Collective motor dynamics in membrane transport *in vitro*

Paige M. Shaklee

Promotiecommissie

Promotores:	Prof. dr. M. Dogterom
	Prof. dr. T. Schmidt
Referent:	Prof. dr. C. Schmidt (Universität Göttingen, DE)
Overige leden:	Prof. dr. M. Orrit
	Dr. ir. J. van Noort
	Dr. ir. E. J. G. Peterman
	(Vrije Universiteit Amsterdam)
	Dr. C. Storm (Technische Universiteit Eindhoven)
	Prof. dr. J. M. van Ruitenbeek

Collective motor dynamics in membrane transport *in vitro*

PROEFSCHRIFT

door

PAIGE MARIE SHAKLEE

geboren te Stamford, CT, Verenigde Staten in 1981

Publications

This thesis is partly based on the following articles:

Paige M. Shaklee, Thomas Schmidt and Marileen Dogterom. Collective motor dynamics in cargo transport. *Review in preparation*
(chapter 1)

Paige M. Shaklee*, Stefan Semrau*, Maurits Malkus, Stefan Kubick, Marileen Dogterom and Thomas Schmidt. Protein incorporation in giant lipid vesicles under physiological conditions. *submitted*
(chapter 2)

Paige M. Shaklee*, Timon Idema*, Gerbrand Koster, Cornelis Storm, Thomas Schmidt and Marileen Dogterom. 2008. Bidirectional motility of membrane tubes formed by nonprocessive motors. *Proc. Natl. Acad. Sci.* USA 105:7993-7997.
(chapter 4)

Paige M. Shaklee, Line Bourel-Bonnet, Marileen Dogterom and Thomas Schmidt. Nonprocessive motor dynamics at the microtubule membrane tube interface. *Biophys. J.* accepted.
(chapter 5)

Paige M. Shaklee, Timon Idema, Line Bourel-Bonnet, Marileen Dogterom and Thomas Schmidt. Kinesin recycling in stationary membrane tubes. *submitted*
(chapter 6)

Contents

Chapter 1

Introduction

Key cellular processes such as cell division, internal cellular organization, membrane compartmentalization and intracellular transport rely on motor proteins. Motor proteins, ATP-based mechanoenzymes, actively transport cargo throughout the cell by walking on cytoskeletal filaments. Motors have been studied in detail on the single motor level such that information on their step size, ATP turnover rate, stall force, average run length and processivity are well known. However, in vivo, motors are often found working together, raising the question of how motors work together in transport. In vitro approaches to understand collective motor behavior that include gliding assays, bead transport, and DNA scaffolds have all provided much information about how motors coordinate stepping in order to transport cargo. However, in all of these experiments, motors are bound to a rigid surface. In their native environment, motors are bound to membrane material so that they can diffuse through a lipid bilayer, suggesting that their collective behavior may rely more on dynamic self-organization than experiments until now have allowed. In this thesis, an in vitro approach is presented to study collections of motors as they self-organize to actively transport membrane along microtubule tracks. [1]

---

[1] *Review in preparation*: Paige M. Shaklee, Thomas Schmidt and Marileen Dogterom. Collective motor dynamics in cargo transport.

1.1   Motor-driven transport

In cells, membrane-bounded vesicles and organelles are often transported over long distances (μm) along well-defined routes and delivered to particular locations. Diffusion alone cannot account for the rate, directionality, and acute destinations of these transport processes. The movement is driven by motor proteins: ATP-fueled mechanoenzymes that convert chemical energy into mechanical work.

Transport occurs over the cell's biopolymer tracks, namely microtubules (MTs) and actin filaments. There are two specific motor families responsible for long-range transport over MTs in cells: dyneins and kinesins. The MTs they traverse are constructed from tubulin heterodimers that associate head-to-tail giving rise to an intrinsic polarity in the MT.[1] Kinesin motors walk towards the dynamic "plus-end" of MTs (typically away from the cell's nucleus) while dynein motors walk in the opposite direction towards the "minus-end" of MTs. Studies inhibiting motor activity have shown that these two motors are essential for bidirectional transport inside of cells.[2] Both dynein and kinesin are processive motors: they take many steps before releasing from a MT. There are also nonprocessive motors that only take a single step before dissociating from a filament such as muscle myosin that interacts with actin filaments.[3] Both processive and nonprocessive motors are key players in intracellular transport and organization. The evidently critical role that motor transport proteins play *in vivo* led to questions about how these individual motor proteins are designed and how they function.

1.2   Single motor studies

Major advances in single molecule studies have provided a font of information about individual motor proteins. The structures of motor proteins are well known from biochemical isolation and DNA sequencing followed by techniques such as cryo-electron microscopy (cryo-EM), X-ray crystallography and nuclear magnetic resonance (NMR).[4,5] Fig. 1.1 shows a kinesin motor taking a step along a MT.[6] The motor binds to the MT via two globular head domains that are held together by a coiled coil

stalk. The the motor is bound to cargo via binding domains at the other end of the stalk (not shown in the image). Structural images of the precise conformation that motors maintain while bound to a MT in different nucleotide states have elucidated the way in which a motor's ATP cycle is coupled to their mechanical movement. These studies provide much information about the structure of motor proteins and the way in which they bind to a MT, but their dynamics have required different probes. A key step towards studying individual motor dynamics has been the isolation of motor proteins so that they can be examined in the absence of other proteins that might alter their behavior. Many microtubule motor proteins can be expressed in *E. coli*[7] and *S. cerevisiae*[8] and purified to use in *in vitro* experiments.
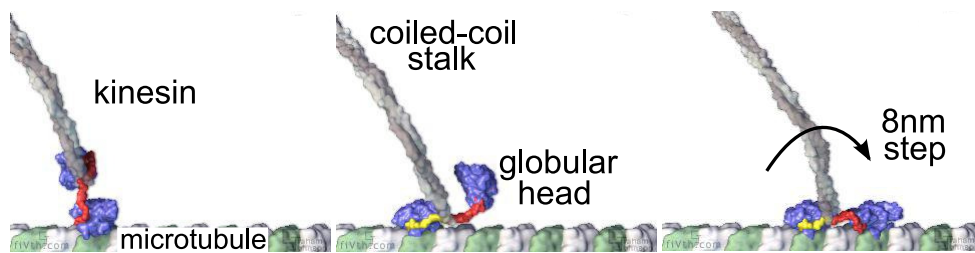
Figure 1.1: **Kinesin on a microtubule** a) Timeseries showing kinesin taking an $8nm$ step along a MT. The globular head domains bind to the MT and are held together by a coiled coil stalk. Cargo is bound at the other end of the stalk.[6]

Elegant experiments with optical traps have allowed enough spatial and temporal resolution to determine the stepsize of individual kinesin motors to be $8nm$.[9] Optical traps also provide force information in the pN range allowing many groups to determine that a kinesin's velocity decreases roughly linearly in response to load until stalling at a load of approximately 4 to $8pN$.[9–12] The distance a kinesin walks on a MT before dissociation, its runlength, has been shown to be $\approx 1\mu m$[13,14] and, at zero-load, the motors consume $1\text{ATP}/step$ and walk at speeds up to $\approx 2\mu m/s$ *in vivo*[2] and $\approx 1\mu m/s$ *in vitro*.[15] Similar experiments have been performed for dynein.[16] Though processive like kinesin, dynein does not

always take uniform $8nm$ steps and often takes side or backsteps. Like dynein, the non-claret dysjunctional protein (ncd), responsible for MT bundling *in vivo*, moves to the minus end of MTs.[17,18] However, unlike dynein, ncd has been shown to be nonprocessive *in vitro*.[19,20] The motor has been used quite frequently as an attractive model to understand the ways in which nonprocessive motors function as compared to processive motors and we also review those findings here. Values for *in vitro* runlength, speed and ATP turnover rate of individual kinesins, dyneins and ncds under zero-load are shown in Table 1.1.

motor	runlength (nm)	speed (nm/s)	ATP^{-1}	stall force (pN)
kinesin	$800 - 1200$[13,14]	1000[15]	100	5[9–12]
dynein	$1000 - 1700$[16,21]	90[16]	–	7[22]
ncd	9[23]	≈ 12[23,24]	1.4[24]	–

Table 1.1: Table of *in vitro* runlength, speed and ATPase for individual microtubule motors: dynein, kinesin and ncd. It should be noted that the values for ncd are based on data for individual motors. Thus, the runlength represents the stepsize and the speed is the speed at which a motor takes a single step rather than the maximum speed that multiple motors can transport a cargo.

Though the wealth of single molecule information about individual motor proteins continues to grow, motors tend to work together.[25] Immunogold EM images of kinesins and dyneins on organelle fractions show motors that are grouped in clusters of two or more on membrane cargo and in many cases all the motors on the cargo are localized to a single cluster.[26–29] There is more and more evidence that cooperation between multiple motors in cargo movement is a key mechanism that cells use to regulate cargo transport.[30] Thus, recently, interest has increased in the area of collective motor dynamics.

1.3   From the individual to the collective

Many of the initial experiments to examine collective motor behavior have been performed *in vitro*. *In vitro* experiments are ideal experiments

to perform in order to ensure that no other external factors influence the dynamics observed under the microscope. Some of the very first *in vitro* experiments to examine collective motor behavior were gliding assays. In these assays, motors are bound by their tail to a glass surface, leaving their feet (or heads) free above (fig. 1.2b). When the motors encounter a
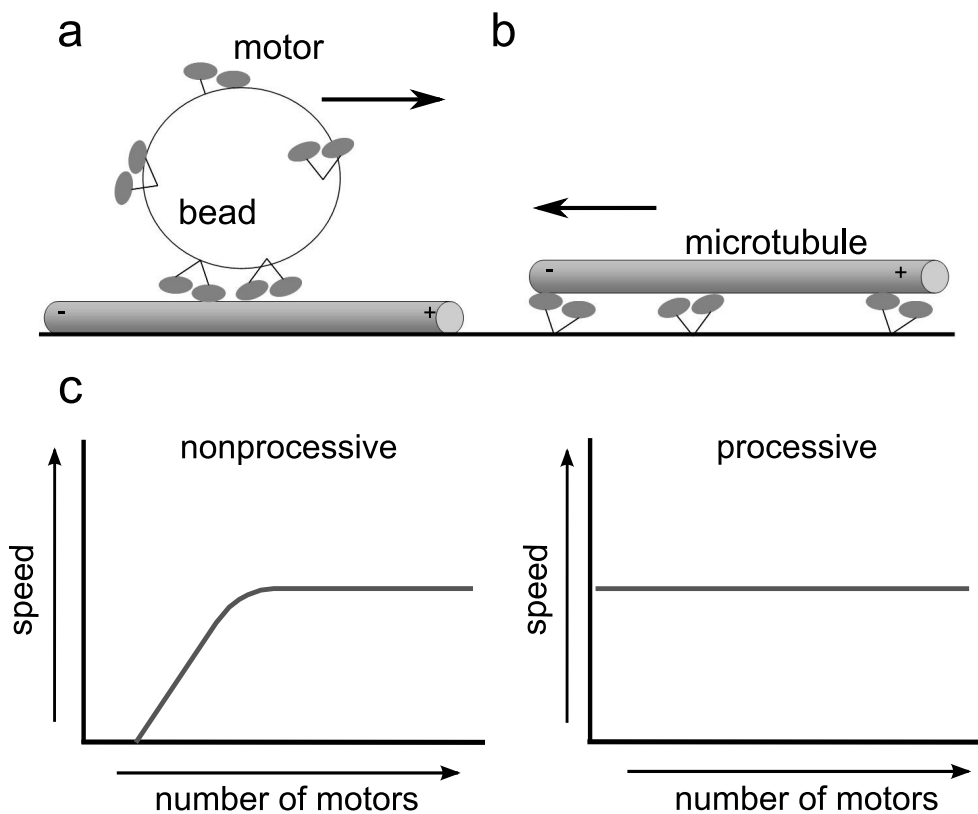
Figure 1.2: *In vitro* **motility assays** a) Bead assay: the bead moves in the same direction as the motors walk. b) Gliding assay: the microtubule glides along the surface in the direction opposite from the motor walking direction. c) The speed of MT gliding by nonprocessive motors is number dependent. However, for processive motors, the MTs are moved at the same speed regardless of the number of motors attached to the filament.

MT that is freely diffusing above in the bulk of a sample, they immediately bind to the MT. Because the motors are anchored in place, as they

walk, the MT glides across the surface. For processive motors, regardless of the number of motors and in the absence of load, the MTs glide at the same speed[31] suggesting that a certain degree of coordination between motors must exist.[3] In contrast, the MT gliding speed by nonprocessive motors *is* number dependent: for continuous gliding a threshold number of motors available to bind the filament is necessary. Thereafter gliding speed increases with motor density up to a maximum gliding speed (fig. 1.2c) that depends on the fraction of time a motor is bound to a filament during its ATP cycle: the duty ratio.[3] For example, ncd has a duty ratio of ≈ 0.08. The MT gliding speeds ncd motors can exhibit range from $12 - 160 nm/s$[19,32] where $160 nm/s$ is the saturation speed. In order for nonprocessive motors to transport a cargo, they must coordinate to form an effectively processive ensemble, such as the case of the Myo4p nonprocessive motor responsible for mRNA transport.[33,34]

The gliding assay has been used to determine the dynamics of various collective motor systems. Gliding assays with a mutant version of the minus-end directed ncd motor, NK11, have shown that motors can spontaneously change the direction in which they step resulting in bidirectional MT gliding.[35] Moreover, the assay has shown the force-mediated switching behavior of MTs that glide by competing plus-end directed kinesin and minus-end directed dynein[36] as well as by antagonistic kinesin-5 and ncd.[37] Coordination in stepping and binding/unbinding rates must all be uniquely coupled to regulate the motor ensembles. Major steps have been taken to advance this assay, so that it can be tailored using specialized surface chemistry to control the motor density on the surface and determine that a loose mechanical coupling between motors is necessary for efficient transport by motor ensembles.[38]

Because collections of motors are often used to transport micrometer-sized cargos *in vivo*, another typical assay to examine motor behavior is to attach motors to a bead *in vitro* and allow the motors to move the bead as they walk on underlying MTs (fig. 1.2a). Beads moved by kinesins move at constant speeds independent of motor number but run-length increases as more motors are available to interact with the MT.[30,39] In contrast, beads moved by dynein-dynactin complexes (dynactin serves

as a cargo binder) with a high number of motors tend to pause frequently and anchor the bead cargo at microtubule intersections.[40] Moreover, while individual dynein-dynactins can often display bidirectional movement, ensembles of dynein-dynactins move cargo unidirectionally (in both gliding and bead assays).[41]

In both the gliding assays and the bead assays, motors are randomly organized on a surface (flat glass surface or rounded bead surface) so that their position and orientation as well as relative distances from eachother are unknown. Recent experiments using DNA scaffolds to couple discrete numbers of motors at set distances have confirmed that multiple kinesins maintain longer runlengths than individuals while their speed does not vary.[42] When two motors are coupled (a distance of $50nm$ apart), though the transport speed does not vary, the unbinding rate of an individual motor is enhanced and cargo is no longer transported in discrete $8nm$ steps.[43]

1.4 Collective dynamics in membrane transport and tube pulling

In all of these experiments, motors are bound to a rigid surface. However, in their native environment, motors are bound to membrane material so that they can diffuse through a lipid bilayer, suggesting that motors' collective behavior may depend on the ability to assemble and freely rearrange configuration. This type of self-organization has not been allowed for in the experiments described so far. Preliminary experiments where collections of kinesins are attached to small oil droplets, a model system for small vesicles *in vivo*, exhibit the same transport characteristics as beads transported by multiple kinesins.[44] The physical properties of oil droplets are different from small vesicles made of membrane material, though, and the collective dynamics of MT motors in the absence of any other proteins on small vesicles has yet to be investigated.

An alternative model system to study collective membrane-bound motor dynamics is provided where functionalized kinesin motors are specifically attached to giant unilamellar vesicles (GUVs) and allowed to en-
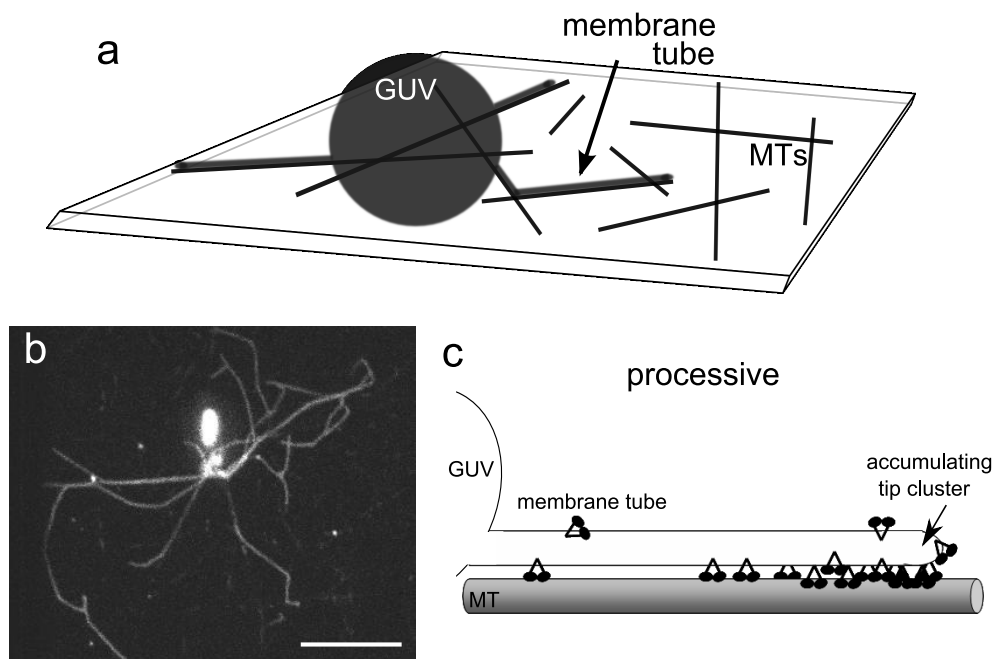
Figure 1.3: **Motors in membrane tubes** a) Schematic of experiments for tube pulling. A GUV coated with motor proteins sits on top of randomly arranged MTs on a glass surface. Motors walk along the MTs, pulling membrane material from the GUV with them to extract membrane tubes. b) Fluorescence image of an *in vitro* membrane tube network formed by kinesin motors on top of a mesh of unlabeled MTs. bar=$10\mu m$. c) Cartoon of processive motors in a membrane tube. The motors walk towards the tip at full speed, however, motors at the tip are slowed because of the tube pulling force so motors accumulate at the tip.

counter MTs on a surface have shown that with the simple addition of
ATP, membrane tube networks are formed[45] (fig. 1.3a). An example of
a network formed by kinesin motors is shown in figure 1.3b. The for-
mation of these elaborate networks that mimic the dynamic membrane
tube networks of the endoplasmic reticulum[46] relies on the cooperation
of multiple motors. An individual motor cannot exert enough force to
deform the GUV and extract a membrane tube, but collectively, clusters
of motors can exert a force large enough to pull a tube. This force scales
as $F_{\text{tube}} \sim \sqrt{\kappa\sigma}$, where κ is the membrane bending modulus and σ the
surface tension.[47,48] The prediction that motors dynamically assemble
and form a stable tip cluster to pull a tube[49] has been experimentally
verified[50] and supported by a microscopic model.[51] Because the speed
of motors at the tip of the tube is damped by the opposing tube-pulling
force, motors that walk at full speed along the length of the membrane
tube collect at the tip. Figure 1.3c shows a schematic cartoon of ki-
nesin motors dynamically clustering at the tip of a membrane tube. In-
triguingly, the unequal load felt by different motors in a membrane tube
(where the highest load in the tube is at the very tip acting on the tip-
most motor) may facilitate the clustering at the tip that is necessary to
continuously move the tube.[52]

These experiments where motors can self-organize on a membrane
cargo provide an experimental framework that allows us to explore many
questions. We have seen that as more nonprocessive motors attach to a
MT in gliding assays, the faster the MT glides. If nonprocessive motors
are not rigidly coupled to a surface, and allowed to freely arrange on their
cargo can they perform directed work for transport of e.g. membrane
tubes? If so, how do the motors coordinate for transport? What are the
dynamics of motors when they reach the end of a MT and can not pull
a membrane tube any farther? How do motors of opposite directionality
organize on vesicles to mediate bidirectional transport?

1.5   Contents of the thesis

In this thesis, I address these questions about motor collectivity in membrane transport. I use an *in vitro* approach where I attach motor proteins to membrane reservoirs, GUVs. When motors on the GUV encounter MTs on the surface, in the presence of ATP, motors self-organize to extract membrane tubes. I examine both the movement of the membrane tubes and the dynamics of the motors in the membrane tubes. Chapter 2 provides details on the materials and common methods used in these membrane tube experiments throughout this thesis.

I show, in chapter 4, the surprising result that membrane tubes can be formed by nonprocessive motors. Nonprocessive ncd motors not only extract membrane tubes from GUVs, but they also mediate bidirectional membrane tube dynamics. I present a model for this system and suggest that bidirectional tube movement is the eventuality of this system.[32]

Whereas in chapter 4, all the motor dynamics are inferred by examining membrane tube behavior, chapter 5 directly examines motor dynamics in membrane tubes. Motor dynamics at the MT-membrane tube interface are probed using the techniques of image correlation spectroscopy and fluorescence recovery after photobleaching. Nonprocessive motors bind to the MT over the entire length of the membrane tube, while as expected, processive motors accumulate at the tip of the tube.[50] I find a very small diffusion constant for motors at the MT-membrane tube interface suggesting that a constant high-density of motors is maintained to mediate the membrane tube dynamics seen in chapter 4.[53] The detailed derivations of the solutions for the autocorrelation function and fluorescence recovery profile in one dimension are written in chapter 3. The derivations are meant to describe membrane tubes which are approximated as one-dimensional lines for the cases of a) simple diffusion and b) where the particles in the system exhibit a directed motion.

Chapter 6 examines the recycling phenomenon that arises in nonmoving membrane tubes formed by processive motors. I present a model that proposes that cooperative binding[54] leads to the formation of clusters that walk towards the tip of a membrane tube. Cooperative binding combined with cooperative unbinding at the tip and a nucleation point

along the MT define a the recycling period. Based on comparison of the numerical results and experimental data I estimate a binding probability and concentration regime where the recycling phenomena occurs.[55]

Chapter 7 discusses future research directions that follow from the work in the rest of the thesis. In particular I present preliminary experiments and simulations examining the competition between dynein and kinesin motors in small vesicle transport *in vitro*.

Chapter 2

Materials and Methods

The following chapter describes experimental methods, technical details and assays that were used for the experiments throughout this thesis. The first section describes the electroformation method used to obtain giant unilamellar vesicles (GUVs). We also describe the purification of motor proteins and how we form microtubules. We also discuss a new application of electroformation under physiological conditions to encapsulate proteins inside of GUVs. Experiments exploring this application were performed by Maurits Malkus during his bachelor thesis internship. We further describe methods to make small vesicles. The second section discusses the assays and tools used to examine membrane tube formation and motors during membrane tube formation. [1]

2.1 Materials: vesicles, motors and microtubules

An *in vitro* experiment designed to examine membrane tube formation by microtubule motors requires three essential ingredients: membrane, microtubules and motors. Here, we use giant unilamellar vesicles (GUVs) as a membrane reservoir. In recent years, GUVs have proven a useful tool for biophysical experiments because they are easy to make and manipulate. Motor proteins functionalized with a biotin can be specifically attached to the GUV via streptavidin and a biotinylated lipid. When the moter-coated GUV encounters a microtubule on a glass surface, the motors walk on the MT and exert enough force to deform the membrane. The following section details the methods used to obtain GUVs, stable microtubules and purified, functionalized motor proteins.

2.1.1 Vesicle formation

Giant Unilamellar Vesicles

GUVs can be formed via the electroformation (EF) method,[56] from various combinations and ratios of lipids. Initially, small vesicles form by natural swelling of a lipid bilayer on conducting glass. As the vesicles vibrate with the frequency of an applied voltage, they fuse with neighboring vesicles to create progressively larger vesicles. The method yields many GUVs of large diameter ($10s$ of μms).

The GUVs used for experiments in this thesis were made as follows: A mixture of $2mM$ lipids dissolved in 90% chloroform and 10% methanol are dropped onto one of two indium tin oxide (ITO) coated glass slides ($4cm$ x $6cm$). The 10% methanol is added to the mixture to facilitate lipid adhesion to the glass. The lipids are distributed on the glass by the "rock and roll" method[56] and dried for $1hr$ under continuous nitrogen flow. A chamber is constructed from the two glass plates, the dried lipids on the bottom glass, and a polydimethylsiloxane (PDMS) spacer with a hole in the middle (fig. 2.1a). The chamber is filled with a solution of $200mM$ sucrose and an AC voltage, 3.3V at $10Hz$, is applied to the glass plates (cartoon in fig. 2.1a). After ≈ 5 hours, vesicles reach sizes ranging
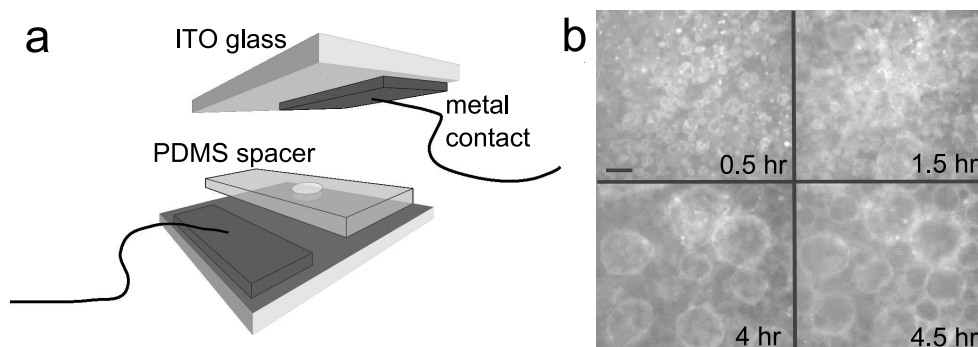
Figure 2.1: **Electroformation chamber**. a) The electroformation chamber consists of two conducting glass coverslides (indium titanium oxide, ITO) with metal contacts and a PDMS spacer with a hole in the middle where the lipids and sucrose solution are placed. b) Timeseries showing the formation of GUVs in the chamber. A fraction of the lipids are fluorescently labeled and the vesicles are imaged from below through the ITO glass with an epi-fluorescence microscope. Over time, vesicles swell and fuse with neighboring vesicles to create GUVs from 5 to $50\mu m$ in diameter, bar $20\mu m$.

from 5 to $50\mu m$ in diameter, fig. 2.1b.[56] The vesicles are then harvested from the chamber and further used in experiments.

GUVs formed under physiological conditions

We explored applications of electroformation under physiological conditions[57,58] in order to encapsulate proteins inside of GUVs. The advantage of this method is that the proteins can be directly encapsulated by GUVs during electroformation in the presence of their appropriate saline buffer. We verified that proteins in high salt buffers could be encapsulated in GUVs made from synthetic lipids. We further determined that these proteins retained their function during electroformation by showing that eYFP was encapsulated and still fluoresced after electroformation (Fig. 2.2c). We performed the same experiments with tubulin and tubulin proteins were incorporated into GUVs during electroformation, where they successfully polymerized in the presence of GTP. The proteins polymerized into MTs that actively exerted pushing forces from the inside of the GUV, reshaping the GUV (Fig. 2.2d) into similar shapes

reported by others.[59] The tubulin/MTs retained their property of "dy-namic instability" where the MT switches between growing and shrinking phases. The radical dynamic shape changes of the membrane protrusion in the timeseries and inset of Fig. 2.2d are an indicator of the growing and shrinking MTs. The MTs deformed the GUVs at speeds ranging from $0.3\mu m/min$ to $5.7\mu m/min$, in agreement with MT growth speeds reported by others.[60] We further probed the size limits for encapsulation. We successfully internalized $1\mu m$-sized beads in these GUVs (Fig. 2.2b).
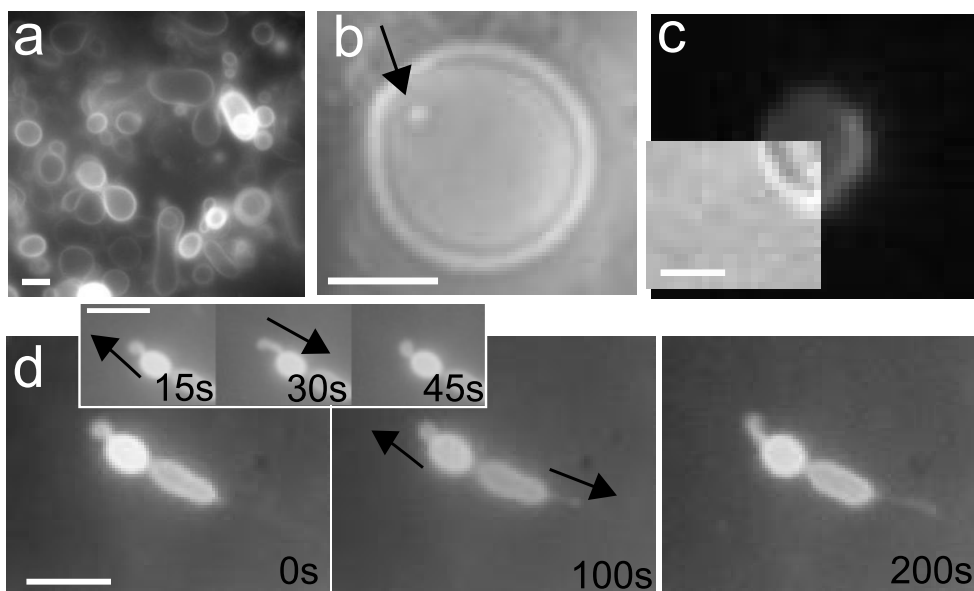
Figure 2.2: **Proteins retain function inside GUVs** (a) GUVs formed under physiological conditions (in MRB40). (b) A $1\mu m$ polystyrene bead (indicated by the arrow) encapsulated by a GUV (c) Fluorescence image of a GUV containing eYFP incorporated during electroformation, lower left overlay is a phase contrast image of the vesicle. (d) Time series showing the dramatic shape changes of GUVs deformed by dynamic GTP MTs grown at 37°C. MTs deform the vesicle at speeds up to $5.7\mu m/min$. Inset shows growth followed by retraction of a membrane protrusion due to MT depolymerization. All scale bars are $5\mu m$.

The GUVs under physiological conditions were made as described

here. DOPC, and DOPE-Rh were purchased from Avanti Polar Lipids. Tubulin, GTP and GMPCPP (a non-hydrolyzable GTP analog) were purchased from Cytoskeleton. eYFP was purified from *E. coli* SG13009 with the inserted plasmid pMP6088 stam 6244 (Qiagen).[61] Lipids were resuspended in 90% chloroform and 10% methanol, and 0.2mol% DOPE-Rh was added to DOPC to a final volume of $100\mu l$. $1\mu l$ of the lipid solution was dropped onto one of two indium tin oxide (ITO) coated coverslips purchased from Diamond Coatings Limited. The lipids were distributed on the glass by the "rock and roll" method[56] and dried for $30min$ under continuous nitrogen flow. An $8\mu l$ volume chamber was constructed from the two glass plates, the dried lipids on the bottom glass, and a polydimethylsiloxane (PDMS) spacer.

The chamber was first filled with MRB40 ($40mM$ Pipes / $4mM$MgCl$_2$ / $1mM$ EGTA, $pH6.8$, $100mOsm$) containing eYFP to verify protein incorporation. The experiments were repeated in the same way with a solution of $38\mu M$ tubulin in MRB40 and $4mM$ GTP or GMPCPP (conditions for spontaneous nucleation) and/or polystyrene beads and placed at $4°C$. In contrast to the original electroformation method,[56] we applied an AC electric field at a higher frequency[57,58] as follows: the AC electric field was applied at $500Hz$ with a linear voltage increase from $50Vm^{-1}$ to $1300Vm^{-1}$ over $30min$, held at $1300Vm^{-1}$ for $90min$, then the frequency was decreased linearly from $500Hz$ to $50Hz$ linearly over $30min$. During imaging GUV samples with GTP MTs were heated to $37°C$ by a heating foil mounted on top of the sample.

Small Unilamellar Vesicles

SUVs were formed using the freeze-thaw method.[62] Lipids were resuspended in chloroform and allowed to dry under nitrogen flow in a plastic tube. PEG lipids were added to minimize direct lipid interaction with the charged glass, so that fewer vesicles interacted with or exploded on the glass. The lipids were resuspended in $300\mu l$ of $50mM$ KCl and flash-frozen and thawed five times, followed by sonication. $50mM$ KCl was chosen because it is the minimum salt concentration necessary to make small vesicles and it has the same osmolarity as MRB40, the salt buffer

we used later in experiments with MT motor proteins. If the solution appeared clear, then the SUVs were successfully formed and were checked under the microscope. If the solution appeared milky, the freeze-thaw steps were repeated until the solution became transparent.

Vesicles used in experiments

In chapter 4, GUVs were composed of: 1, 2, - dioleoyl - sn - glycero - 3 - phosphocoline (DOPC), 1, 2 - dioleoyl - sn - glycero - 3 - phosphoethanolamine - N - (cap biotinyl) (DOPE-Bio), and 1 , 2 - dioleoyl - sn - glycero - 3 - phosphoethanolamine - N - (lissamine rhodamine B sulfonyl) (DOPE-Rh). All lipids were purchased from Avanti Polar Lipids. $20\mu l$ of the 2mM lipid mixture in 1 : 10 chloroform:methanol (96.9mol% DOPC, 0.1mol% DOPE-Rh and 3mol% DOPE-Bio) were dried on ITO glass. Here, vesicles were made in an electroformation chamber with a $1ml$ volume.

In chapters 5 and 6, GUVs were composed of: DOPC and a rhodamine-labeled biotinylated phosphatidylethanolamine (Rh-B-DSPE), supplied by Line Bourel-Bonet.[63] For Image Correlation Spectroscopy experiments, a lipid composition of 99.9mol% DOPC with 0.1mol% Rh-B-DSPE was used in order to bind ≈ 125motors/μm^2. This lipid composition was chosen to be able to directly compare results with published results from others.[50] However, for practical reasons regarding imaging, visualization and photobleaching, the number of fluorophores and hence, motors used in the Fluorescence Recovery After Photobleaching experiments was increased. Specifically, 99.7mol% DOPC with 0.3mol% Rh-B-DSPE was used to bind ≈ 375motors/μm^2. In this case $10\mu l$ of lipid mix was dropped on the ITO glass of a $300\mu l$ volume electroformation chamber.

In chapter 7, small vesicles were composed of: 94.9mol% DOPC, $4mol\%$ 1, 2 - Dioleyl - sn - glycero - 3 - phosphoethanolamine - N - [methoxy - (polyethylene glycol) - 2000] (PEG - (2000) - DOPE), 1mol% 1 , 2 - distearoyl-sn-glycero - 3 - phosphoethanolamine - N - [biotinyl - (polyethylene glycol) -2000] (Bio - PEG - (2000) - DSPE) and 0.1mol% DOPE-Rh.

2.1.2   Microtubules

Microtubules (MTs) were prepared from tubulin purchased from Cytoskeleton. Tubulin ($10mg/ml$) in MRB80 ($80mM$ K-Pipes / $4mM$ MgCl$_2$ / $1mM$ EGTA, pH 6.8) with $1mM$ GTP was incubated for $15min$ at $37°C$ to polymerize. MTs were stabilized by mixing 1:10 (vol/vol) with MRB80 containing $10\mu M$ taxol .

2.1.3   Motor Proteins

Three MT motor proteins were used in the experiments in this thesis: kinesin-1, non-claret dysjunctional (ncd) and cytoplasmic dynein. Kinesin and dynein are both processive motors but kinesin moves towards the plus-end of MTs while dynein walks to the minus-ends. Ncd is non-processive and moves towards the minus-end of MTs. Though, *in vivo*, ncd is used to bundle MTs during mitosis,[64] in this thesis we use it as a model motor to study the collective behavior of nonprocessive motors. We repeat all the experiments that we perform with nonprocessive motors, with the processive motor, kinesin, which has been studied extensively and hence a useful motor to study as a comparison. Furthermore, kinesin and ncd both take uniform 8nm steps[15, 23] and are both entirely unidirectional. In contrast, dynein's stepsize can vary[16] and it takes occasional backsteps in the absence of load.[16] *In vivo*, dynein and kinesin are responsible for bidirectional transport along MTs. Thus, in this thesis, we use the combination of dynein and kinesin in a reconstituted system with small vesicles to examine the dynamics of motor competition in transport.

Full-length motors are often hydrophobic, stick to surfaces *in vitro* and are more difficult to purify. To circumvent these practical problems, we use minimal motor constructs for all of our experiments. The sections below specify the construct designs, purification details, and resulting motility characteristics.

Kinesin-1 and ncd

Kinesin and Ncd dimers were expressed and purified in our lab. The first 401 residues of the kinesin-1 heavy-chain from Drosophila melanogaster, with a hemaglutinin tag and a biotin at the N-terminus, were expressed

in *Escherichia coli* and purified as described.[65] The plasmid was a kind gift from Dr. F. Nédélec and Dr. T. Surrey (Heidelberg, Germany) and was originally created in Jeff Gelles' lab (Brandeis University, USA). Residues K195-K685 of the nonclaret disjunctional (ncd) from Drosophila melanogaster, with a 6x-His tag[23] and biotin, were expressed and purified in the same fashion, but with lower induction conditions: 10 μM Isopropyl β-D-1-thiogalactopyranoside (IPTG). The ncd plasmid was a kind gift from Dr. R. Stewart and Dr. M. van Duijn modified the plasmid to contain the biotin binding region.

Motors were further purified by MT affinity purification to remove any inactive motors.[66] Their resulting ATP activity was verified by an ATPase assay.[67] The concentration of motors was estimated from the ATP activity assuming an ATPase for ncd of $1.4s^{-1}$ and $60s^{-1}$ for kinesin and motors were stored at concentrations of $\approx 2\mu M$. Motors were tested for MT gliding activity bound to a glass surface via their biotin tag (see cartoon in fig.1b in chapter 1). Kinesins exhibited MT gliding speeds of $475 \pm 50 nm/s$. Ncd speeds ranged from $16 nm/s$ to $120 nm/s$ depending on the surface density of motors. Though MTs that were glided by Ncd often slowed down, or even paused, they always moved unidirectionally over the surface. The kinesin was used in experiments in chapters 4-7 and ncd in chapters 4-6.

Dynein

The artificially dimerized cytoplasmic dynein construct GST-Dyn1-331kD was made as described.[16] The construct was modified to contain a HA-LOtag^{TM} (Promega) that could be biotinylated and a SNAPtag^{TM} (Covalys) that could be labeled with a fluorophore. Purification was performed as described[16] with the generous help of Dr. S.L. Reck-Peterson in her lab at the Harvard Medical School.

Dynein motors were initially tested for activity in an assay where Cy5-labeled sea urchin axonemes were stuck aspecifically to a glass surface in a flow cell (fig. 2.3a). Motors were then added to the flow cell and allowed to bind in the rigor state to the axonemes, (in the absence of ATP). The chamber was rinsed to remove any unbound dynein, and

then streptavidin Q-dots (QuantumDot Inc.) were added to the chamber and allowed to incubate for $10min$. The chamber was washed again and motility buffer ($30mM$ HEPES pH 7.2, $50mM$ KAcetate, $2mM$ MgAcetate, $1mM$ EGTA, 10% glycerol, $1mM$ DTT, $1mM$ Mg-ATP, and an oxygen scavenger system) was added. The axonemes and Q-dots were visualized with a TIRF microscope using objective-style TIRF and an Argon laser with $491nm$ illumination at $3mW$. Images were acquired with a cooled, intensified CCD camera (Mega10-S30Z, Stanford Photonics).

The kymograph in fig. 2.3b shows the displacement of the two marked Q-dots in fig. 2.3a as Dynein molecules moved them along the axoneme. The Q-dot speeds ranged from $\approx 65nm/s$, an expected speed for a single dynein motor[16] to $\approx 10nm/s$ where the Q-dots were likely slowed by the presence of many other motors attached to the bead in varying orientations (elucidated in the case where bead aggregates were walked along the axonemes at slow speeds) or by additional inactive motors that bind to the axoneme but do not walk. Motors were further tested for motility in MT gliding assays. Fig. 2.3c shows a plot of MT gliding speed vs. dynein surface concentration. The gliding speeds increase with decreasing dynein concentration and plateau around $40nm/s$. The slowing speeds as surface concentration increases are likely due to the presence of inactive motors that also interact with the MTs so that the other motors cannot easily glide the MT.

Gliding speeds of the unmodified GST-Dyn1-331kD under the same experimental conditions are consistently $\approx 130nm/s$. The reduction in gliding speed of the new construct arose from an error in the incorporation of the SNAPtag that may have caused other folding changes in the motor. The construct is currently being rebuilt with a short linker between the SNAPtag and the dynein motor. However, the dynein characterized here was used for the preliminary vesicle transport competition experiments with kinesin in chapter 7.
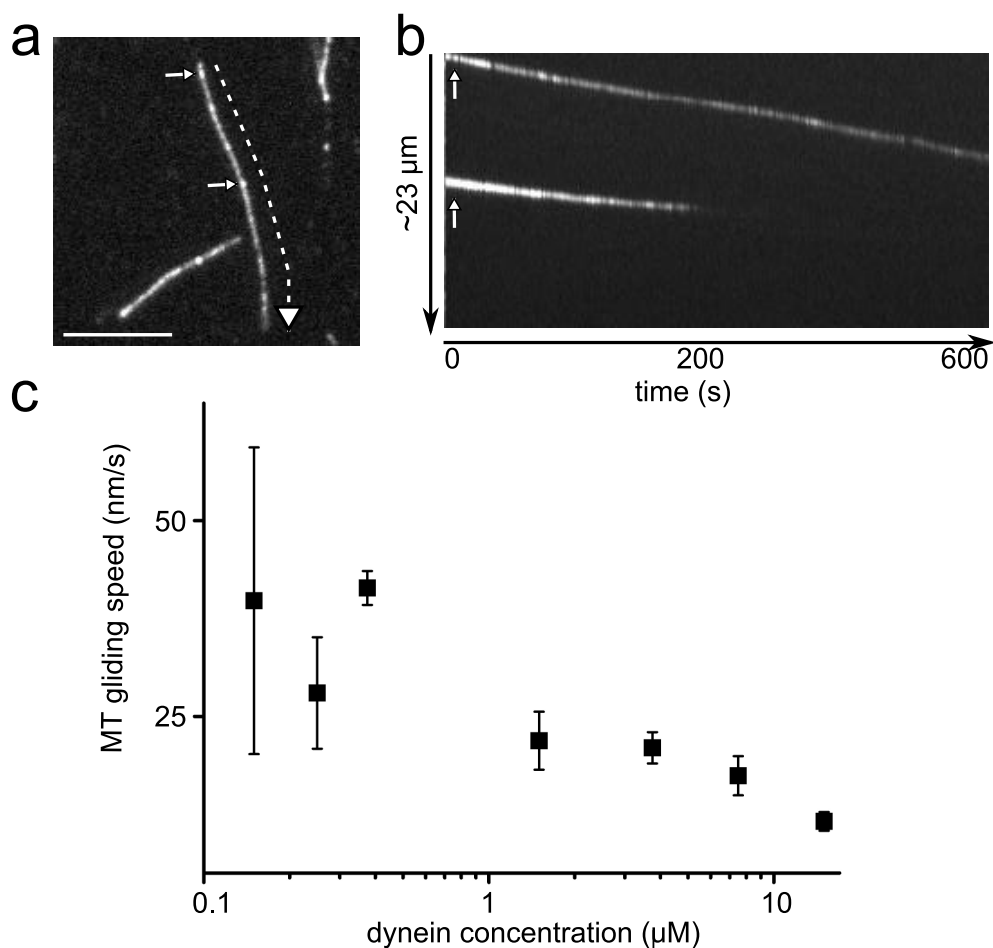
Figure 2.3: **Dynein motility tests**. a)Fluorescence image of Cy-5 labeled axonmenes aspecifically attached to a surface. Dynein-coated Q-dots (examples indicated by the arrows) walk along the axonemes. b) Kymograph of the Q-dots on the axoneme (not shown) from (a) showing the Q-dot displacement as dynein transports them along the axoneme. c) Plot of dynein surface concentration versus MT gliding speed for different gliding assays with dynein. The gliding speed increases slightly as the surface concentration of dynein decreases most probably because fewer inactive motors are available to interact with the MTs and slow down neighboring motors.

2.2 Experimental Assays

2.2.1 Tube-pulling assay

The assay we used to observe membrane tubes *in vitro* in chapters 4,5 and 6 in this thesis consisted of motor-coated GUVs that interact with MTs on a glass surface. In the presence of ATP, motors can collectively exert enough force to deform the spherical vesicle and extract membrane tubes as they walk along the underlying MTs. We describe the specific details of this assay below.

For the experiments in chapter 4, glass coverslips were soaked in Chromosulfuric Acid for $1hr$, rinsed with deionized H_2O, and dried with nitrogen flow. The coverslips were soaked in poly-l-lysine $1 : 500$ by volume in ethanol for $5min$ and dried with nitrogen flow. A circular area on the coverslip was defined with a circle of vacuum grease allowing for a $50\mu l$ sample volume (sample style (a) in fig. 2.4a). MTs were dropped onto the sample area and incubated for $10min$ to adhere. MTs that did not stick to the surface were removed by rinsing two times with MRB40 ($40mM$ K-Pipes/ $4mM$ $MgCl_2$/$1mM$ EGTA, pH 6.8) containing $10\mu M$ taxol (MRB40tax). α-Casein (Sigma) was dropped on the surface ($1mg/ml$) to coat the surface and minimize interaction of GUVs with exposed glass, incubated for $10min$ and rinsed with MRB40tax.

In parallel, GUVs were mixed 1:1 in MRB40tax with $180mM$ glucose to osmotically match the intravesicular osmolarity (Halbmikro Osmometer, Type M, Knauer, Germany). $2.5\mu l$ of $2mg/ml$ streptavidin were added to $50\mu l$ of the vesicle solution and incubated for $10min$. This quantity of streptavidin saturates all biotin binding sites on the vesicle. Next $2\mu l$ of motor (kinesin or ncd $\approx 650\mu g/ml$) was added and incubated for $10min$. $40\mu l$ of the vesicle solution was dropped onto the sample area. $20\mu l$ of MRB40tax with $180mM$ glucose was dropped on top of the sample to help the vesicles to settle to the glass surface. Finally, $0.5\mu l$ Oxygen Scavenger ($8mM$ DTT/$0.4mg/ml$ catalase/$0.8mg/ml$ glucose oxidase) and $1\mu l 100mM$ ATP were added to the sample. The sample was sealed by placing a coverslip on top of the bottom glass and circle of vacuum grease (as in fig 2.4a).
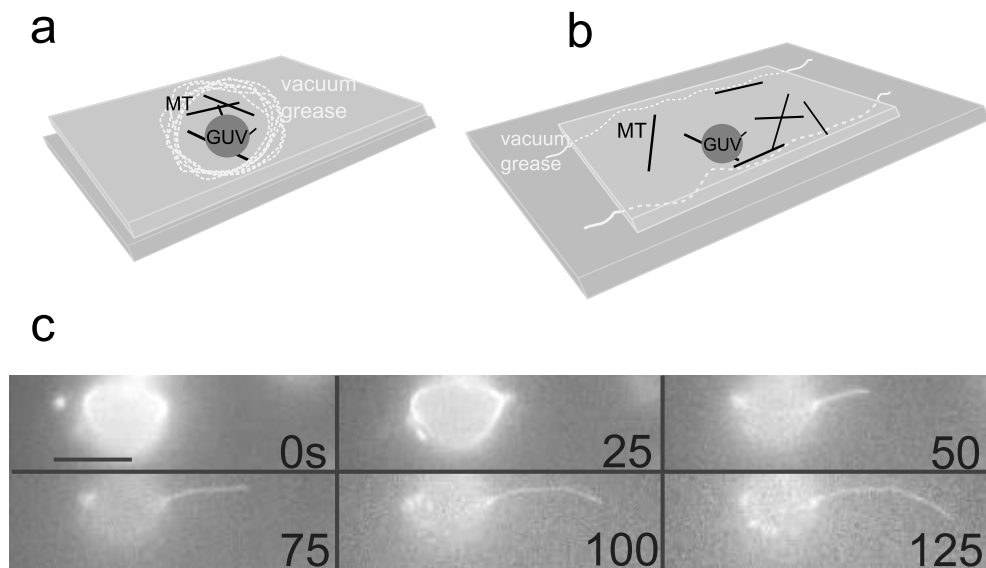
Figure 2.4: **Sample preparation**. a) sample style (a): a circular area on the coverslip was defined with a circle of vacuum grease allowing for a $50\mu l$ sample volume. MTs stick to the surface and GUVs coated with motors are dropped on top of them. A top coverslip is dropped on top of the vacuum grease circle and gently pressed down to make a sealed chamber. b) sample style (b): a flow cell is constructed with a clean coverslide with thin stripes of vacuum grease whereupon a ploy-l-lysine or DETA-treated glass slide is placed allowing for a $15\mu l$ sample volume. MTs and GUVs covered with motor proteins are added to the flow cell, and in the presence of ATP, motors extract membrane tubes from the GUVs. c) Fluorescence time series showing a membrane tube extracted by kinesin motors. Here the membrane is fluorescent and the MTs on the surface are not visible. bar= $10\mu m$.

The experiments in chapters 5 and 6 had a slightly different preparation. Glass coverslips were cleaned by sonication in KOH and further charged with DETA, a peptide similar to poly-l-lysine, as described.[68] We adapted this method of sample preparation because the DETA-coated glass yielded a higher surface coverage with MTs. A glass coverslide and the DETA-treated coverslip were used to make a $15\mu l$ flow cell (see sample style (b) in fig. 2.4b). We adapted the sample preparation to a flow cell method to better rinse between incubation steps. We used the original sample style (for the experiments in chapter 4) in fig. 2.4a to reduce the possibility of shearing vesicles during a flow, but found that the vesicle yield with sample style (b) was comparable. Taxol stabilized MTs were incubated in the flow cell for $10min$ to adhere to the surface. MTs that did not stick to the surface were removed by rinsing the flow cell twice with MRB40tax. Casein Sodium Salt (Sigma) $(200\mu g/ml)$ in MRB40tax were incubated in the flow cell for $8min$ to block the remaining surface and minimize interaction of GUVs with exposed glass. The flow cell was subsequently rinsed with MRB40tax.

GUVs were mixed 1:1 in MRB40tax with $180mM$ glucose. $1\mu l$ of $2mg/ml$ streptavidin was added to $30\mu l$ of the vesicle solution and incubated for $10min$. Next $1\mu l$ of $2\mu M$ motor was added and incubated for $10min$. Finally, $0.5\mu l$ Oxygen Scavenger ($8mM$ DTT/$0.4mg/ml$ catalase/$0.8mg/ml$ glucose oxidase) and $1\mu l$ of $100mM$ ATP were added to the vesicle solution. $15\mu l$ of the vesicle solution was slowly pipetted with a cut-off pipette tip into the flow cell. A cartoon of the flow cell is shown in fig. 2.4b with stable MTs randomly bound to the surface and a GUV settled on top of the MT mesh. It should be noted that though the cartoon only shows one example GUV, in practice a single sample has many GUVs on top of the MT mesh.

The flow cell was sealed with hot candle wax at the open ends. We then examined the fluorescent GUVs under the microscope and could see membrane tubes being extracted from the vesicles. Fig. 2.4c shows an example time series of a membrane tube extracted by kinesin motors. Here, only the membrane is fluorescently labeled so that neither the MTs nor the motors are visible. Though photobleaching does occur,

the apparent rapid loss of fluorescence in the GUV is actually due to refocusing of the microscope.

2.2.2 SUV transport assay

In chapter 7, SUVs were transported over MTs by kinesin and/or dynein. Experiments were performed as described here. Taxol stablized MTs were allowed to adhere to the surfaces of a flow cell made of a coverslide and a DETA-treated coverslip. Then, $0.4mg/ml$ casein sodium salt was incubated in the chamber. In parallel, $1\mu l$ of $2mg/ml$ streptavidin was added to SUVs diluted in MRB40. Subsequently, $1\mu l$ of $2mM$ kinesin and/or dynein was added to the SUV mixture. Finally, an oxygen scavenging system, MgATP, methylcellulose and casein were added to the SUV mixture. Then, the motor-coated SUVs were added to the flow chamber, the flow chamber was sealed and SUVs were imaged.

2.3 Image Acquisition

The majority of the data presented in this thesis relied on the analysis of timeseries of images. The images were acquired on various microscope setups described below.

Images shown in this chapter and in chapter 4 were acquired on an epifluorescence inverted microscope equipped with a CCD camera (Axiovert 40CFL, Carl Zeiss Inc.; WAT-902H ULTIMATE, Watec, Japan) at video rate.

Images in chapters 5, 6 and 7 were acquired on a spinning disc microscope comprised of a confocal scanner unit (CSU22, Yokogawa Electric Corp.) attached to an inverted microscope (DMIRB, Leica) equipped with a $100x/1.3$ NA oil immersion lens (PL FLUOTAR, Leica) and a built-in $1.5x$ magnification changer lens. The sample was illuminated using a 514 nm laser (Coherent Inc.). Images were captured by an EM-CCD (C9100, Hamamatsu Photonics) controlled by software from VisiTech International. Images were acquired with a $100ms$ exposure at $10Hz$.

Fluorescence recovery after photobleaching data in chapter 5 was acquired on a widefield fluorescence microscope setup. An oil immersion objective (100x, N.A.=1.4, Carl Zeiss, Oberkochen, Germany) was

mounted onto a piezo-driven actuator (PIFOC, PI, Karlsruhe, Germany) on an inverted microscope (Axiovert200, Zeiss, Oberkochen, Germany). Images were projected onto a CCD-camera (Cascade 512B, Roper Scientific, Tucson, AZ). A dichroic mirror and an emission filter (z514rdc and D705/40m, Chromas Technology Corp., Rockingham, VT) were used to discriminate the fluorescence emission from the excitation. The excitation beam was generated with an argon-ion laser (Coherent Inc, Santa Clara, CA) coupled into a fiber to generate a clean Gaussian beam. After the fiber a positive lens was used to focus the beam onto the back focal plane of the objective. An intense bleach pulse was implemented by placing this lens onto a piezo stage (PIHera, $250\mu m$ range, PI, Karlsruhe, Germay) which was used to quickly move the lens along the optical axis, generating a tight laser beam of $\approx 1.2\mu m$ to bleach a small circular area in the sample. After bleaching, the piezo was moved back to the original position $\Delta t = 20\mu s$) to image fluorescence recovery.

Chapter 3

Image Correlation Spectroscopy and Fluorescence Recovery after Photobleaching in 1-D

In this thesis, we use fluorescence Image Correlation Spectroscopy (ICS)[69] and Fluorescence Recovery After Photobleaching (FRAP)[70] to extract individual motor information and also information about motors as they act in concert. ICS is a tool used in imaging microscopy to examine molecules dynamics in images. FRAP is used to describe the mobility of fluorescent molecules into bleached areas of varying geometries. In chapter 5, we perform ICS and FRAP experiments on motor proteins in membrane tubes. Because a membrane tube is much longer than it is wide, we approximate the tubes as a 1-D system. This chapter provides a detailed solution to the 1-D diffusion equation and subsequently describes the fluorescent behavior for fluorescent particles in 1-D: fluctuations in the case of ICS and recovery in the case of FRAP. We consider the cases relevant to the experiments in this thesis where particles either freely diffuse or move in a directed manner.

3.1 Image Correlation Spectroscopy, 1-D

Image Correlation Spectroscopy (ICS)[69] is an adaptation of Fluorescence Correlation Spectroscopy (FCS),[70] used for image analysis. The beauty of correlation spectroscopy lies in its ability to extract molecular and environmental information from a weak fluorescence signal, comparable to the background noise, using correlation analysis of the fluorescence fluctuations for very small samples of molecules. Here, we specifically adapt ICS to examine fluorescence fluctuations in a timeseries of images. The temporal autocorrelation of fluorescence fluctuations at a given point is a measure of the probability that, if a fluorescent molecule is detected at a time t, that a fluorescent molecule will also be at that point after a time $t + \tau$. The rate and shape of this probability as it decays in time provide information both about the mechanisms and the rate constants behind the processes driving the fluorescence fluctuations.[70] In this thesis, we use ICS to examine behavior of active fluorescent motors in membrane tubes.

In a typical fluorescence correlation experiment, the fluorescence signal $F(t)$ is acquired from a detection volume as a function of time. In our case, the fluorescence signal is a function of both time and space, $F(r, t)$ because we determine the fluorescence signal along a membrane tube in an image for each point in time. Because a membrane tube is much longer than it is wide, we approximate the tube as a 1-D line. At each point in space (each pixel along the line is considered individually), fluorescent particles may only enter or leave along that line. In our data, we consider each individual point along the line separately and only a single fluorescent species contributes to a fluorescent signal at that point. Thus, in a given pixel, we can describe the fluorescence intensity at a time t by:

$$F(t) = Q \int W(r)C(r,t)dr \qquad (3.1)$$

where $C(r,t)$ is the concentration of fluorescent species, Q is a product encompassing the absorbance, fluorescence quantum efficiency, and experimental fluorescence collection efficiency. $W(r) = I(r)S(r)T(r)$ where $I(r)$ describes the spatial intensity profile of the excitation light, $S(r)$ describes the spatial extent of the sample and $T(r)$ defines the area in the sample from which the fluorescence is measured. In the case of a sample illuminated by a focused laser beam with a Gaussian intensity profile,

$$I(r) = I_0 e^{-r^2/(2s^2)} \tag{3.2}$$

$$T(r) = \begin{cases} 1 & r \leq s \\ 0 & r > s \end{cases} \tag{3.3}$$

$$S(r) = 1 \tag{3.4}$$

so that

$$W(r) = \begin{cases} I_0 e^{-r^2/(2s^2)} & r \leq s \\ 0 & r > s \end{cases} \tag{3.5}$$

where s is the $1/e^2$ radius of the focused beam and I_0 is a constant.

The time-averaged fluorescence intensity for a single molecule in a pixel, $\langle F(t) \rangle$ is constant. The fluctuations of the fluorescence intensity $F(t)$ as it deviates from the average $\langle F(t) \rangle$ can then be described as:

$$\delta F(t) = F(t) - \langle F(t) \rangle \tag{3.6}$$

Then, the normalized autocorrelation function, $H(\tau)$ of the temporal fluctuations in the measured fluorescence signal $F(t)$ is:

$$H(\tau) = \frac{\langle F(t+\tau)F(t) \rangle}{\langle F(t) \rangle^2} = \frac{\langle F(\tau)F(0) \rangle}{\langle F(t) \rangle^2} \tag{3.7}$$

Fluorescence fluctuations are due to fluctuations in the concentration of particles at r and t from an average concentration over time $\langle C(r,t)\rangle_t$ ($\langle \rangle_t$ indicates a time average):

$$\delta C(r,t) = C(r,t) - \langle C(r,t)\rangle_t \tag{3.8}$$

so that the average fluorescence and fluorescence fluctuation can now be described as

$$\langle F(t)\rangle = \kappa Q \langle C(r,t)\rangle_t \int W(r)dr \tag{3.9}$$

$$\delta F(t) = \kappa Q \int \delta C(r,t)W(r,t)dr \tag{3.10}$$

Now the normalized autocorrelation function $H(\tau)$ of the fluorescence fluctuations can be described as:

$$H(\tau) = \frac{\int \int W(r)W(r')\langle \delta C(r,0)\delta C(r',\tau)\rangle_t dr dr'}{[\langle C(r,t)\rangle_t \int W(r)dr]^2} \tag{3.11}$$

where

$$\langle C(r,t)\rangle_t = \frac{1}{V_{\text{eff}}H(0)} = \frac{\int [W(r)/W(0)]^2 dr}{H(0)[\int (W(r)/W(0))dr]^2} \tag{3.12}$$

and V_{eff} is the effective volume that a fluorescent particle may pass through.

3.1.1 Solution for the diffusion equation: single-species 1-D diffusion

In order to solve eq. (3.12), we need to determine the concentration profile, $C(r,t)$, of an optical species diffusing laterally through a focal point of interest, with a diffusion coefficient D where we assume that D is independent of r. We determine this concentration profile by solving the diffusion equation for 1-D diffusion. The diffusion equation reads as:

$$\frac{\partial C(r,t)}{\partial t} = D\frac{\partial^2 C(r,t)}{\partial r^2} \tag{3.13}$$

The diffusion equation can be solved most easily in Fourier space, so that the concentration profile can be described as:

$$C(r,t) = \int A_k(t)e^{-ikr}dk \tag{3.14}$$

We define $C_k = A_k e^{-ikr}$ so that combining eqs. (3.13) and (3.14) taking both the time and space derivatives

$$\partial_t A_k e^{-ikr} = -k^2 A_k e^{-ikr} \tag{3.15}$$

Because the diffusion equation is a linear equation, the diffusion equation can be described as a linear differential operator acting on the concentration function C_k yielding a differential equation for the coefficient A_k:

$$\mathcal{L}[C_k(t)] = e^{-ikr}\partial_t A_k + DA_k k^2 e^{-ikr} = 0 \tag{3.16}$$

$$\partial_t A_k + DA_k k^2 = 0 \tag{3.17}$$

$$A_k(t) = A_k(0)e^{-Dk^2t} \tag{3.18}$$

Having determined $A_k(t)$ it is possible to construct a solution for the concentration profile

$$C(r,t) = \int A_k(0)e^{-Dk^2t}e^{-ik \cdot r}dk \qquad (3.19)$$

In order to determine $A_k(0)$, we take the Fourier transform of the intial condition $C(r,0)$

$$A_k(0) = \frac{1}{2\pi}\int \delta(r-r')e^{ikr}dr = \frac{1}{2\pi}e^{ikr'} \qquad (3.20)$$

We can then use Green's Function $(G(r,r',t))$, which tells how a single point of probability density intially at r' evolves in time and space to create a solution for the partial differential equation of eq. (3.13).

$$G(r,r',t) = \frac{1}{2\pi}\int e^{-Dk^2t}e^{-ik(r-r')}dk = \frac{1}{(4\pi Dt)^{1/2}}exp\left(\frac{-(r-r')^2}{4Dt}\right) \qquad (3.21)$$

The concentration profile and solution to the diffusion equation can now

be described:

$$C(r,t) = \int G(r,r',t)C(r',0)dr' \qquad (3.22)$$

3.1.2   The Autocorrelation profile: single-species 1-D diffusion

We can now solve $H(\tau)$, eq. (3.11), for a single diffusive species. We insert the solution for the concentration profile, $C(r,t)$ back into the

autocorrelation function, so that

$$H(\tau) = \frac{\int\int I_0 exp\left(\frac{-r^2}{2s^2}\right) I_0 exp\left(\frac{-r'^2}{2s^2}\right) \langle C(r,t)\rangle_t \frac{1}{\sqrt{4\pi D\tau}} exp\left(\frac{-(r-r')^2}{4D\tau}\right) dr\,dr'}{[\langle C(r,t)\rangle_t \int I_0 exp\left(\frac{-r^2}{2s^2}\right) dr]^2}$$

(3.23)

The autocorrelation function can ultimately be simplified to:

$$H(\tau) = \frac{1}{\langle C(r,t)\rangle_t \sqrt{4\pi D(\tau + \tau_D)}}$$

(3.24)

where $\tau_D = \frac{s^2}{D}$ and $\langle C(r,t)\rangle_t = \frac{1}{H(0)\sqrt{4\pi D\tau_D}}$

The final temporal autocorrelation curve for a single fluorescent species diffusing in 1-D can be described as:

$$H(\tau) = H(\infty) + H(0)\sqrt{\frac{\tau_D}{\tau + \tau_D}}$$

(3.25)

3.1.3 The Autocorrelation profile: 1-D diffusion with an additional directed motion

We also consider the case where a particles with a directed motion influences the fluorescence correlation profile, such as the case of motors walking in a directed fashion along a microtubule below a membrane tube. To account for an additional directed motion component in the autocorrelation curve, a term accounting for a velocity, V, in the system must be introduced into the diffusion equation:

$$\frac{\partial C(r,t)}{\partial t} = -V\frac{\partial C(r,t)}{\partial r} + D\frac{\partial^2 C(r,t)}{\partial r^2}$$

(3.26)

The Green's function accounting for V looks as follows:

$$G(r, r', t) = \frac{1}{(4\pi Dt)^{1/2}} exp\left(\frac{-(r - r' - Vt)^2}{4Dt}\right) \qquad (3.27)$$

where V is the velocity component of the system due to the particles with a directed motion. Solving the autocorrelation function as was done for the purely diffusional case, we arrive at the following:

$$H(\tau) = H(\infty) + H(0)exp\left(-\frac{\tau^2}{4\tau_V^2(1 + \frac{\tau}{\tau_D})}\right)\sqrt{\frac{\tau_D}{\tau_D + \tau}} \qquad (3.28)$$

where $\tau_D = \frac{s^2}{D}$ and $\tau_V = \frac{s}{V}$.

3.2   Fluorescence Recovery After Photobleaching, 1-D

Fluorescence Recovery After Photobleaching (FRAP) is a powerful tool for determining average particle behavior in an ensemble of fluorescently labeled particles.[71] An area of fluorescent particles at a concentration C_0 is rapidly bleached by an intense, localized laserbeam. Fluorescent particles moving into the bleached area recover the fluorescence: both the rate and the extent of the recovery provide information about the mobility of the fluorescent species. In this thesis, we consider the recovery of fluorescently marked motors into bleached regions both in the middle, and at the tip of membrane tubes. As in the case of the previous ICS derivations, we approximate a membrane tube as a 1-D line.

3.2.1   FRAP: Simple 1-D diffusion

The fluorescence recovery curve, $F_K(t)$ (fluorescence intensity as a function of time after bleaching) contains all the information necessary to

quantitatively describe the transport process. In the case of purely isotropic diffusion the fluorescence recovery curve looks as follows:

$$F_K(t) = \frac{q}{A} \int I(r) C_K(r,t) d^2 r \qquad (3.29)$$

where q is the product of the quantum efficiencies of laser light absorption, emission and detection, A is the attenuation factor of the beam during fluorescence recovery and $I(r)$ is the intensity profile of the bleach pulse. $C(r,t)$ is the concentration of unbleached molecules at a distance, r, and time t with the boundary condition: $C_K(\infty, t) = C_0$.[72]

Initially, we calculate the fluorescence recovery into a bleached region lying somewhere in the middle of a tube. The ends of the tube are considered to be far enough away from the bleached region that the tube is effectively infinite. Thus, the fluorescence can be recovered by fluorescent particles in reservoirs on either side of the bleached region. Calculating the concentration profile of fluorescent particles that recover a bleached region, $C_K(r,t)$ is mathematically very challenging. However, here, we follow the insightful method of Soumpasis[72] and, instead, calculate the concentration profile of the dark particles as they leave the bleached region, $C_K^*(r,t)$, given that:

$$C_K^*(r,t) + C_K(r,t) = C_0 \qquad (3.30)$$

We apply the following boundary conditions:

$$C_K^*(\infty, t) = 0 \qquad (3.31)$$
$$C_K^*(r,0) = C_0(1 - e^{-K}) \qquad (3.32)$$

where $r < w$ and w is the width of the bleached region. K is a bleaching

parameter defined as $K = \alpha T I(0)$ where $\alpha I(0)$ is the rate constant of the

first-order irreversible photobleach and T is the time of the bleach pulse. In the experiments considered in this thesis, all data is normalized prior to analysis, so that the terms $1 - e^{-K}$, q and A (in eq. (3.29)) simplify to 1.

We can again use the solution to the one-dimensional diffusion equation, eqs. (3.21) and (3.22), and describe the concentration profile of bleached particles moving from the bleached region of width, w as:

$$C_K^*(r,t) = \frac{1}{\sqrt{4\pi Dt}} \int_0^{w/2} C_K^*(r,0) exp\left(\frac{-(r-r')^2}{4Dt}\right) dr' \qquad (3.33)$$

We combine eqs. (3.29) through (3.33) to determine the intensity profile of the bleached region:

$$F(t) = 2 * \int_0^{w/2} C_0 - C_K^*(r,t) dr \qquad (3.34)$$

$$= C_0 w \left(1 - \frac{4\sqrt{t}\left(exp\left(\frac{w^2}{16Dt}\right) - 1\right)}{\sqrt{\tau_D \pi}} - Erf\left(\frac{\sqrt{\tau_D}}{4\sqrt{t}}\right)\right) \qquad (3.35)$$

where $\tau_D = \frac{w^2}{D}$ is the typical time for a fluorescent particle to re-enter the bleached region, in this case, driven by diffusion. The evolution of the fluorescence recovery profile in time is shown in figure 3.1a. As expected, higher diffusion times result in a slower recovery curve.

3.2.2   FRAP: 1-D diffusion at the tip of a membrane tube

In the case that a membrane tube is bleached at the very tip, the boundary conditions change. Fluorescent particles may only re-enter the bleached region from one direction, and likewise, particles may only exit
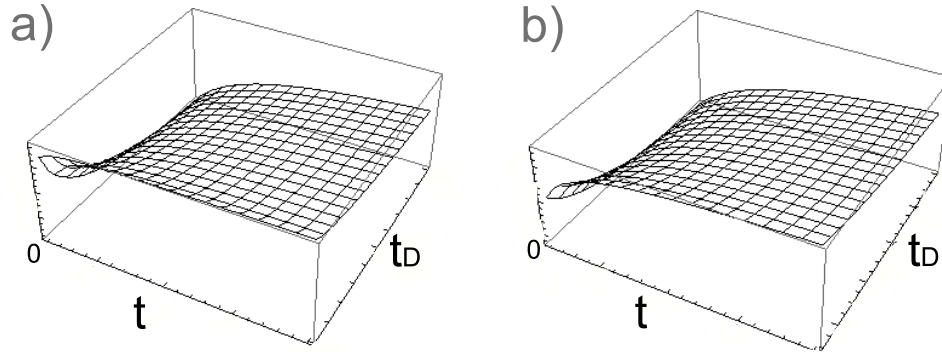
Figure 3.1: Example FRAP curves. a) FRAP curve for 1-D diffusion for different diffusion times, b) 1-D diffusion for a line that is bleached at one end (tip of a membrane tube).

the bleach region in one direction. The very tip of the membrane tube is described as a mirror that reflects any particles that reach it. Thus, the Green's function is written as:

$$G(r, r', t) = \frac{1}{\sqrt{4\pi Dt}} \left(exp\left(\frac{-(r-r')^2}{4Dt}\right) + exp\left(\frac{-(r+r')^2}{4Dt}\right) \right) \quad (3.36)$$

so that the equation for the concentration profile of the bleached particles

leaving the bleached region is:

$$C_K^*(r, t) = \frac{C}{2} Erf\left(\frac{r}{2\sqrt{Dt}}\right) - Erf\left(\frac{2r-w}{4\sqrt{Dt}}\right) \quad (3.37)$$

We solve for the FRAP intensity profile in time, as in the previous section, and find

$$F_{tip}(t) = 2C_0 w \left(1 + \frac{\left(1 - e^{\frac{\tau_D}{t}}\right)\sqrt{t}}{\sqrt{\tau_D \pi}} - Erf\left(\sqrt{\frac{\tau_D}{t}}\right)\right) \tag{3.38}$$

again, where $\tau_D = \frac{w^2}{D}$.

The curve is plotted in fig. 3.1b. The recovery is slower than for diffusion in the middle of the tube, because fluorescent particles may only enter the bleached region from one direction, and similarly, the bleached particles may only exit the bleached region in one direction.

The solutions derived in this chapter for the 1-D ICS and FRAP curves are applied to experiments later in this thesis in chapter 5.

Chapter 4

Bidirectional membrane tubes driven by nonprocessive motors

In cells, membrane tubes are extracted by molecular motors. Although individual motors cannot provide enough force to pull a tube, clusters of such motors can. Here, we use a minimal in vitro model system to investigate how the tube pulling process depends on fundamental properties of the motor species involved. Previously, it has been shown that processive motors can pull tubes by dynamic association at the tube tip. We demonstrate that, remarkably, nonprocessive motors can also cooperatively extract tubes. Moreover, the tubes pulled by nonprocessive motors exhibit rich dynamics. We report distinct phases of persistent growth, retraction and an intermediate regime characterized by highly dynamic switching between the two. We interpret the different phases in the context of a single-species model. The model assumes only a simple motor clustering mechanism along the length of the entire tube and the presence of a length-dependent tube tension. The resulting dynamic distribution of motor clusters acts as a velocity and distance regulator for the tube. We show the switching phase to be an attractor of the dynamics of this model, suggesting that the switching observed experimentally is a robust characteristic of nonprocessive motors. A similar system could regulate in vivo biological membrane networks.

Timon both designed the model and performed the simulations described in this chapter. [1]

4.1 Membrane tubes formed by nonprocessive motors

Dynamic interactions between the cell's cytoskeletal components and the lipid membranes that compartmentalize the cell interior are critical for intracellular trafficking. A trademark of these cytoskeletal-membrane interactions is the presence of continuously changing membrane tube networks. In *e.g.* the endoplasmic reticulum *in vivo*[73,74] and in cell-free extracts,[75–78] new membrane tubes are constantly formed while old ones disappear. Colocalization of these membrane tubes with the underlying cytoskeleton has led to the finding that cytoskeletal motor proteins can extract membrane tubes.[78] Motors must work collectively to extract membrane tubes,[49,50] because the force needed to form a tube, F_{tube},[79] is larger than the mechanical stall force of an individual motor.[80]

Here we investigate how the tube pulling process depends on fundamental properties of the motors involved. We use ncd, a motor protein highly homologous to kinesin, yet fundamentally different biophysically. Processive kinesin motors take many steps toward the plus end (to the cell periphery) before unbinding from a microtubule (MT); they have a duty ratio of ~ 1 (fraction of time spent bound to the MT).[3] Ncd, in contrast, is strictly non-processive: motors unbind after a single step[3] characterized by a duty ratio of ~ 0.15.[24] The ncd motor is unidirectional, moving towards the minus end (directed towards the nucleus) of MTs.[81] Though ncd is not involved in tube formation *in vivo*, we choose it as the model motor in our pulling experiments because of its nonprocessivity. We have studied ncd in MT gliding assays where motors are rigidly bound to a glass substrate and show linear, motor-concentration dependent MT gliding speeds, up to a saturation of $120 nm/s$. Due to their nonprocessivity, it is not *a priori* obvious that ncd motors can cooperatively pull membrane tubes.

We use Giant Unilamellar Vesicles (GUVs) as a substrate to study purified nonprocessive ncd motors *in vitro*. Our key findings are first,

that ncd motors readily extract tubes and second, that the tubes display more complex dynamics than those pulled by processive motors. We report the emergence of a distinct switching behavior: the tubes alternate between forward and backward movement with variable speeds, ranging from $+120 nm/s$ to $-220 nm/s$. This bidirectional switching is a phenomenon entirely absent in membrane tubes extracted by processive kinesin motors, which proceed at constant speeds ranging up to $400 nm/s$.

Though the bidirectional tube behavior we observe could result from motors forced to walk backward under tension,[82] thus far there is no experimental evidence to support this interpretation for unidirectional motors.[83,84] Moreover, retraction speeds are much higher than the maximum speeds measured in ncd gliding assays so that the reverse powerstroke would have to be much faster than the experimentally found speeds. We suggest a mechanism by which nonprocessive motors form clusters along the length of the entire tube, each of which is capable of withstanding the force due to tube tension. These clusters are dynamic entities that continuously fluctuate in motor number. The motors in the cluster at the tip of the membrane tube pull forward, until the fluctuating cluster size falls below a critical value and the tip cluster can no longer support the tube. We implement this model mathematically and show its necessary consequence is a distinct switching behavior in membrane tubes extracted at finite force. We analyze our experimental results in the context of this model and we predict the distribution of motor clusters all along the length of a membrane tube. The resulting dynamic distribution of motor clusters acts as both a velocity and distance regulator for the tube. Finally, we trace the evolution of the system through simulations and find the same behavior observed experimentally. In short, we show that not only can nonprocessive, unidirectional ncd motors act cooperatively to extract membrane tubes - they do so in a highly dynamic, bidirectional switching fashion. Our findings suggest an alternative explanation for *in vivo* bidirectional tube dynamics, often credited to the presence of a mixture of plus and minus ended motors.

4.2   Results: nonprocessive motors move membrane tubes bidirectionally

4.2.1   Experimental results

We investigate the influence of motor properties on membrane tube pulling with a minimal system where biotinylated motor proteins are linked directly via streptavidin to a fraction of biotinylated lipids in GUVs. Upon sedimentation to a MT-coated surface, and addition of ATP, motors extract membrane tubes from the GUVs. When we introduce nonprocessive ncd motors to our system, we see networks of membrane tubes formed. Fig. 4.1a shows a fluorescence time series of membrane tubes pulled from a GUV by ncd motors. The tips of the membrane tubes formed by ncd show remarkable variability. The arrow on the lower right hand corner of the image of fig. 4.1a indicates a retracting membrane tube and the remaining arrows show growing membrane tubes. In our experiments, we see not only tubes that persistently grow or retract, but also tubes that switch from periods of forward growth to retraction. We characterize these tube dynamics by tracing the tube tip location as it changes in time. Fig. 4.1b shows example traces of membrane tube tips in time: one of tube growth, one of retraction and two that exhibit a bidirectional movement. We verify that this bidirectional tube movement is unique to nonprocessive motors by comparing to membrane tubes pulled by processive motors. Under the same experimental conditions kinesins produce only growing tubes (fig. 4.1c). In the rare cases of tube retraction with kinesin, tubes snap back long distances at high speeds, at least 10 times faster than growth speeds (see example case in fig. 4.1d). In these cases, it is likely that the motors pulling the tube have walked off the end of the underlying MT.

We further quantify membrane tube dynamics by calculating instantaneous speeds for individual tip traces by subtracting endpoint positions of a window moving along the trace. As described in the materials and methods, we use a window size of $1s$ for the ncd, and $2s$ for the kinesin membrane tube tip traces. Fig. 4.2a shows an example of the resulting distribution and frequency of tip speeds for a single dynamically switch-
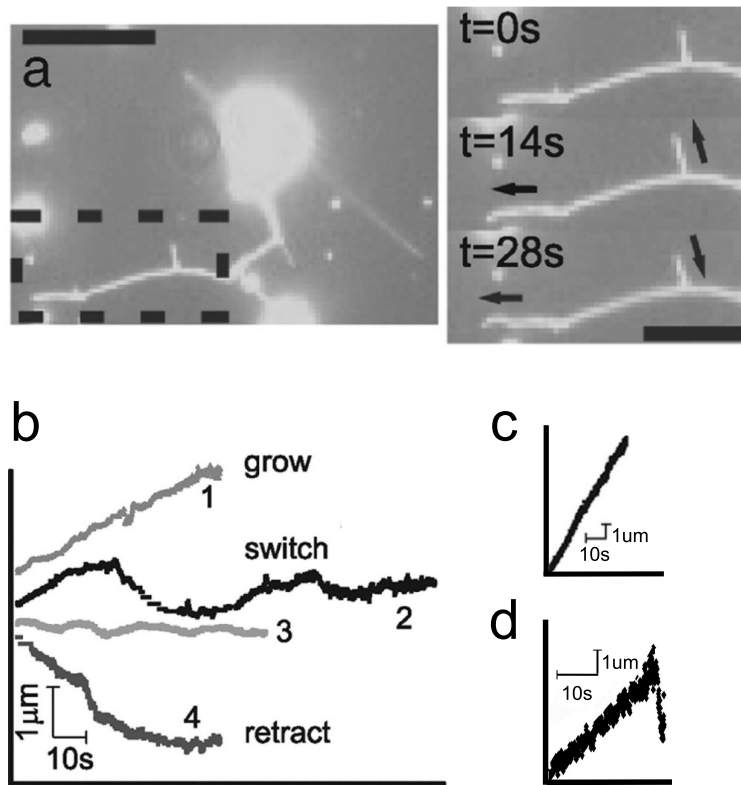
Figure 4.1: **Membrane tubes formed by nonprocessive motors** a) Fluorescence image of a membrane tube network extracted from GUVs by nonprocessive motors walking on MTs on the underlying surface. The time sequence images on the right show the detailed evolution of the network section within the dashed region on the left. Arrows indicate direction of membrane tube movement: the left arrows indicate a growing tube and the right arrows show a tube that switches between growth and retraction. (left scalebar, 10μm, right scalebar, 5μm). b) Example traces of membrane tube tips formed by nonprocessive motors as they move in time. There are three distinct behaviors: tube growth (1), tube retraction (4) and switching between growth and retraction (2 and 3), a bidirectional behavior. c) Tubes formed by kinesins grow steady high speeds. d) On the rare occasions that retractions occur in tubes formed by processive motors, tubes snap back long distances towards the GUV at speeds at least 10 times faster than growth speeds.

ing membrane tube formed by ncd (trace 3 from fig. 4.1b). Fig. 4.2b
shows the speeds for a membrane tube pulled by kinesin.
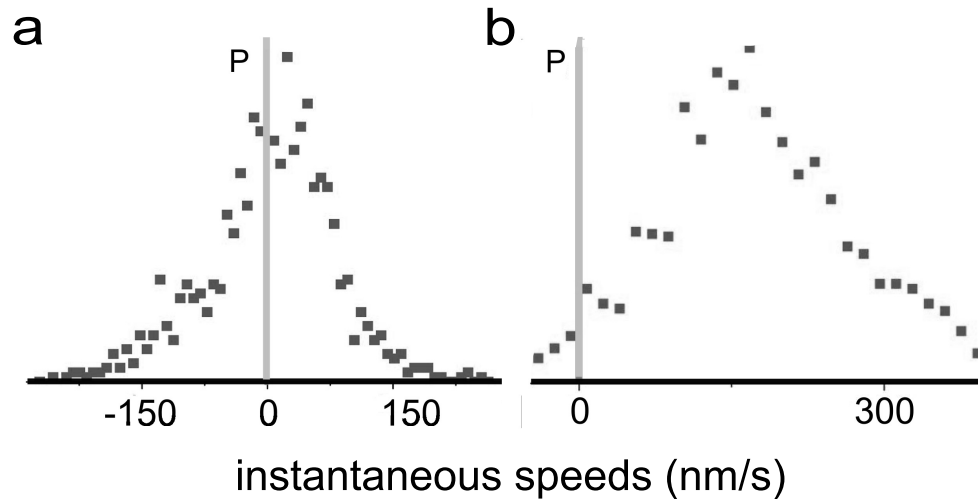
Figure 4.2: **speed distribution** a)The distribution of instantaneous tip
speeds for membrane tubes pulled by ncd is asymmetric and centers around
zero, with both positive and negative speeds. b) kinesin tubes move with only
positive speeds.

The speed distributions of tubes formed by kinesin and ncd are dis-
tinctly different where the speeds of tubes pulled by kinesin are dis-
tributed around a high positive speed. From gliding assays, one expects
that kinesin would pull membrane tubes at a constant $500 nm/s$. The
kinesin motors along the bulk of membrane tube are moving freely in a
fluid lipid bilayer, do not feel any force and may walk at maximum speed
toward the membrane tube tip. However, the motors at the tip experi-
ence the load of the membrane tube and their speeds are damped.[49,50,84]
The Gaussian-like distribution of speeds we find for kinesin elucidates
the influence of load on the cluster of motors accumulating at the tip
of the membrane tube. The distribution of speeds for ncd is asymmet-
ric and centered around zero with both positive and negative speeds.
Though bidirectional ncd mutants have been studied,[35] here we verify
that the ncd we use in our experiments are unidirectional. Gliding assays
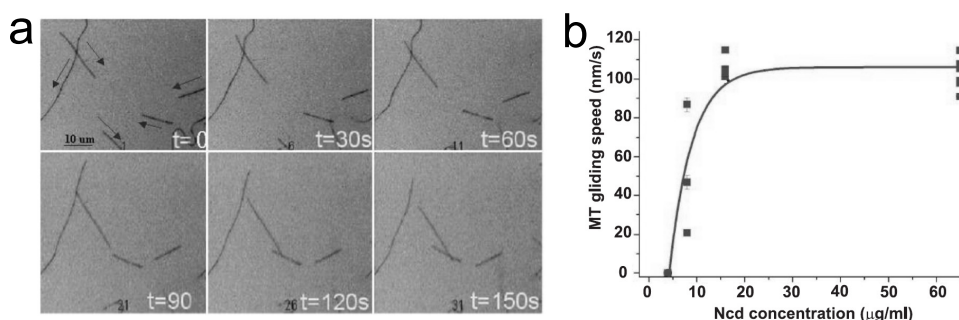
Figure 4.3: **Ncd motors gliding MTs** a)Time series showing unidirectional gliding by ncd motors, direction indicated by the black arrows b)MT gliding speed as a function of density of ncd on the glass surface.

have shown that MT gliding speeds decrease as surface motor densities decrease (fig. 4.3b), however, regardless of surface density (and consequently, load) MTs never switch direction as seen in the time series in fig. 4.3a. Hence, a simple damping of motor walking speed at the membrane tip, as in the case of kinesin, does not provide an explanation for the distribution of negative membrane tube speeds found in the tubes pulled by ncd. The unique tube pulling profile of the nonprocessive motors suggests that they provide a mechanism to mediate membrane retractions and hence, bidirectional tube dynamics.

4.2.2   Model

Koster *et al.*[49] show that membrane tubes can be formed as a result of motors dynamically associating at the tube tip. Collectively, the clustered motors can exert a force large enough to pull a tube. Evans *et al.*[47,48] find that this force scales as $F_{\text{tube}} \sim \sqrt{\kappa\sigma}$, where κ is the membrane bending modulus and σ the surface tension. Koster *et al.* predict a stable tip cluster to pull a tube, which has been verified experimentally by Leduc *et al.*[50] and supported by a microscopic model by Campàs *et al.*[51]

Although accurate for membrane tubes produced by processive motors, the kinesin model does not explain the bidirectionality in tubes formed by nonprocessive motors. There must be an additional regula-

tory mechanism for the tube retractions to explain the negative speed profiles seen in experiments with ncd. We propose a mechanism to account for these retractions wherein dynamic clusters form along the entire length of the tube. In the case of kinesin, motors walk faster than the speed at which the tube is pulled, and accumulate at the tip cluster.[49,50] However, due to their low duty ratio, nonprocessive motors do not stay bound long enough to walk to the tip of the membrane tube. Compared to freely diffusing motors ($D = 1 \ \mu\text{m}^2/\text{s}$),[50,53] a MT-bound motor (bound for approximately $0.1s$[23,24]) is stationary. Consequently, there are MT-bound motors all along the length of the tube. Local density fluctuations lead to areas of higher concentration of bound motors, resulting in the formation of many motor clusters, not just a single cluster at the tube tip.

In both cases, the cluster present at the tip has to be large enough to overcome F_{tube}. Because an individual motor can provide a force up to approximately $5pN$[80] and a typical F_{tube} is $25pN$,[49] a cluster must consist of at least several motors to sustain tube pulling. Statistical fluctuations can make the tip cluster too small to overcome F_{tube}, resulting in a retraction event. In the case of ncd, as soon as the retracting tip reaches one of the clusters in the bulk, the tube is caught, and the retraction stops. Growth can then resume, or another retraction event takes place. The process of clustering along the membrane tube, as illustrated in fig. 4.4a, and the associated rescue mechanism are absent from the mechanism that describes kinesin tube pulling.

In our model two different mechanisms drive forward and backward tube motion, so we expect two different types of characteristic motion profiles. Retraction is regulated by motor clusters that can form anywhere along the length of the tube: their locations are randomly taken from a uniform probability distribution. Consequently the distance between them follows an exponential distribution. The long steptime of MT-bound ncd motors allows us to temporally resolve the effect of the disappearance of clusters from the tube tip: individual retraction events. We therefore expect to recover this exponential distribution in the retraction distances. The forward velocity depends on the size of the cluster at
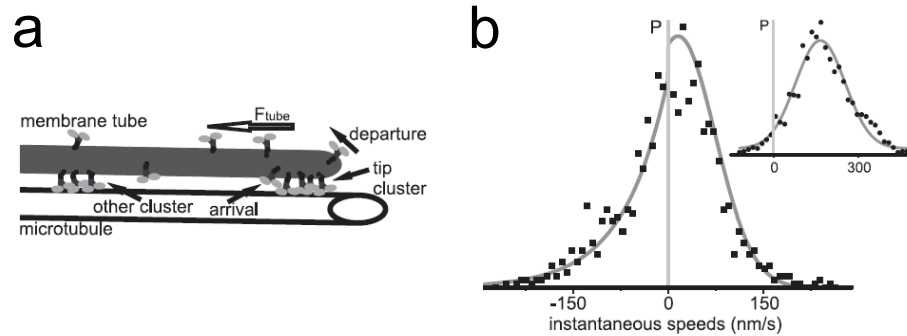
Figure 4.4: **Model for membrane tube bidirectionality** a) Sketch of nonprocessive motor clustering along a membrane tube. MT-bound nonprocessive motors are distributed along the entire length of the tube; local density fluctuations result in the formation of motor clusters. b) Distribution of instantaneous speeds of a bidirectionally moving membrane tube (trace 2 in Fig. 4.1b). The speed distribution can be described as a combination of two different processes: pulling by nonprocessive motors and tube tension induced retraction. Therefore the forward and backward speeds follow different distributions, as described by Eq. (4.1); the solid line shows the best fit of this distribution. (inset) Tubes pulled by processive kinesin motors follow a simple Gaussian speed distribution.

the tube tip.[3] Per experimental timestep there are many motors arriving at and departing from each cluster. Moreover, while taking a time trace we observe pulling by several different clusters of motors. Because there are many clusters in an individual trace, we can employ the Central Limit Theorem to approximate the distribution of cluster sizes by a Gaussian. If the number of motors in the tip cluster is large enough to overcome the tube force, the speed at which the cluster pulls scales with the number of excess motors: $v = A(n - c)$. Here, n is the number of motors, c the critical cluster size and A the scaling constant that depends on the turnover rate, stepsize and tube tension. The forward speed distribution will therefore inherit the Gaussian profile of the cluster size distribution, where the mean and spread of this distribution depend on the average tip cluster size. The probability density of the exponential distribution function depends on a single parameter λ, the mean retraction distance. The Gaussian distribution depends on both the mean $\langle n \rangle$ and the spread σ_n of the tip cluster.

The tube dynamics are described by the probability distribution of the tip displacement per unit time. From the individual probability densities for retraction and growth we find the combined density $f(\Delta L)$, the full probability density of advancing or retracting a distance ΔL:

$$f(\Delta L) = \begin{cases} (1 - Z)\frac{1}{\lambda} \exp\left(-\frac{|\Delta L|}{\lambda}\right) & \begin{array}{l} \Delta L < 0 \\ \text{(retract)} \end{array} \\ \frac{1}{\sigma_n \sqrt{2\pi}} \exp\left[-\frac{1}{2}\left(\frac{(x/s) - (\langle n \rangle - c)}{\sigma_n}\right)^2\right] & \begin{array}{l} \Delta L \geq 0 \\ \text{(advance)} \end{array} \end{cases} \tag{4.1}$$

where n is the size of the cluster at the tip, c is the minimal cluster size necessary to support the tube, and s the steplength, which is equal to the size of a MT subunit (8nm).[3] The normalization constant Z depends on $\bar{n} = \langle n \rangle - c$ and σ_n and is given by $Z = \frac{1}{2}\left[1 + \text{erf}\left(\frac{\bar{n}}{\sigma_n \sqrt{2}}\right)\right]$.

4.3 Discussion

From the experimental data we cannot determine $\langle n \rangle$ and c individually, but only speed profiles which scale with the difference $\bar{n} = \langle n \rangle - c$, the number of excess motors present in the tip cluster that actually pull. To

determine $A\bar{n}$, $A\sigma_n$ and λ, we make use of the fact that Z is the fraction of forward motions, providing a relation between $\bar{n}$ and σ_n. We then have a two-parameter fit for the entire speed distribution, or two single-parameter fits for the forward and backward parts of the total speed distribution.

We apply our model to experimental data and find that the different mechanisms for forward and backward motion accurately describe the experimental ncd tip traces (Fig. 4.4b). As predicted, kinesin motors only show forward pulling speeds, described by a Gaussian distribution (see inset Fig. 4.4b). The marked contrast in speed profiles of processive and nonprocessive motors is a signature of different biophysical processes: for processive motors a single cluster remains at the tip ensuring a constant forward motion whereas tubes pulled by nonprocessive motors are subject to alternating growth and retraction phases.

Growth and retraction are accounted for by the two different mechanisms in our model. Combined, they explain the three different types of observed behavior: growth, retraction, and switching between both. To unravel the relationship between the two mechanisms in describing membrane tube behavior, we plot the characteristic growth rate $A\bar{n}$ versus the characteristic retraction length λ.

Because a trace exhibiting switching behavior should have an average displacement of zero, we can derive a 'switching condition' from the probability distribution (4.1) by requiring the expectation value of ΔL to vanish. The line in the phase diagram where this switching condition is met by:

$$\lambda_s = A\bar{n}\frac{Z}{1-Z} + \frac{A\sigma_n}{\sqrt{2\pi}}\frac{1}{1-Z}\exp\left[-\frac{1}{2}\left(\frac{\bar{n}}{\sigma_n}\right)^2\right] \qquad (4.2)$$

where Z is the normalization constant from equation (4.1). In fig. 4.5a we plot the lines for which the switching condition holds for the range of values for $A\sigma_n$ we find in the experimental traces (50 nm/s $\leq A\sigma_n \leq$ 70 nm/s). We also plot the experimentally obtained values for $A\bar{n}$ and λ of the four traces given in fig. 4.1b. We clearly see different regimes: growing tubes have large average cluster size and small distances between clusters,

while retracting tubes show the inverse characteristics (small cluster size and large distance between clusters). The switching tubes are in between, in a relatively narrow region.

4.3.1 Simulations

The switching regime covers only a small part of the total available parameter regime in the phase diagram (fig. 4.5a). That we observe switching behavior in approximately 50% of the experimental traces indicates that these parameters are dynamic quantities that change over time. Our experimental observation times are too short to track these changes, but we can implement them in simulations. To introduce dynamics into our model, it is important to realize that the tube force F_{tube} is not independent of the tube length, an additional observation not yet integrated into the model. As tubes grow longer the vesicle itself starts to deform. Consequently, the tube force increases with the tube length, an effect also observed experimentally.[85]

As the tube force increases, larger tip clusters are required to continue pulling the tube. An immediate consequence of the force depending on the tube length is the emergence of a typical lengthscale, L_D. For a tube of length L_D the forward force exerted by an average motor cluster is balanced by F_{tube}. We can implement the force dependence in our model by introducing a Boltzmann-like factor that compares two energy scales: F_{tube} times the actual length of the tube $L(t)$ compared to the mean cluster force F_c times the typical length of the tube L_D. All constants are accounted for by L_D; we stress that choosing this form to incorporate a typical lengthscale is an assumption but that the qualitative results do not depend on the exact functional form chosen.

Tubes are initially pulled from motor-rich regions on the GUV. As a tube grows longer, clusters are spread further apart and the average cluster size decreases. The average retraction distance increases with increasing tube length, $L(t)$, and scales inversely with the total number of motors, $N(t)$, on the tube: $\lambda \sim L(t)/N(t)$. Similarly, the average number of motors at the tip scales with the total number of motors $N(t)$ and inversely with the tube length $L(t)$: $\langle n \rangle \sim N(t)/L(t)$. Therefore the
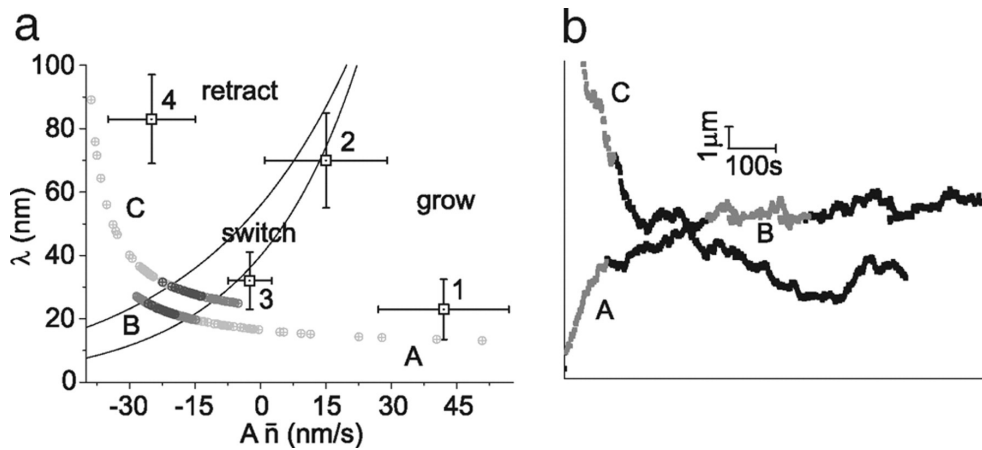
Figure 4.5: **Membrane tube phase diagram and simulations**. a) Phase diagram showing mean retraction distance λ vs. effective growth speed $A\bar{n}$. Lines represent the switching condition described by equation 4.2 for $A\sigma_n = 50$ nm/s and $A\sigma_n = 70$ nm/s. Squares 1-4 correspond to traces 1-4 in Fig. 4.1b, where the errors are determined by the mean square difference between the data points and the fit of distribution (4.1). As expected qualitatively, retracting membrane tubes fall well into the retraction regime with large retraction distance and small cluster sizes, while growing membrane tubes have large cluster sizes and smaller distances between clusters. b) Two simulated tube tip traces of a membrane tube pulled by nonprocessive motors. The time evolution of the parameters λ and $A\bar{n}$ for both traces is shown in the phase diagram (a), by circles getting darker in time. We see that both simulated tubes evolve towards a switching state. The highlighted sections of the simulated traces represent all possible characteristic behaviors of tubes pulled by nonprocessive motors.

total number of motors at the tip can now be expressed as:

$$N(t) = C2\pi R_0 L(t) e^{-L(t)/L_D}, \tag{4.3}$$

where C is the average motor concentration on the GUV and R_0 is the tube radius. Combined, equations (4.1) and (4.3) represent a system to describe the membrane tube dynamics caused by nonprocessive motors.

We perform simulations of membrane tubes extracted by nonprocessive motors using equation (4.3) with a given value for C, which is based on experimental values. We choose the simulation timestep to match the experimental sampling rate of 25 Hz. In each timestep we add Gaussian noise to the position to account for the experimental noise. In the simulations we observe two kinds of behavior: tubes that grow and subsequently retract completely after relatively short times, and tubes that evolve to a switching state. When we perform control simulations with a cluster size that is independent of the tube length, we find either fully retracting or continuously growing membrane tubes, never switching. Fig. 4.5b shows two examples of simulated switching traces. We follow the average number of motors at the tip $\langle n \rangle$ and the retraction distance λ as they change in time. The simulated evolution from growth to a switching state can be seen in the phase diagram fig. 4.5a. In the switching state, the tube length and total number of motors on the tube are essentially constant, and equation (4.2) is satisfied.

The highlighted sections of the simulated traces shown in fig. 4.5b represent all possible characteristic behaviors of tubes pulled by nonprocessive motors. The occurrence of all three types of behavior in a long simulated tube tip trace suggests that the experimental observations are snapshots of a single evolving process. The simulations indicate that all these processes eventually move to the switching regime. The switching state corresponds to a regulated tube length, determined by the GUV's motor concentration and surface tension.

4.3.2   Conclusion

We have shown that nonprocessive motors can extract membrane tubes. We find that at a given tension, these tubes exhibit bidirectional mo-

tion. We propose a model to explain our experimental findings wherein motors form clusters all along the length of the membrane tubes. The bidirectional membrane dynamics seen experimentally with nonprocessive motors can be accurately described by two different mechanisms for forward and backward motion. Future *in vitro* experiments will make use of single molecule fluorescence to directly quantify the locations of nonprocessive motors and motor clusters as they actively change in time. Our model predicts the emergence of motor clustering and an equilibrium tube length where tube bistability occurs. We propose that this mechanism with nonprocessive motors could also regulate tube dynamics *in vivo* and should be investigated.

4.4   Data Analysis

We have developed a Matlab® algorithm to trace the membrane tube growth dynamics by following the tip displacement as a function of time. The algorithm determines the intensity profile along a tube and extended beyond the tip. Fig. 4.6a shows an image from the timeseries of fig. 4.1a with a dashed line along and extending beyond the tip of the membrane tube. The algorithm determines the intensity profile along this dashed line. A sigmoidal curve fit to the intensity profile (also shown in fig. 4.6a) determines the tip location with a subpixel precision of $40nm$.

We trace tip locations for 7 individual kinesin-pulled membrane tubes (all growing, a single one showing a rapid retraction event) and 15 ncd tubes (by eye, the traces are divided into 7 growing, 3 retracting, and 7 switching). We calculate instantaneous speeds for individual tip traces by subtracting endpoint positions of a window moving along the trace (see fig. 4.6b). Initially we use a range of window sizes, from $0.68s$ to $12s$, to calculate instantaneous speeds from the tip traces.

We find that, for the ncd data, a window size of $1s$ is large enough to average out experimental system noise (signal due to thermal noise, fluorophore bleaching and microscope stage drift) but small enough to preserve the unique bidirectional features we see in tube data. At very small time windows, noise dominates the speed calculations, and results
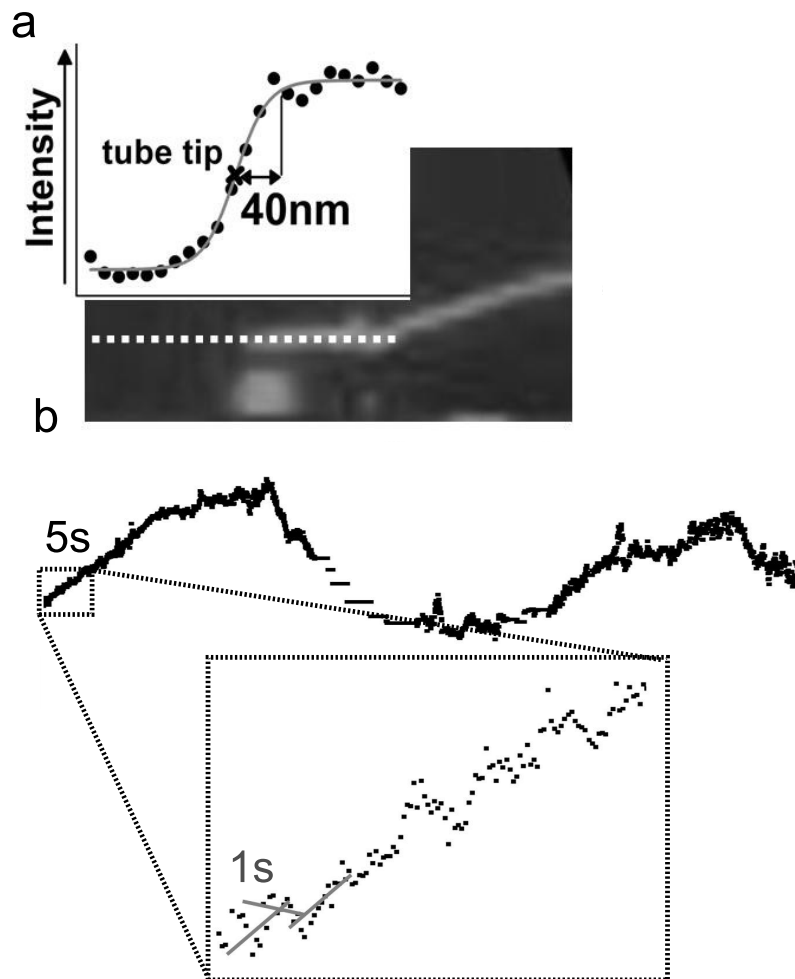
Figure 4.6: **Tip trace and speed analysis** a) To determine the location of the tip, we fit a sigmoidal curve to the intensity profile of a line along the tube extending into the bulk (dashed line). The method allows sub-pixel resolution of $40nm$. b) We move a $1s$ window over the length of a membrane tube trace. In each of the windows, we subtract endpoint positions of the data to determine the slope of the data in the window. Each of the slopes represents an instantaneous speed which we use to calculate the probability distribution of instantaneous speeds shown in fig. 4.2.
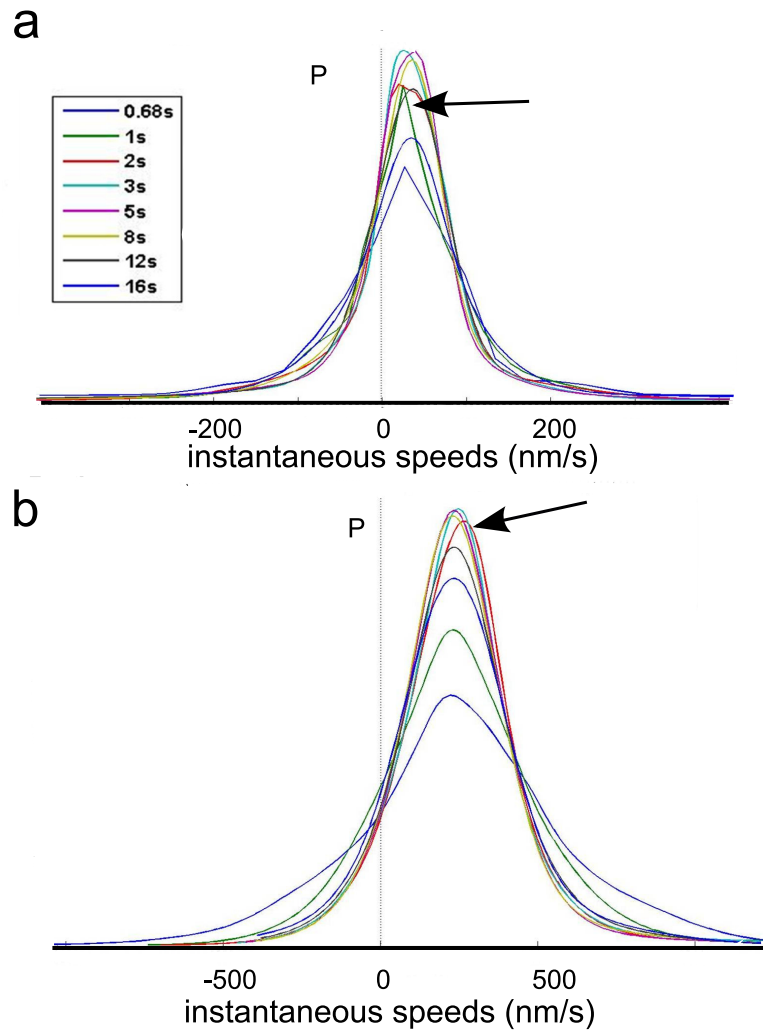
Figure 4.7: **Window size determination** Probability distribution of instantaneous speeds determined for different window sizes. a) For the tubes pulled by nonprocessive motors, a window size of 1s (indicated by the arrow) is large enough to average out experimental noise but does not average out unique features of the asymmetric speed profile. b) However, for kinesins, the speed profile from a moving window of 2s to 8s differs very little. We use the smallest window possible above the noise level: 2s indicated by the arrow.

in a broad distribution of the instantaneous speeds distribution. As we increase the time window, the distribution narrows until $2s$ and $3s$ windows where the data is overaveraged (the distribution begins to broaden again), and even larger window sizes smooth away the prevalent changes in speeds and directionality already qualitatively evident in the data (see fig. 4.7a).

For kinesin, however, the resulting speeds we find using a window size of $2s$ (minimum size for the kinesin data, the experimental signal is noisier than for the ncd data) differ very little from the speeds using up to an $8s$ window (fig. 4.7b). Because there is little variance in the speed of a tube pulled by kinesin motors, we would not expect changes in window sizes to influence the speed distribution (once the window is large enough to average out noise). Ultimately, we use small window sizes that are still large enough to average out experimental noise but preserve as much of the signal details as possible: $1s$ for ncd tip traces and $2s$ for kinesin traces, with steps of $0.04s$.

The inset of fig. 4.8 shows a trace of a membrane tube that is not actively moved by motors but whose signal is subject to thermal noise, fluorophore bleaching and microscope stage drift. We determine this trace using our tip-tracing algorithm and calculate instantaneous speeds in the same fashion as for active tube tips. Fig. 4.8 shows the resulting distribution of instantaneous speeds, with a spread of approximately $23nm/s$. The average noise for all of our experimental traces is $\approx 40nm/s$, a value incorporated both into the analysis of the tube traces and used in simulations. We fit all of the instantaneous speed profile for tubes formed by nonprocessive motors and extract both the average retraction distance, λ, and the mean forward speed, $A\bar{n}$. The data for tubes that retract (triangles), switch (circles) and grow (squares) are shown in fig. 4.9. The data from the different regimes group into different areas of the plot, as expected from the explanation of the phase diagram of fig. 4.5a. However, the original data traces were simply separated qualitatively by eye. From the plot, we can distinguish, in a quantitative way, the behavior regime of the membrane tubes.
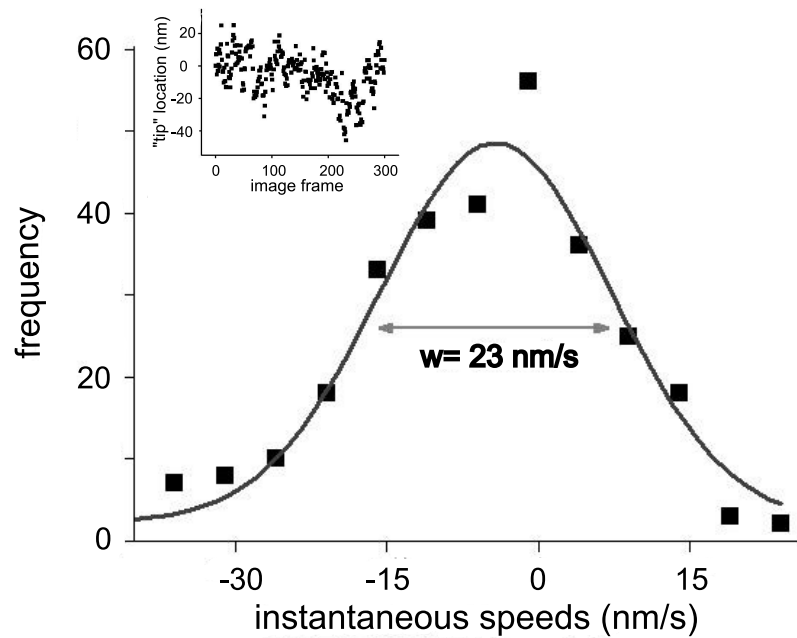
Figure 4.8: **Noise** The data are shown for tubes that retract, switch and grow. At first glance one can already see a separation of the data points within the graph.
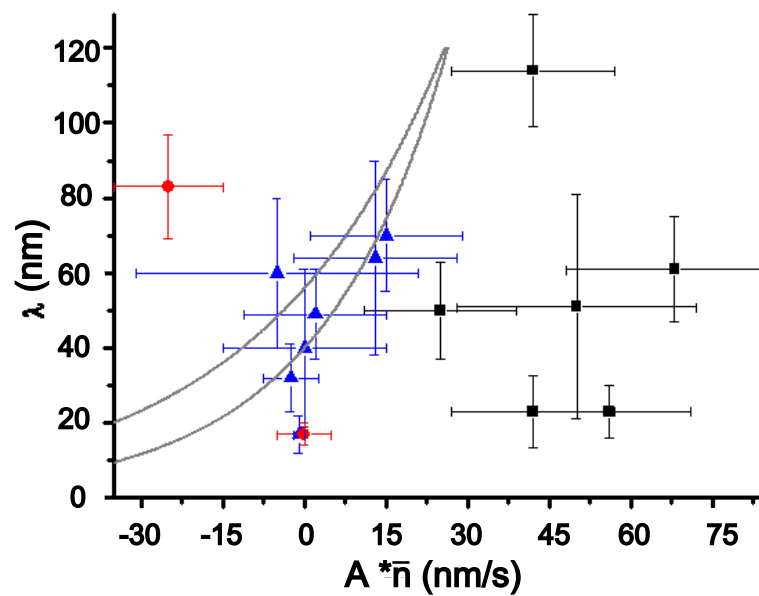
Figure 4.9: λ **vs.** $A\bar{n}$ **for all tubes formed by nonprocessive motors**
The data are shown for tubes that retract, switch and grow. At first glance
one can already see a separation of the data points within the graph.

Chapter 5

Nonprocessive motor dynamics at the microtubule membrane tube interface

Key cellular processes such as cell division, membrane compartmentalization and intracellular transport rely on motor proteins. Motors have been studied in detail on the single motor level such that information on their step size, stall force, average run length and processivity are well known. However, in vivo, motors often work together, so that the question of their collective coordination has raised great interest. Here, we specifically attach motors to giant vesicles and examine collective motor dynamics during membrane tube formation. Image correlation spectroscopy reveals directed motion as processive motors walk at typical speeds ($\leq 500nm/s$) along an underlying microtubule and accumulate at the tip of the growing membrane tube. In contrast, nonprocessive motors exhibit purely diffusive behavior, decorating the entire length of a microtubule lattice with diffusion constants at least 100 times smaller than a freely-diffusing lipid-motor complex in a lipid bilayer ($1\mu m^2/s$); fluorescence recovery after photobleaching experiments confirm the presence of the slower-moving motor population at the microtubule-membrane tube interface. We suggest that nonprocessive motors dynamically bind and unbind to maintain a continuous interaction with the microtubule. This dynamic and continuous interaction is likely necessary for nonprocessive motors to mediate

bidirectional membrane tube dynamics reported in chapter 4. [1]

5.1 Nonprocessive motors in membrane tubes

The emergent collective behavior of motor proteins plays an important role in intracellular transport. Processive kinesin motors, motors that take many steps along a microtubule (MT) before dissociating, collectively generate enough force to extract membrane tubes from membrane compartments *in vitro*.[49,50,86] Surprisingly, as discussed in chapter 4, nonprocessive ncd motors, which only take a single step before dissociating from a MT, can also extract membrane tubes where tubes show distinct phases of persistent growth, retraction, and an intermediate regime characterized by dynamic switching between the two.[32]

In order to understand the dynamics of nonprocessive motors as they mediate membrane tube movement, we investigate the general mobility of these motors at the MT-membrane tube interface. We use a minimal *in vitro* model system where motors are specifically attached to a fluorescently labeled lipid on Giant Unilamellar Vesicles (GUVs) to directly probe motor dynamics during membrane tube formation. We examine both processive and nonprocessive motors as they collectively extract membrane tubes from the GUV. Because processive motors walk unidirectionally on MTs at effectively constant speeds, we expect their behavior to show characteristics of a system with directed motion. Since nonprocessive motors, though also unidirectional, only take a single step and then unbind from the MT, their dynamics are likely to appear diffusive. We adapt fluorescence image correlation spectroscopy (ICS)[69] for temporal analysis and, along with fluorescence recovery after photobleaching (FRAP),[70–72] extract information about dynamic properties of the motors as they drive membrane tube dynamics. In contrast to previous experiments where GUVs were coated with $\approx 3000\text{motors}/\mu m^2$,[32] the number of motors on the GUVs here is reduced dramatically to $\approx 125\text{motors}/\mu m^2$ (comparable to[50]). This reduction in motor density allows for adequate ICS and FRAP analysis. However, fewer nonprocessive motors result in

much slower membrane tube dynamics: nonprocessive motors form networks on the scale of hours whereas previously at high motor densities the networks formed in tens of minutes.[32]

Our key findings are that nonprocessive motors interacting with the MT distribute themselves over the entire length of the membrane tube while processive motors accumulate at the tip of the tube. Processive motors walk along the MT towards the tip and exhibit a signature of directed motion at typical motor walking speeds, $\leq 500nm/s$. In contrast, nonprocessive motors at the MT-membrane tube interface show purely diffusive behavior with diffusion constants 10^{-3} times smaller than motors freely diffusing in a membrane tube ($1\mu m^2/s$). We interpret the small diffusion constant as an indicator that motors continuously dis- and reconnect the membrane tube to the MT. Based on our previously proposed model in chapter 4,[32] a dynamic but continuous connection between the membrane tube and the MT is essential for nonprocessive motors to drive membrane tube movement.

5.2   Results

We investigate collective motor behavior during membrane tube formation with a minimal system where biotinylated motor proteins are linked directly via streptavidin to a small fraction of Rhodamine-labeled biotinylated lipids in GUVs.[63] GUVs are allowed to sediment to a surface coated with taxol-stablized MTs, and, after the addition of ATP, motors extract membrane tubes from the GUVs.

The images in fig. 5.1a and fig. 5.2a show sums of all the frames in a movie of active membrane tube networks formed by nonprocessive ncd (fig. 5.1a) and processive kinesin (fig. 5.2a) motors. The tube networks follow the turns and bends of the randomly oriented and crossing MT mesh on the surface indicating that motors actively form the networks by walking on MTs. These networks are formed on the scale of minutes by processive motors, and on the scale of hours by nonprocessive motors. Because ncds have an ATP turnover rate (and hence walking speed) approximately 100x slower than kinesins,[24,87] the differences in timescales
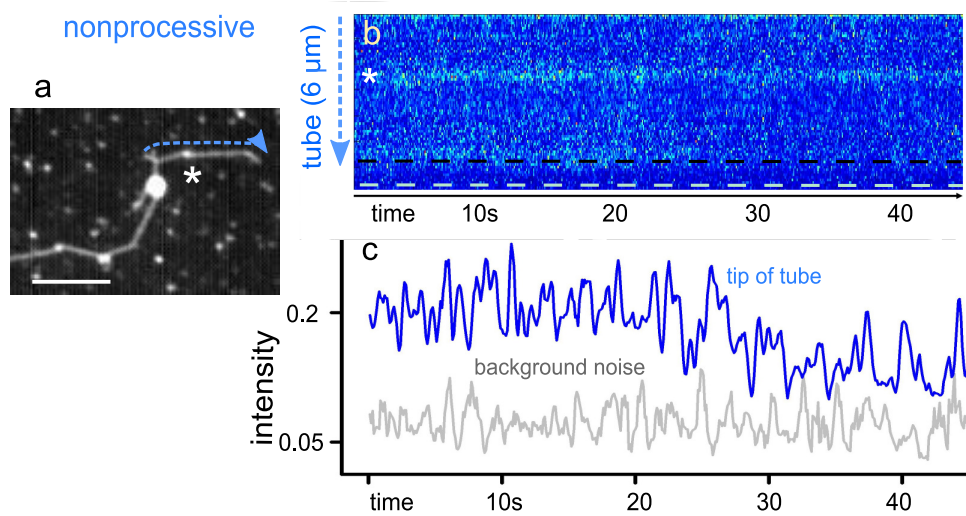
Figure 5.1: **Motor activity in membrane tubes** a) Sum of images in a movie of a membrane tube network formed by nonprocessive (ncd) motors b) Kymograph of line indicated in (a) showing the evolution of the fluorescence profile, and hence the ncd motor locations, along the membrane tube in time. Ncd motors do not show any directed motion nor is there any emergent pattern. c) Fluorescence intensity profile along the tip of the membrane tube (indicated by the dashed line in (b)) formed by nonprocessive motors measured for each point in time. The fluctuations in fluorescence intensity in the tip region are above the background noise shown in gray.
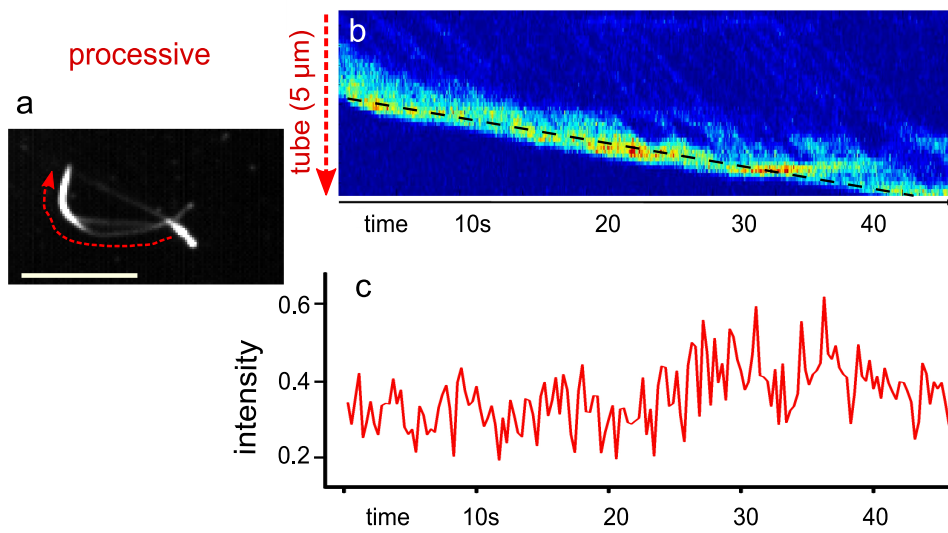
Figure 5.2: **Motor activity in membrane tubes** a) Sum of images in a movie of a membrane tube network formed by processive (kinesin) motors b) Kymograph of line indicated in (a) showing the evolution of the fluorescence profile, the kinesin motor locations, along the membrane tube in time. Kinesins walk toward and accumulate at the tip of the membrane tube. c) Intensity profile along the tip of the growing membrane tube as indicated by the dashed line in (b). As expected for processive motors, motors accumulate at the tip of the tube, resulting in an increase of the fluorescence intensity.

for the formation of tube networks are to be expected. Individual images in the movie are illuminated for $100ms$, and acquired at $10Hz$. A single pixel width line extends along the length of the membrane tube (dashed line) and we observe the fluorescence fluctuations in time along this line. The resulting kymograph shows the time evolution of the fluorescence profile of this line along the tube (fig. 5.1b: nonprocessive, fig. 5.2b: processive). Processive motors consistently move towards the tip of the membrane tube. The processive motors in fig. 5.2a walk at typical speeds ($\approx 400nm/s$) along the underlying MT and accumulate at the tip of the more slowly growing membrane tube ($\approx 50nm/s$). The accumulation occurs because motors at the tip have to work against tension in the membrane tube and are slowed while motors in the rest of the tube may walk freely through a lipid bilayer and are only slowed as clusters grow large enough so that motors impede each others' paths.[50] Nonprocessive motors, however, decorate the entire length of the microtubule lattice. Nonprocessive motors along the membrane tube do not show any directed motion, nor is there any emergent pattern. However, we can see there are motor dynamics indicated by fluorescence fluctuations (above the background noise shown in gray in fig. 5.1c) shown in the fluorescence intensity profile at the tip of the tube in the black line of fig. 5.1c.

5.3 Fluorescence image correlation analysis

Correlations in the fluorescence fluctuations from the data of e.g. fig. 5.1b and fig. 5.2b can be used to provide information about the mechanisms and rate constants behind the processes that drive the fluorescence fluctuations. We expect different driving processes from processive and nonprocessive motors. Processive motors should create a system with a directed motion as motors walk along a MT towards the tip of a membrane tube as shown in fig. 5.2a. In contrast, because nonprocessive motors continuously bind to and unbind from the MT, we would expect them to exhibit a diffusive-type behavior. There are two motor populations in the experiments considered here: motors that interact with

the MT, and motors that freely diffuse in the membrane. However, the population of motors that freely diffuse in the membrane tube move very quickly on the scale of our experimental measurements[50] and likely do not contribute to the majority of the dynamics on the s timescale so we do not consider them here. In order to probe the dynamics of motors at the MT by considering the fluctuations in fluorescence signal along a membrane tube, we examine the influence of diffusion and a directed motion on the autocorrelation function. First, we assume that a membrane tube is much longer than it is wide so that it can be approximated as a one-dimensional system. Thus, fluorescence correlations can also be examined in 1-D. The normalized temporal fluorescence autocorrelation $H(\tau)^{[69,70]}$ for a single pixel along the membrane tube is

$$H(\tau) = \frac{\langle F(t+\tau)F(t)\rangle}{\langle F(t)\rangle^2} \tag{5.1}$$

The derivations of the 1-D autocorrelation curves are described in detail in the supplementary material. For a system dominated by a single diffusive species, the autocorrelation curve is:

$$H(\tau) = H(\infty) + H(0)\sqrt{\frac{\tau_D}{\tau + \tau_D}} \tag{5.2}$$

where $\tau_D = \frac{s^2}{D}$, s is the width of a single pixel and D is the diffusion constant.[70] For a system with a directed motion, the autocorrelation is described as:

$$H(\tau) = H(\infty) + H(0)exp\left(-\frac{\tau^2}{4\tau_V^2\left(1 + \frac{\tau}{\tau_D}\right)}\right)\sqrt{\frac{\tau_D}{\tau_D + \tau}} \tag{5.3}$$

where $\tau_V = \frac{s}{V}$ and V is the velocity of the particles in the system.

In order to verify that a one-dimensional approximation is a reasonable assumption when analyzing our data, we simulate data for both nonprocessive and processive motors in membrane tubes. In the case of the nonprocessive motors, we allow motors to diffuse at the MT-membrane tube interface with a known diffusion constant D. Fig. 5.3a shows an

example of the resulting kymograph for a tube formed by nonprocessive motors. The resulting, spatially averaged, autocorrelation curve over time is shown in fig. 5.3c (black line). The curve is well-fit by the 1-D model autocorrelation curve for a system with a single diffusive species, shown in grey. The diffusion constant extracted from the fit is the same as the diffusion constant used in the simulations: for simulations where $D = .160\mu m^2/s$, the resulting value from the autocorrelation curves give $D = .164 \pm .017\mu m^2/s$ ($n = 3$).

Processive motors walk towards the tip of a membrane tube, along a microtubule with a velocity, V. Fig. 5.3b shows an example kymograph from a simulation of processive motors walking towards the tip of a (non-moving) membrane tube. Clusters can be seen forming and walking towards the tip (in the direction of the arrow on the left). The black line in fig.5.3d is a plot of the temporal autocorrelation curve, averaged over space. The fluctuations in the signal at longer timelags arise because the times at which motors pass through a point can appear correlated. These fluctuations, however, oscillate around 1 and do not change the fit at lower timelags. The curve is fit by the 1-D autocorrelation curve for a system with a directed motion, shown in grey. The velocity from the model fit matches the velocity used in the simulations: for simulations where $V = 1000nm/s$ the value from the autocorrelation curves yield $V = 973 \pm 60nm/s$ ($n = 3$). (The processive motor simulations, for a system with a directed motion, are based on the simulations described in chapter 6. The fact that we impose a boundary at the tip changes the system from being purely a system with flow and contributes to the unusual correlation peaks and valleys at longer timescales.)

The exponential decay in eq. 5.3 for a system with a directed motion can be seen at longer correlation times (fig. 5.4a lower curve) while in a system driven by diffusion the feature is absent (fig. 5.4a upper curve). We have confirmed this with the simulations. In the experimental data, the processive motors should yield a correlation curve that shows features of a directed motion in the autocorrelation curve and nonprocessive motors a diffusive-type behavior.

We consequently examine the experimental data and determine the
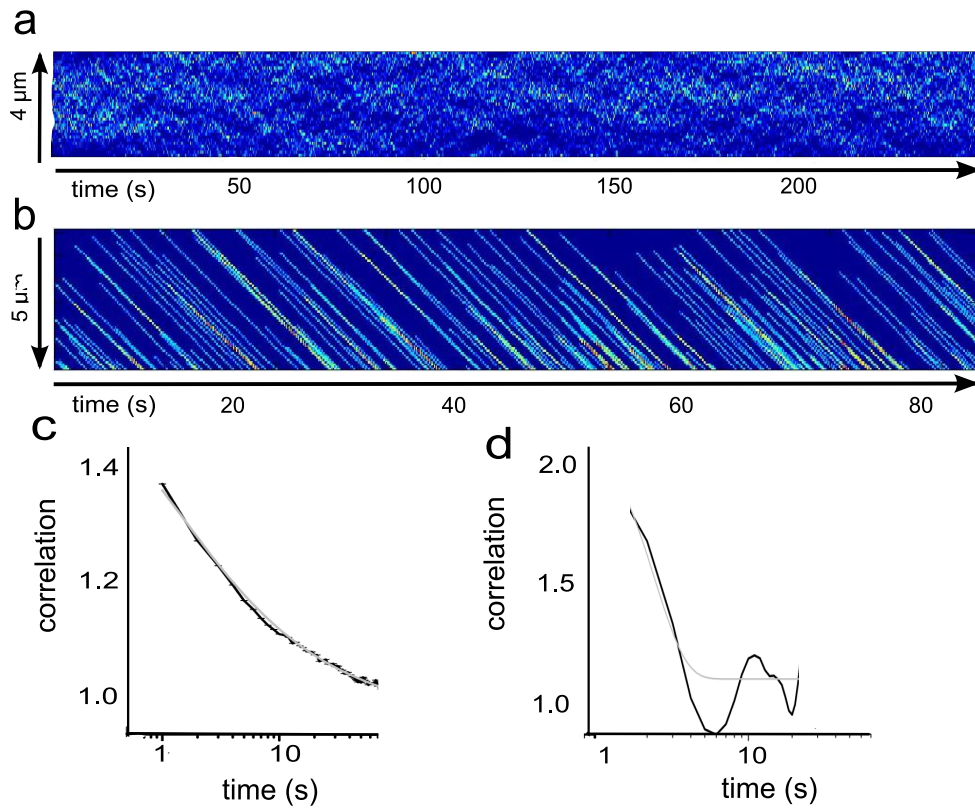
Figure 5.3: **Simulated data for 1-D ICS analysis** a) Kymograph of a simulated membrane tube formed by nonprocessive motors. The signal arises from nonprocessive motors at the MT-membrane tube interface. b) Kymograph of a simulated tube formed by processive motors. Processive motors form clusters as they walk towards the tip of a membrane tube. c) Space-averaged temporal autocorrelation of the nonprocessive motors in the kymograph of (a). The curve is fit with the 1-D model autocorrelation curve for a system with a single diffusive species, shown in grey. The diffusion constant extracted from this model is in agreement with the diffusion constant used in the simulations. d) Space-averaged temporal autocorrelation of the processive motors in the kymograph of (b). The curve is fit with a 1-D model autocorrelation curve for a system with a directed motion (gray line). The velocity from t_V is in agreement with the velocity used in the simulations.
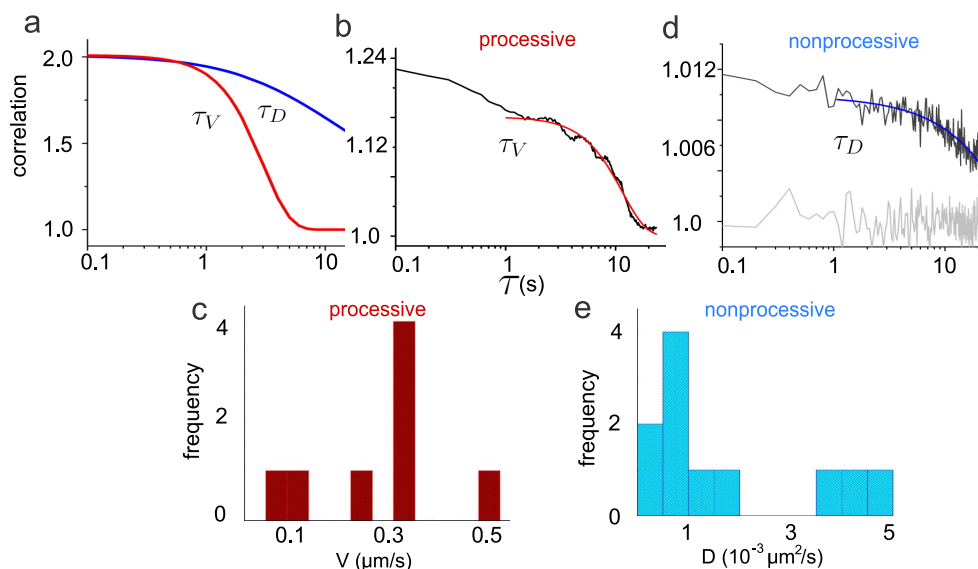
Figure 5.4: **1-D temporal autocorrelation curves for diffusion and flow**. a) The upper curve is a model curve for a system that is driven purely by single-component diffusion where $\tau_D = 12s$ and $D = 1*10^{-3}\mu m^2/s$. The lower curve is a model curve for a system with a directed motion, where $\tau_V = 0.78s$ and $V = 140nm/s$. The most striking difference between the two curves occurs at longer correlation times where the curve with a directed motion follows an exponential decay to zero. b) Average autocorrelation curve for the points along a tube formed by processive motors (see line in fig. 5.2a). The curve is characteristic for a system of particles that have a directed movement with an exponential decay at longer times. The curve is described by a one-dimensional model for a system of particles with a direction motion of velocity, where $\tau_V = 0.54 \pm 0.07$ and $V \approx 200nm/s$: motor speeds as they walk on the MT towards the tip of a membrane tube. c) Histogram of speeds extracted from fits to the autocorrelation curves by a 1-D model for a system with directed movement. d) Autocorrelation curve for nonprocessive motors in a membrane tube (see line in fig. 5.1a). The curve is fit with a diffusive model for fluorescence correlations in a one-dimensional tube to yield a diffusion constant for nonprocessive motors that interact with the microtubule lattice. Here $\tau_D = 29 \pm 4s$ and $D \approx 0.4*10^{-3}\mu m^2/s$. The signal is compared to background noise (lower gray curve) to indicate that the signal is above the noise of the system. e) Histogram of diffusion constants from fits to the autocorrelation curves for membrane tubes formed by nonprocessive motors. The resulting diffusion constants are very small, on the order of $10^{-3}\mu m^2/s$.

autocorrelation for each pixel along a membrane tube individually, and average the resulting autocorrelation curves. The data for processive kinesin motors, excluding the saturated tip region, show a signature for a system with a directed motion in the autocorrelation curves (fig. 5.4b). Because we expect all motors that interact with the MT lattice to walk, we assume that diffusion at the MT lattice does not play a role. Thus, we fit the autocorrelation curve where $\tau_D \to \infty$ and determine that $\tau_V = 0.54 \pm 0.07s$ which gives $V \approx 200 nm/s$ using eq 3. The fit does not extend to small timelags (fig. 5.4b) because our model assumes a system with a single motor fraction. We do not consider the motors freely diffusing in the membrane tube that contribute to very fast timescale fluorescence signals. Thus, at small time lags in the FCS data, the signals between the two motor populations mix and the experimental data deviates from the model. Fig. 5.4c shows a histogram of processive motors speeds in different experimental membrane tubes. The spread in speed is to be expected because as motors locally accumulate they can impede each other's path to slow each other down and there is also error in the fits from the model.

Fig. 5.4d shows the autocorrelation curve for a tube pulled by nonprocessive motors. It should be noted that the experimental curves are well above the noise shown in gray in fig. 5.4d. We fit the autocorrelation curves obtained from the experimental data of tubes pulled by nonprocessive motors with the 1-D model driven by diffusion, eq. 2. The autocorrelation curve shows the dynamics of the slower fraction of molecules in the system: motors interacting with the MT. The resulting diffusion time for the nonprocessive motors from the fit in fig. 5.4d is $\tau_D = 29 \pm 4s$ so that $D \approx 0.4 * 10^{-3} \mu m^2/s$. In general the diffusion constants for nonprocessive motors interacting with the MT are on the order of $10^{-3} \mu m^2/s$ as shown in fig. 5.4e. Surprisingly, the values of the diffusion constant are very small as compared to the diffusion constant of a motor-lipid complex freely moving in a lipid bilayer, $\approx 1 \mu m^2/s$.[50]

We also examine spatial fluorescence correlations to rule out the possibility that motors artificially aggregate or show preferential binding regions on the MT. The normalized autocorrelation function, $H(\rho)$, for

spatial correlations in the measured signal $F(r)$ along the membrane tube
is described as:

$$H(\rho) = \frac{\langle F(r + \rho)F(r)\rangle}{\langle F(r)\rangle^2} \qquad (5.4)$$

To determine $F(r)$ we extend a line along the length of a membrane tube,
not extending into the vesicle nor into the tip region. We determine the
intensity profile along this line at each point in time and determine if
there is any spatial correlation in the fluorescence signal along the tube,
$H(\rho)$. The point spread function of the microscope can be described as:
$PSF \approx exp\left(\frac{x^2}{2\sigma^2}\right)$ where σ is the width of the point spread function. In
our experimental setup $\sigma = 110nm$. We fit the spatial autocorrelation
curves with the autocorrelation for the point spread function and find the
values of σ are comparable. The value of σ from the spatial correlation for
processive motors is $199 \pm 9nm$ and 149 ± 6 for the nonprocessive motors.
The comparable σ values imply that on length scales comparable to the
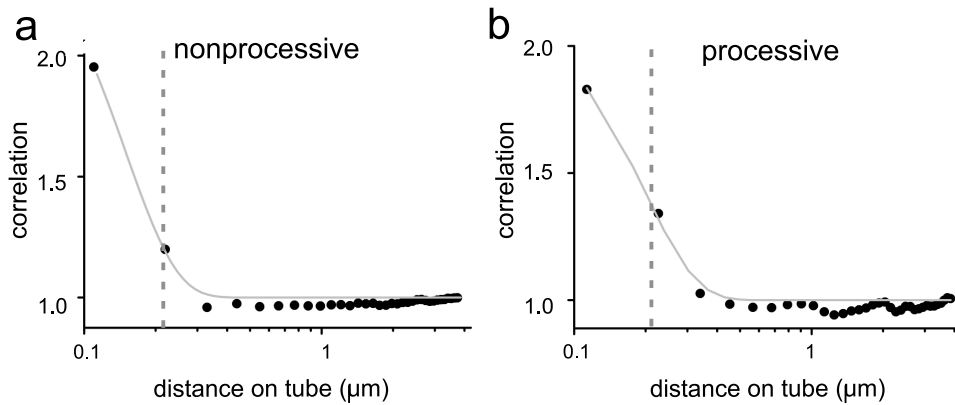
Figure 5.5: **Spatial correlations of motors along membrane tube** a)
Average spatial autocorrelation for nonprocessive motors in a membrane tube.
The correlation decays to zero at the distance of the point-spread-function of
the microscope, indicating no spatial correlation. b) The spatial correlation
for processive motors also decays to zero at the distance of the point-spread-
function of the microscope, also indicating a lack of spatial correlation.

point-spread-function of the microscope motor clusters are not spatially
correlated. The absence of correlation indicates that artificial aggregation

and preferential binding do not influence the motor dynamics we observe
(see supplementary material for detailed analysis).

5.4   Fluorescence recovery analysis

Until now, the fraction of motors freely-diffusing in the membrane tube
have been ignored. However, to fully understand the motor dynamics in
the system, we need to know how motors diffusing in the membrane tube
behave and what fraction of the motors interact with the MT. To probe
the population of freely-diffusing motors, we used a technique that is
commonly exploited to examine the dynamics of diffusive particles: Flu-
orescence Recovery After Photobleaching (FRAP).[70–72] We bleach the
motors in a small region of the membrane tube and examine the fluo-
rescence recovery in that region. The timeseries in fig. 5.6a shows the
fluorescence of a membrane tube formed by nonprocessive motors that
is bleached at $t = 0$ in the circular region. Over time, the fluorescence
in the bleached region is recovered. Examples of normalized curves for
bleached regions of nonprocessive motors in membrane tubes both in the
absence and presence of MTs are shown in fig. 5.6b. Membrane tubes
in the absence of MTs are formed by flow. We examine the half-time
for recovery for tubes with processive motors, nonprocessive motors and
tubes where motors do not interact with a MT and are freely diffusing.
The half times for bleached membrane tubes are shown in fig. 5.6c. The
squares show the fluorescence recovery for a membrane tube (bleached in
the middle) that does not interact with a microtubule below, so that all
of the motors freely diffuse in the membrane tube. The average time scale
for the half-time for recovery (solid symbols in fig. 5.6c), $\tau_{1/2}$, for all of
the tubes is approximately the same suggesting that, in contrast to the
ICS experiments, free diffusion of fluorescent motors in the membrane
tube dominates the recovery signal.

The FRAP data also provides values for the diffusion constant of the
motors diffusing in the membrane and the fraction of motors at the MT-
membrane tube interface. To extract this information from the data, we
again approximate a membrane tube as a line. Because FRAP probes fast
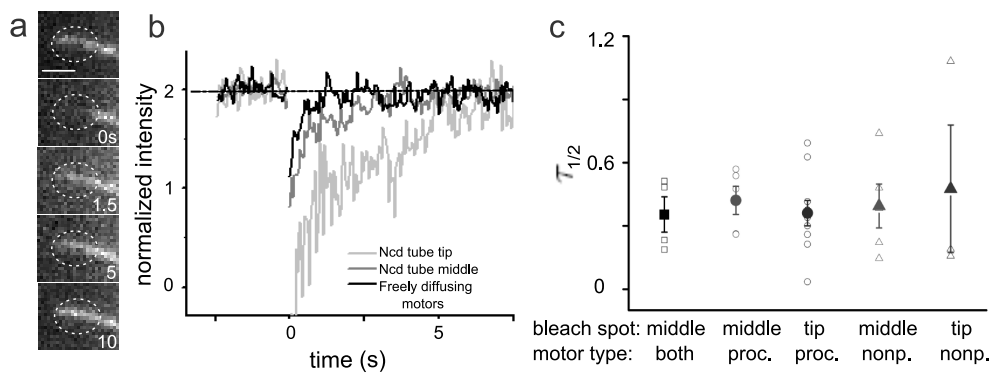
Figure 5.6: **FRAP curves** a) Timeseries showing the fluorescence recovery of nonprocessive motors in a membrane tube before and after bleaching of a region at the tip of the tube (dashed circle), bar= $2\mu m$. b) FRAP curves for nonprocessive motors at a region in the middle of a membrane tube and at the tip of a membrane tube. c) We can examine the half-time for recovery of fluorescence into the bleached region, $\tau_{1/2}$. The plot shows this half-time for recovery for tubes that have only freely diffusing lipid-motor complexes (hollow squares, solid square represents the mean), tubes with processive motors either bleached in the middle of a tube or at the tip (circles), and tubes with nonprocessive motors either bleached in the middle or at the tip (triangles).

timescales, the recovery curves can be described for a 1-D model system with a single diffusive species, the motors diffusing in the membrane tube. The normalized fluorescence intensity, $F(t)$, from a 1-D recovery model for a single diffusive species of initial concentration C_0 in a bleached region of width w in the middle of a membrane tube is:

$$F(t) = C_0 w \left(1 - \frac{4\sqrt{t} \left(exp \left(\frac{w^2}{16Dt} \right) - 1 \right)}{\sqrt{\tau_D \pi}} - Erf \left(\frac{\sqrt{\tau_D}}{4\sqrt{t}} \right) \right) \qquad (5.5)$$

where $\tau_D = \frac{w^2}{D}$ and D is the diffusion constant.

Motors bleached at the tip of a tube encounter a reflecting boundary so that the recovery curve is as follows:

$$F_{tip}(t) = 2C_0 w \left(1 + \frac{\left(1 - e^{\frac{\tau_D}{t}} \right) \sqrt{t}}{\sqrt{\tau_D \pi}} - Erf \left(\sqrt{\frac{\tau_D}{t}} \right) \right) \qquad (5.6)$$

Fig. 5.7a shows an example FRAP curve for nonprocessive motors in a membrane tube that has been bleached at the tip of the tube. The curve is fit (solid line in fig. 5.7a) with eq. 5.6 to determine τ_D. Here, $\tau_D = 126 \pm 18s$ and $w = 1.87 \mu m$ so that $D = .027 \mu m^2/s$. The diffusion constant for this tube and diffusion constants for other nonprocessive motor membrane tubes are plotted in the scatterplot of fig. 5.7b.

As expected in tubes that do not interact with a MT, all the motors are fast-moving and these freely-moving motor-lipid complexes have a diffusion constant of $\approx 1 \mu m^2/s$, indicated by the black circles. The value is in agreement with measurements from FRAP experiments on a lipid bilayer on a surface (the bottom of a GUV).[50] The FRAP curves from nonprocessive motors in various tubes yield different diffusion constants, ranging from $10^{-2} m^2/s$ to $1 \mu m^2/s$. The diffusion constants often have values below the value of purely freely-diffusing motors because the
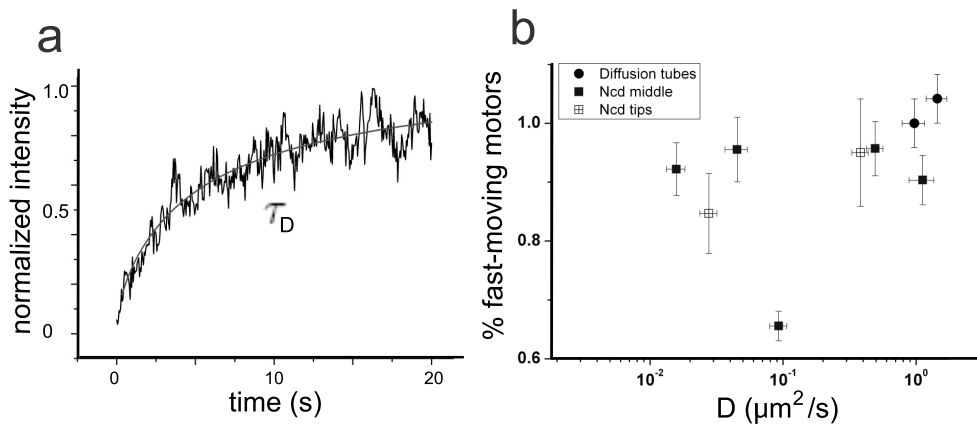
Figure 5.7: **FRAP data** a) FRAP curve for nonprocessive motors in a membrane tube fit by a 1-D model for recovery due to diffusion. The model gives $\tau_D = 126 \pm 18s$ and $D = 0.027\mu m^2/s$. b) Scatterplot of diffusion constants measured for nonprocessive motors in membrane tubes using FRAP. Motors freely diffusing in a membrane tube have diffusion constants of $1\mu m^2/s$ (circles) and nonprocessive motors interacting with a membrane tube show a reduced diffusion constant. When motors interact with a MT on the surface the percentage of freely diffusing motors is reduced, as indicated by changes in the percentage of fast-moving motors on the y-axis.

fraction of motors at the MT-membrane tube interface also contribute to the signal. Also, as predicted, the fraction of motors that interacts with the MT varies from tube to tube but the fraction of freely-diffusing motors is always higher.

5.5   Nature of the slowly diffusing fraction

The values of the diffusion constants from FRAP, $10^{-2} - 1\mu m^2/s$, and the values derived from ICS, $10^{-3}\mu m^2/s$, measurements describe the dynamics of two different populations: slow-moving motors at the MT-membrane tube interface and fast-moving motors that diffuse freely in the membrane. Because each timestep in the ICS measurements lasts $100ms$, the signal from any fast-moving motors is averaged out over the entire tube. Thus, ICS measurements only probe longer timescale behavior at the MT-membrane tube interface, a slow-moving fraction of the motor population. The diffusion constants on the order of $10^{-3}\mu m^2/s$ are an indicator of motor behavior at the MT lattice: likely reflecting repeated motor binding and unbinding.

FRAP measurements probe both this slow-moving fraction as well as the fast-moving fraction of the motor population: the motors that freely diffuse in the membrane. The net diffusion constant from FRAP can be called a measure of an effective "interrupted diffusion" constant, D_{eff} where $D_{\mathrm{eff}} = D_{\mathrm{f}}/(1 + \frac{k_{\mathrm{on}}}{k_{\mathrm{off}}})$.[88] Here, D_{f} is the diffusion constant for motors freely diffusing in the membrane, k_{on} is the rate at which motors bind to the MT lattice and k_{off} the rate at which motors leave the lattice. We can consider k_{off} to be constant, its value is known from kinetic studies on ncd, $k_{\mathrm{off}} = 10s^{-1}$.[24] We expect k_{on} to be high because the membrane tube is close to the MT and motors may easily bind to the MT. The high k_{on} results in the smaller D_{eff} that we measure.

The ICS measurements, however, only provide information about the fraction of molecules on the MT lattice, the slow-moving fraction. We speculate that the small diffusion constant could result from two possible scenarios. First, motors could unbind and quickly rebind again within a same pixel on timescales faster than we probe with the ICS experiments.

Cooperative binding, where the probability that a motor will bind next to a motor already bound on a MT is much higher than a motor randomly binding on the MT, could facilitate quick rebinding. Second, motors could stay bound to the MT for longer periods of time than the $0.1s$ expected based on earlier kinetic studies.[24] The depletion rate of ATP for our experiments does not allow ADP to compete with ATP until several hours into an experiment. Thus, we assume that neither long ADP nor nucleotide-free MT-bound states contribute to the signal of slow dynamics at the MT lattice. In this case, the relatively long dwell-times for motors on the MT are likely facilitated by binding.[54] The consequence of this small diffusion constant in relation to the emergent collective behavior of tube extension and shrinkage[32] is that motors are continuously available to anchor the membrane tube to the MT.

We have shown with ICS and FRAP that nonprocessive motors show a diffusive behavior at the MT lattice with a very small diffusion constant. The small diffusion constant measured on the MT is an indicator of a continuous binding and rebinding of motors to the MT lattice. Continuous reorganization of motors along the lattice would allow a stochastic clustering-mechanism to arise. Such clustering has been predicted to be the driving force behind dynamic membrane tube transport by nonprocessive motors as seen in previous studies.[32]

5.6 Data Analysis: FRAP

Fig. 5.8 shows an example of data traces acquired during a FRAP experiment. These traces are: the background signal (background), the signal along the entire tube in addition to the bleached region (entire tube), and the signal from the bleached area itself (bleached region). To simplify the analysis of our data, we normalize the raw data before fitting the data to extract diffusion times. Initially, the background signal is subtracted from all the other signals (entire tube and bleached region). From the background-subtracted "bleached region" signal, we determine the diffusion times for a region in the middle and at the tip of a membrane tube (derivation described in detail in the supplementary material).

The fraction of fast-moving fluorescent particles from the background-subtracted signals is determined using the following relationship:

$$A = \frac{I_{\text{entiretubebeforebleach}} * I_{\text{bleachedregionafterbleach}}}{I_{\text{entiretubeafterbleach}} * I_{\text{bleachedregionbeforebleach}}}. \tag{5.7}$$

The value of A, the fast-moving fraction, is a measure of how many particles are free to move on the timescale of one of our experiments. The value can be small either because dark particles slowly leave the bleached region so that fluorescent particles may not enter the region or that other fluorescent particles are also slow to enter the bleached region. Both cases are caused by the same behavior: low mobility of the fluorescent particles (motors).
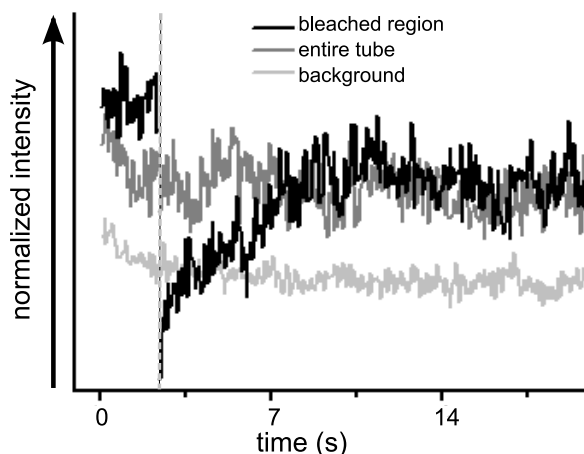
Figure 5.8: **Raw FRAP data** Proper normalization of a fluorescence recovery curve requires a sample of the background signal (background), the signal along the entire tube in addition to the signal in the bleached region (entire tube), and the signal of the bleached area (bleached region). The background signal is subtracted from the signal in the bleached region and the entire tube so that the data is normalized for acquisition bleaching. Then, the fast-moving fraction of molecules, A can also be calculated from the data in the figure according to eq. 7.

Chapter 6

Kinesin recycling in stationary membrane tubes

Collections of motors dynamically organize to extract membrane tubes. The tubes dynamically grow but often pause or change direction as they traverse an underlying microtubule network. We find, in stalled membrane tubes in vitro, motor clusters begin to accumulate and reach the tip of a membrane tube at regular time intervals. The average times between cluster arrivals scale linearly with the time over which motors depart from the tip suggesting that motors are recycled towards the tip. Numerical simulations of the motor dynamics in the membrane tube and on the MTs show that the presence of cooperative binding between motors quantitatively accounts for the clustering observed experimentally. Cooperative binding along the length of the MT, cooperative unbinding at the tip and a nucleation point at a distance behind the tip define the recycling period. Based on comparison of the numerical results and experimental data we estimate a binding probability and concentration regime where the recycling phenomenon occurs. [1]

6.1 Processive motors in non-moving membrane tubes

Transportation within the cell is driven by mechanoenzymes, motor proteins. Motors not only deliver cargo, in the form of vesicles and other proteins, as they walk on cytoskeletal tracks, but they are also responsible for continuous reorganization of membrane compartments. Because of their essential cellular function, the physical properties of individual motor proteins have been heavily investigated. For example, the kinesin motor transports cargo to the plus ends of microtubules (MTs) as an ATPase,[3] it can walk at speeds up to $1 \mu m/s$,[15] stalls at forces greater than $5pN$,[9,11,14] and takes anywhere between $50 - 100$ steps on a MT before it dissociates from the MT.[89] However, there is more and more evidence that cooperation between multiple motors in cargo movement is critical for regulating cargo transport in cells.[30,90–92] Though we know much about individual motor proteins, our understanding of how motors behave as collectives is still limited.

To study collective motor dynamics, we use a minimal model system where kinesin motors are specifically attached to giant unilamellar vesicles (GUVs). When the motor-coated GUVs encounter a surface decorated by MTs, in the presence of ATP, the motors extract membrane tubes.[49] Because a single motor can only provide $5pN$ of force[9,11,14] and deformation of a vesicle to extract a membrane tube requires $\approx 25pN$,[47,93] motors must work together to share the load. Motors have been shown to dynamically associate at the tips of growing membrane tubes so that collections of kinesins are readily available to pull the tube.[49,50] These motor dynamics have been observed in growing membrane tubes. However, *in vivo*, membrane tubes can be seen pausing and changing direction regularly (see movie of membrane tubes *in vivo*[74]). The dynamics of motor proteins in membrane tubes that are paused have not yet been investigated.

Here, we examine the dynamics of processive kinesin motors in stalled membrane tubes *in vitro*. We find that motors repeatedly congregate en

route to the tip of the membrane tube at regular time intervals. Moreover, we find that the average time for clusters to form scales linearly with the time over which motors depart from the tip. We explain the clustering mechanism by cooperative binding: motors have a higher probability of binding to the MT nearby motors that are already bound, than to an unpopulated area of the MT. With a simple, 1-D lattice model, we are able to describe the motor behavior and further probe the dynamics with numerical simulations. Simulations that account for cooperative binding in concert with cooperative unbinding of motors at the tip of the membrane tube and a cluster nucleation point behind the tip where the membrane tube is held to the MT by a few motors, recover the linear relationship between average arrival time and tip decay time found in experiments. From simulations we estimate the probability of cooperative binding to be 0.24 and determine a critical number of motors on the tube, $25 < N < 120$, necessary for this phenomenon to occur in non-moving tubes.

6.2 Experimental results: kinesins cluster towards the tip at typical timescales

We use a minimal *in vitro* model system where kinesin motors are specifically attached to a fluorescently labeled lipid[63] on Giant Unilamellar Vesicles (GUVs) to directly examine motor dynamics during membrane tube formation. We use kinesins (kinesin-1) because they are responsible for *in vivo* transport of vesicles and membrane material towards the plus end of MTs. *In vitro*, kinesins have been shown to collectively extract membrane tubes from a GUV as they walk on underlying MTs.[49,50] The groups of kinesins walk towards the plus-end of the underlying MT with speeds of $370 \pm 43 nm/s$, comparable to MT gliding speeds for the kinesin construct we use. The motors accumulate at the tip of the growing membrane tube where their speeds are damped by the tube-pulling force.[49,50] At some point, motors encounter the end of a MT (or a MT junction) and the tube can no longer be pulled forward, though the motors are still highly active.
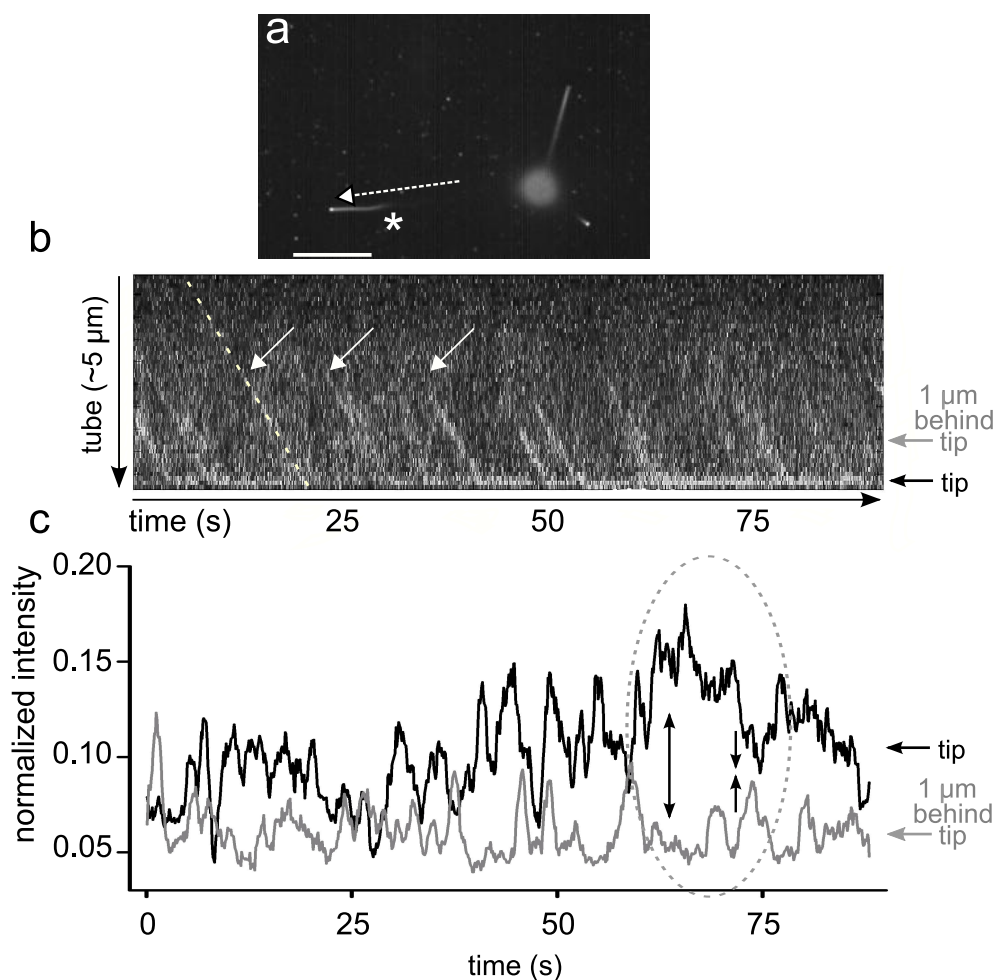
Figure 6.1: **Kinesin dynamics in membrane tubes** a) Membrane tube
network formed by kinesin motors. The image is a sum of a series of images
tracing fluorescent kinesin dynamics in a membrane tube network. The star
indicates the point at which the membrane tube is connected to the underlying
microtubule (MT). bar= $5\mu m$. b) Kymograph tracing the motor dynamics in
the direction of the arrow of (a) in time. The arrows indicate examples of
new kinesin motor clusters. c) Trace of the intensity profile in time at the
tip and $1\mu m$ behind the tip, indicated by the arrows in (b). The two signals
are generally anticorrelated so that when there is a high intensity at the tip
the intensity behind the tip lowers. The region in the dashed circle shows two
distinct anticorrelated parts of the intensity signals, indicated by the arrows.
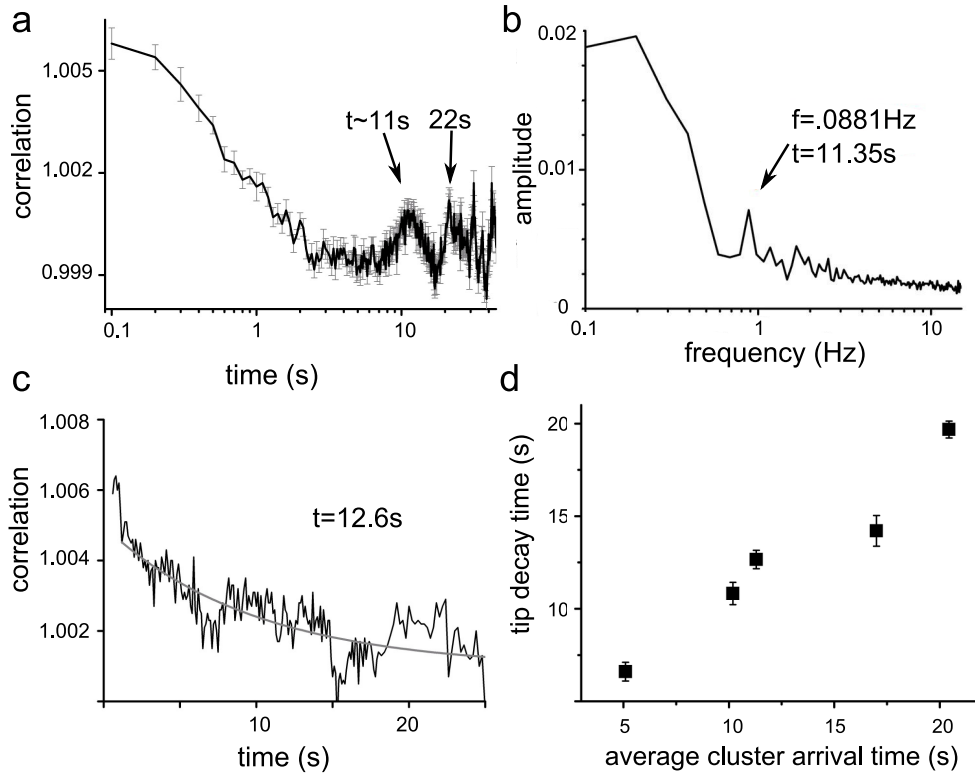
Figure 6.2: **Motor cluster timescale** a) Autocorrelation curve in time, averaged for all points along the membrane tube of fig. 6.1a and b. The correlation curve shows distinct peaks at $\approx 11s$ and $22s$. b) The peak around $11s$ is confirmed by a peak in the power spectrum. c) Autocorrelation curve at the very tip of the membrane tube. The curve is fit with an exponential decay. The decay time of this fit tells the time, $12.6 \pm 0.5s$, it takes for clusters at the tip to dissipate. d) Plot of the decay (release) time of the motors at the tip of a tube vs. the typical cluster arrival time for different tubes. Different tubes have different characteristic times, but the times at which motor clusters form is linearly related to the release of motors from the tube where $t_{decay} = (0.85 \pm .04)t_{arrival}$.

Fig. 6.1a shows the sum of a series of images of a tube network formed by kinesin motors. The fluorescence signal appears wherever there are motors bound to the MT. At and beyond the star in fig. 6.1a, the fluorescence rapidly decreases because the membrane tube is lifted from the surface and not attached to the MT. Though the tube is stationary, motors are still highly active in the tip region close to the MT. We trace the motor positions through time as they walk towards the tip of the membrane tube, along the tube in the direction of the dashed arrow. In the resulting kymograph (fig. 6.1b), the motors congregate to form clusters. The signal of motors at the tip is anticorrelated with the signal of motors behind the tip as shown by the intensity traces at the tip and $1\mu m$ behind the tip in fig. 6.1c. The region within the dashed oval shows two examples, indicated by the arrows, where the signal is anticorrelated. The anticorrelation suggests that the majority of the motors in the system collect into clusters in the same region so that, for example, when all the motors are bound to the MT near the tip, there are no motors available to bind behind the tip.

The distinct clusters of motors arrive at the stationary tip at regular time intervals. In the kymograph in fig. 6.1b, motors cluster approximately every 10 to 11s. We verify the times quantitatively by examining the time autocorrelation of the fluorescence signal from the motors (fig. 6.2a). The curve is an average of all correlation curves along the length of the membrane tube. The autocorrelation curve shows distinct peaks at 11s and 22s. This period of 11s is confirmed by examination of the power spectrum of the signal in fig. 6.2b. Also visible in the kymograph in fig. 6.1b, the motors appear to accumulate on average about $2\mu m$ behind the tip. In all stationary tubes we observe, we find that motor clusters accumulate and move towards the tip at regular time intervals. We compare this arrival time to the time at which motor clusters leave from the tip. The time it takes for a cluster to leave from the tip is determined by the decay time of the autocorrelation curve at the tip of the membrane tube. Fig. 6.2b shows an exponential fit to the autocorrelation curve from the tip region of the tube in fig. 6.1a. The exponential fit gives a decay time for the motors at the tip: $12.6 \pm 0.5s$. The times

differ for different tubes but the motor decay times are linear with the
times of arriving clusters (fig. 6.2c) where $t_{\text{decay}} = (0.85 \pm .04)t_{\text{arrival}}$.
Because the time for motor arrival is linear with the time for motors to
depart, we suggest that the motors are recycled towards the tip in paused
membrane tubes. The recycling only arises in tubes that are no longer
growing. The behavior may be present in growing tubes but so many
motors accumulate at the tip that the fluorescent signal in the tip region
is too high to be able to see the subtle motor dynamics we describe here.
It should also be noted that diffusion alone cannot account for the time
scale of this recycling pattern. Motors can diffuse in the membrane a
distance of $2\mu m$ in less than $1s$.[53]

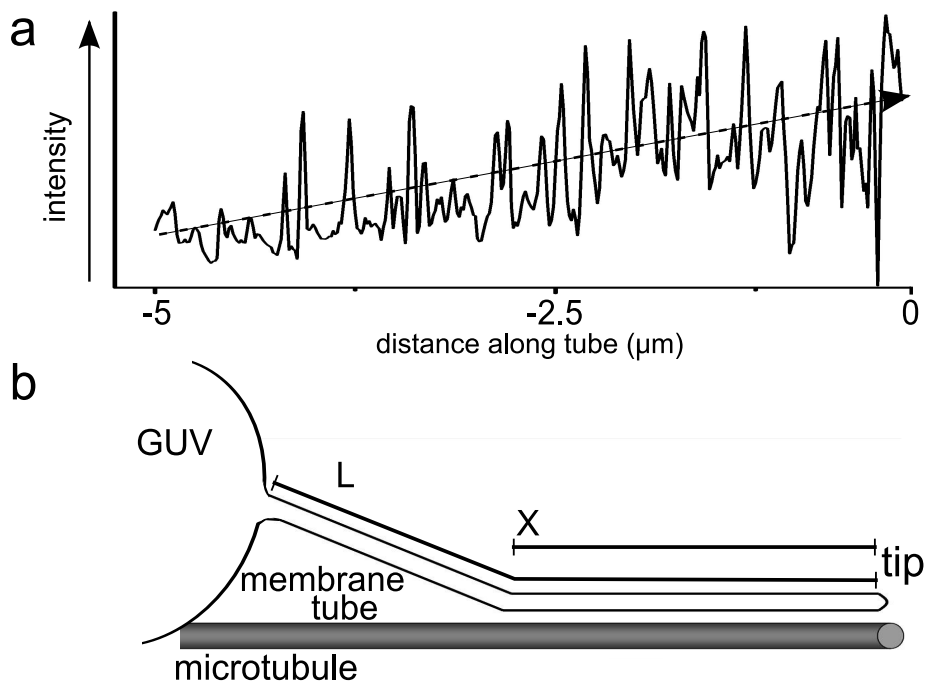Figure 6.3: **Motor cluster dynamics** a) Intensity profile of a cluster of
motors (following the dashed line in fig. 6.1b) moving towards the tip of a
membrane tube: the fluorescence increase indicates that the cluster accumu-
lates motors as it moves towards the tip. b) Cartoon showing the geometry of
a membrane tube of length L extending from a GUV. The tube is anchored
to the MT a distance X behind the tip.

In order to understand how the motors form clusters, we examine the motor density profile as motors move towards the tip. Each time a motor cluster reappears, the motor density starts small and increases as the motors move towards the tip of the membrane tube. The accumulation of motors is indicated by an increase in the fluorescence intensity profile of a building cluster (following the dashed line from fig. 6.1b) shown in fig. 6.3a. Though we cannot identify the exact location where the clusters begin to form, they *always* increase in number as the motors move towards the tip.

We postulate that a nucleation point is defined by the point at which a few motors close to the vesicle randomly anchor the membrane tube to the MT. This occurs at a distance X behind the tip of the tube indicated by the star in fig. 6.1a and shown in the cartoon in fig. 6.3b. This geometry has been observed experimentally[50] and is a shape that minimizes the energy of the GUV/membrane tube system by minimizing the curvature at the point where the tube meets the GUV.[79,94] The location of a nucleation point can also be at the crossing of two underlying MTs, where membrane tubes are often found to bend and diverge, or formed at a point where the MT has a defect.

6.3   Model and Simulations: cooperative binding, unbinding and a nucleation p-oint

The formation of clusters that arrive at regular time intervals can be explained in a physical picture in which motors diffusing in the membrane may randomly bind at a nucleation point a distance X behind the tube (cartoon in fig. 6.3b). Once a few motors have bound to the MT and walk towards the tip, motors diffusing in the membrane tube have a high probability of binding to the MT next to motors already bound to the MT. This cooperative binding could arise from an increased proximity of the membrane tube to the MT lattice when a single motor links the tube to the MT making it easier for another motor nearby to bind. Another possible cause of cooperative binding could be mutual interaction

between motors.[54,95] We further propose that motors at the tip of the
membrane tube unbind cooperatively. As many motors accumulate in
the tip region, individual motors that are unable to step forward will get
frustrated and fall off initiating a cascade of motor detachment.[96]
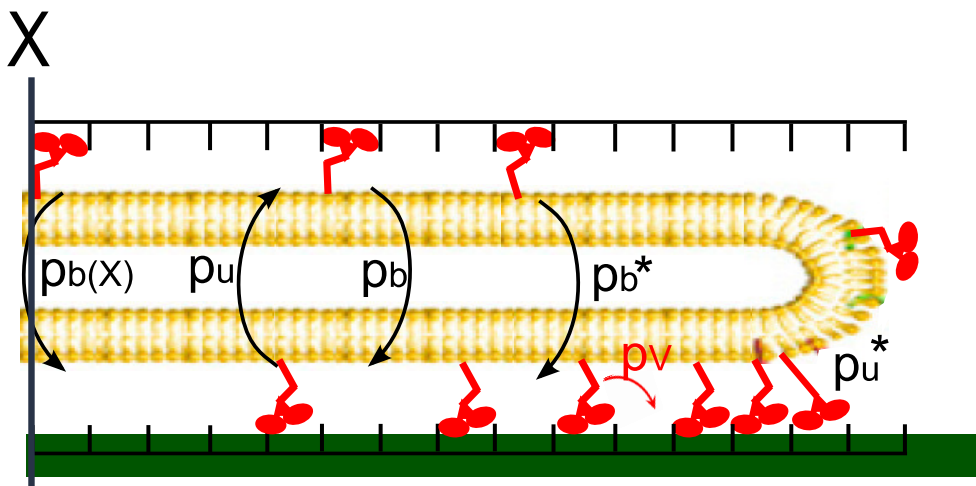
Figure 6.4: **Simulations with motor cooperativity** a) Motors bind randomly anywhere along the MT lattice with a probability p_b and a distance X
behind the tip of the membrane tube with a probability $p_{b(X)}$. However, if a
diffusing motor neighbors a motor that is already bound to the MT lattice, the
diffusing motor will bind next to it on the MT with a probability p_b^*. Once on
the MT lattice, motors may walk towards the tip of the MT with a probability
p_v or detach from the MT with a probability p_u and at the very tip with a
probability p_u^*.

We use Monte Carlo simulations to investigate whether or not a nucleation point, cooperative binding and cooperative unbinding at the tip
account for the trends in our experimental data. We consider a MT
directly beneath a membrane tube with N diffusing motors. The high
curvature of the membrane tube only allows ≈ 3 protofilaments of the
MT to be accessible to the motors in the membrane tube. We consider
the simplest case and simulate the motor dynamics on a single protofilament and in a one-dimensional membrane tube. We consider a single
motor to be a unit, neglecting the existence of different attachment and

detachment rates for both motor domains[97] and all rates apply to the entire motor.

Motors diffusing in the 1-D membrane tube explore a length $l = \sqrt{4Dt}$, where D is the diffusion constant, and t is time. These diffusing motors do not feel eachother and may occupy the same lattice site. Motors in the membrane tube may bind to the MT at a nucleation point a distance X behind the tip of the MT, provided a lattice site is empty. Motors in the membrane may also bind to empty lattice sites on the MT next to already bound motors with a high probability. Once bound to the MT, a motor walks forward as long as the site in front of it is unoccupied.

The cartoon in fig. 6.4 shows the probabilities that govern motor behavior in the membrane tube and on the MT in the simulations. Motors freely diffusing in the membrane tube randomly bind to the MT lattice anywhere with a very small probability p_b, and at the nucleation point a distance X behind the tip with a probability $p_{b(X)}$. If the diffusing motor encounters motors that occupy neighboring lattice sites on the MT, it binds to the MT with a probability p_b^*, where $p_b^* = \gamma p_{b(X)}$. Once motors are bound to the MT, they walk towards the tip at a constant velocity with a probability p_v. Motors unbind from the lattice with a probability p_u. At the tip of the tube, motors are intially less likely to fall off due to crowding effects,[98,99] but as more motors accumulate individual motors will get frustrated and fall off initiating a cascade of motor detachment.[96] Thus, we estimate the probability of unbinding, $p_u^* = \frac{p_u}{100}N$.

The values D, V, p_v, and p_u used in the simulations are taken directly from experimentally measured values. $D = 1.2 \pm 0.2 \mu m^2/s$ for a lipid-motor complex freely diffusing in a membrane tube.[53] The kinesin motor in these experiments walks with a probability $p_v = 1$ at speeds of $450 \pm 50 nm/s$ which is $\approx 53 \pm 7$steps/s (V).[100] Kinesins walk on MTs for an average of 100 steps[13,14] ($p_u = 0.01$). We assume the probability of random binding anywhere along the MT lattice between X and the tip to be very small $p_b = .001$.[86] The small value is chosen since a motor is likely to diffuse in the membrane for a long time before "feeling" the MT below, because the majority of the lipid bilayer of the tube is not close to
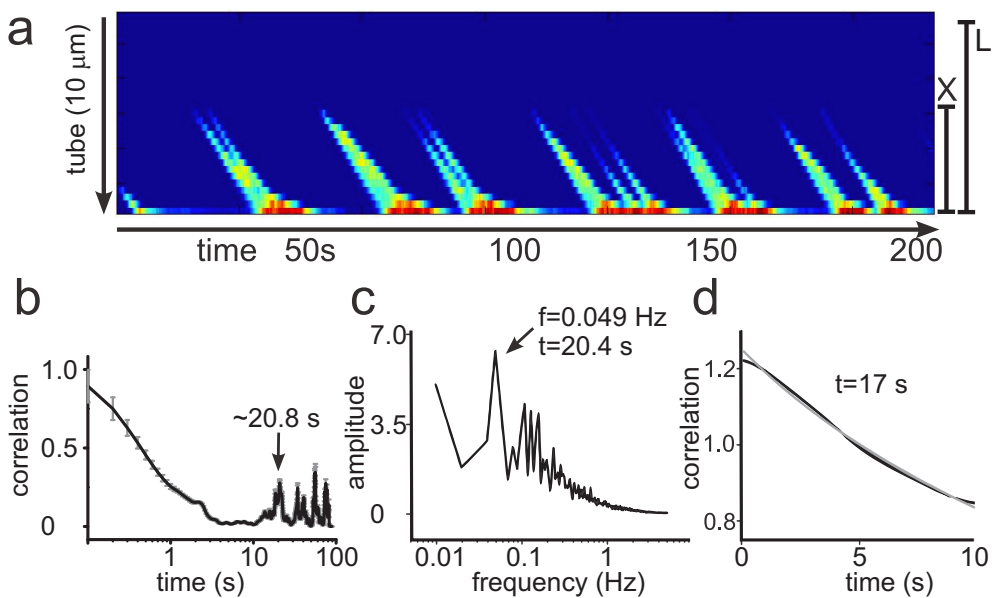
Figure 6.5: **Simulations with cooperative binding and** X a) Kymograph
from a simulation where motors bind cooperatively and there is a nucleation
point along the MT, X. $N = 100$, $L = 10\mu m$ and $X = 5\mu m$. Motor clusters
appear approximately every $20s$. b) Autocorrelation curve of the signal in (a)
showing a distinct peak at $\approx 20.8s$. c) Power spectrum of the signal with
a peak at $20.4s$. d) Autocorrelation curve of the fluorescence signal at the
tip of the membrane tube fit with an exponential decay that gives a cluster
dissipation time of $17s$. The cluster arrival times and decay time at the tip
have similar values.

the MT. At X the probability of binding is larger because the membrane tube is closer to the MT making the MT more accessible to motors in the membrane tube at this point. Thus, the probability of binding chosen here is $p_{b(X)} = .02$. As soon as motors feel clusters of motors on the MT below, they bind with an enhanced probability by a factor $\gamma = 12$. We reason the value of γ by assuming a minimum cluster to be at least 2 motors and considering that there are at least 6 lattice sites around an individual motor on a MT that can be occupied by a neighboring motor. We use the above values for all the simulations.

Because the number of motors in a membrane tube, the length of a membrane tube and the point where the tube is anchored to the MT are different in each experiment, we also vary the values in the simulations to see how the system responds. Based on experimental conditions where vesicles have $\approx 120 motors/\mu m^2$, we estimate the number of motors, N, on a membrane tube to be between 25 and 120. In our simulations, tubes that have fewer than 25 motors, often do not have motors at the tip of the tube implying that too few motors cannot support this tube system. Tubes with greater than 120 motors become very crowded at the tip and the dynamics of motor clusters can no longer be seen. Note that N does not vary in an individual simulation because we assume the density of motors over the vesicle and tubes to be uniform. We consider membrane tubes that range from $5\mu m$ to $10\mu m$ in total length (L). (Simulations of tubes of length $> 10\mu m$ show the same quantitative results as tubes of $10\mu m$). Distances behind the tip (X) range from $2\mu m$ to $7\mu m$.

Fig. 6.5a shows a kymograph from a simulation where $N = 100$, $L = 10\mu m$, and $X = 5\mu m$. The kymograph shows the formation of clusters arriving at the tip in intervals of $\approx 18s$. The autocorrelation (fig. 6.5b) and power spectrum (fig. 6.5c) of the signal confirm a cluster arrival time of $\approx 20s$ and motors decay from the tip over a time of $17s$ (fig. 6.5d). In contrast, in the absence of a nucleation point motor clustering requires a much higher probability of cooperative binding and clusters do not arrive at regular time intervals (fig. 6.6a). In this case $N = 40$ and $L = 10\mu m$. N larger than 40 in simulations without X lead to saturating conditions at the tip, so we show an example with fewer
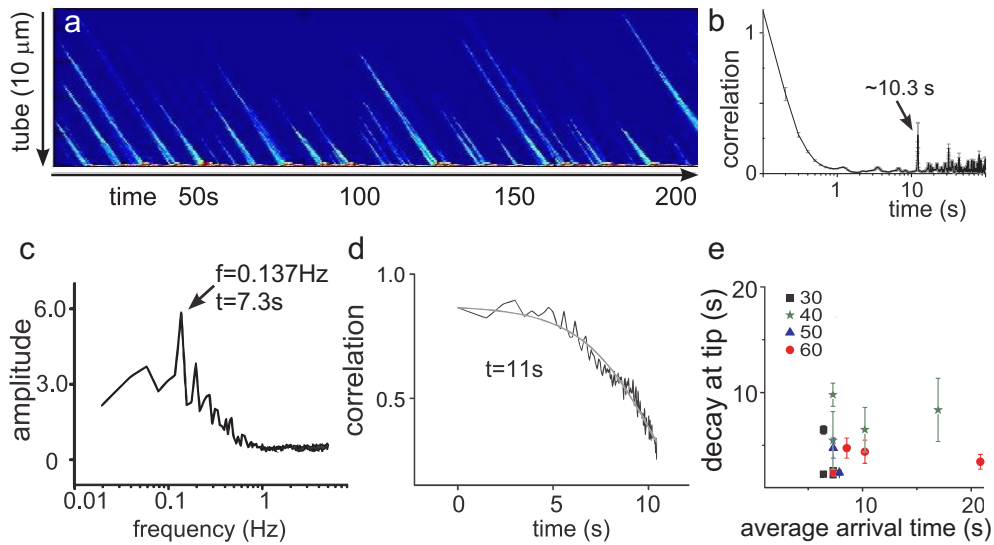
Figure 6.6: **Simulations with cooperative binding but no** X a) Kymograph where motors bind cooperatively to the MT but where there is no defined nucleation point (no X). $N = 40$, $L = 10$, $p_b = 0.001$ and $p_b^* = 0.3$. Motors cluster, but there is less of a defined arrival period as in fig. 6.5a. b) Autocorrelation curve of the signal in (a) showing a less defined peak than in fig. 6.5b of $\approx 12.2s$. c) Power spectrum of the signal with a peak at $7.3s$. d) Autocorrelation curve of the signal at the tip of the tube with an exponential decay that gives a decay time of $11s$. The cluster arrival times and decay time at the tip are of the same order of magnitude though the peaks in the autocorrelation curve are not very large. e) Scatterplot of simulated data for different motor number ($L = 10$ μm) in the absence of a nucleation point, X. The different symbols represent different N. There is no linear increase in cluster arrival time with tip decay time as seen in the experimental data.
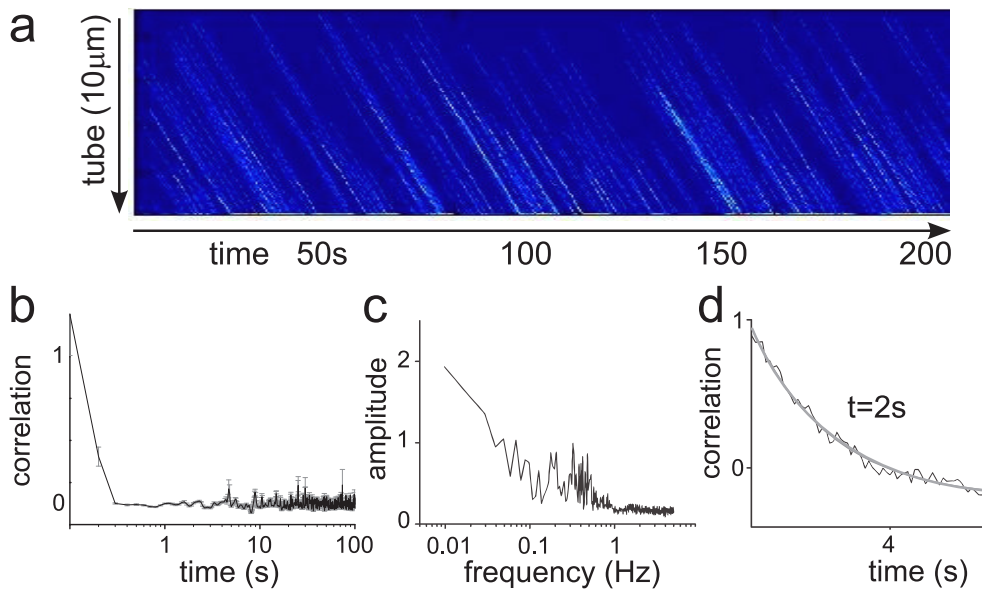
Figure 6.7: **Simulations without cooperative binding or** X a) Kymograph of motors walking along a MT below a membrane tube in the absence of both cooperative binding and X. $N = 40$, $L = 10$, $p_b = 0.001$, $p_b^* = 0$. In the absence of cooperative binding, motors do not cluster. b) The autocorrelation curve of the signal in (a) does not show any peaks in the correlation at longer time lags elucidating the absence of clusters. c) The power spectrum does not peak at any specific frequency as in figs. 6.5c and refsimdat2c. d) The exponential fit to the autocorrelation curve of the signal at the tip of the tube gives a time of $\approx 2s$. Because motors do not build into clusters and accumulate at the tip, the loss of motors at the tip is less significant.

motors here. The probability of cooperative binding is 300 (instead of 12) times greater than p_b because smaller values do not lead to cooperative binding in the absence of X. Here, the highest peak appears to be at $\approx 12.2s$ (fig. 6.6b). The power spectrum suggests an average arrival time of $7.3s$ (fig. 6.6c). The decay time, $11s$, is a similar value to the arrival time (fig. 6.6d). Fig. 6.6e shows the resulting scatterplot of average motor cluster arrival time vs. decay time at the tip for simulated data with different N in the absence of X. There is no linear increase in cluster arrival time with tip decay time as seen in the experimental data. Moreover, if cooperative binding is absent, clusters do not form as can be seen in the kymograph of fig. 6.7a. Peaks in both the autocorrelation curve and the power spectrum are lost, in striking contrast to figs. 6.5b and 6.6b.

We have confirmed that a nucleation point is critical for the recycling phenomenon we observe to occur. We further confirm that all three ingredients: cooperative binding, cooperative unbinding at the tip, and a nucleation point are essential for our model to reproduce the experimental results. Fig. 6.8a shows a kymograph in the absence of cooperative binding, but where both a nucleation point and cooperative unbinding are present. Even at high N clusters do not form in the absence of cooperative binding. Cooperative unbinding is also critical. When we remove cooperative unbinding so that $p_u^* = p_u$, though clustering does occur over regular time intervals, the population of motors at the tip is not enough to continuously hold the membrane tip in place even at N as high as 60, a value in the middle of the expected range on a membrane tube. The arrows in fig. 6.8b indicate points where there are no motors at the tip. If we lower the unbinding probability at the tip to simply account for crowding effects that reduce the unbinding rate, we find that the distinct timescale over which motor clusters form and arrive at the tip disappears as shown in the example in fig. 6.8c.

In the simulations in which we assume a nucleation point to be present at X, we recover the experimentally observed linear relationship between arrival time and decay time for different values of N. Fig. 6.9 shows the resulting average cluster arrival time vs. the average decay time at
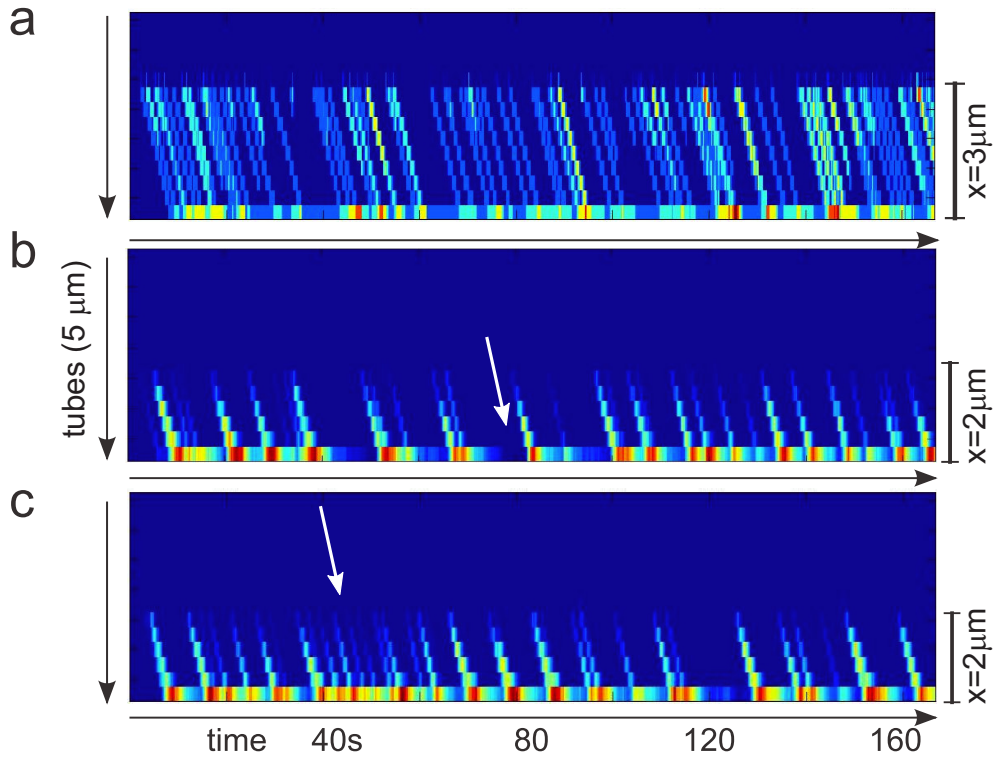
Figure 6.8: **Verification of model components with simulations** a) Simulation of a membrane tube with X and cooperative unbinding at the tip but without cooperative binding along the length of the tube. $N = 100$, $L = 5\mu m$, $X = 3\mu m$ and $p_b^* = 0$. Clusters do not form. b) Simulation of a membrane tube with X and cooperative binding but without cooperative unbinding at the tip. $N = 60$, $L = 5\mu m$, $X = 2\mu m$ and $p_u^* = p_u = .01$. Here, the population of motors at the tip is often not high enough to be able to hold the tip in place. An example of no motors at the tip is indicated by the arrow. c) Simulation as in (b) without cooperative unbinding but with a lower unbinding probability at the tip: $p_u^* = \frac{p_u}{100} = .0001$. Here, the distinct timescale over which motors cluster and arrive at the tip disappears.

the tip from simulations of different membrane tubes with varying X.
The different symbols represent different N and the arrows indicate an
increase in X. The increases in X are indicated in the table at the top
of the fig. 6.9 where the numbers are distances in μm behind the tip. We
find that, at each N, an increase in X results in an increase in both the
average decay time at the tip and the average cluster arrival time.

	N	L (μm)	X (μm)
★	25	5	2➤4
◆	60	5	2➤4
■	100	10	2➤5
●	120	10	4➤7
⟁	experimental data		
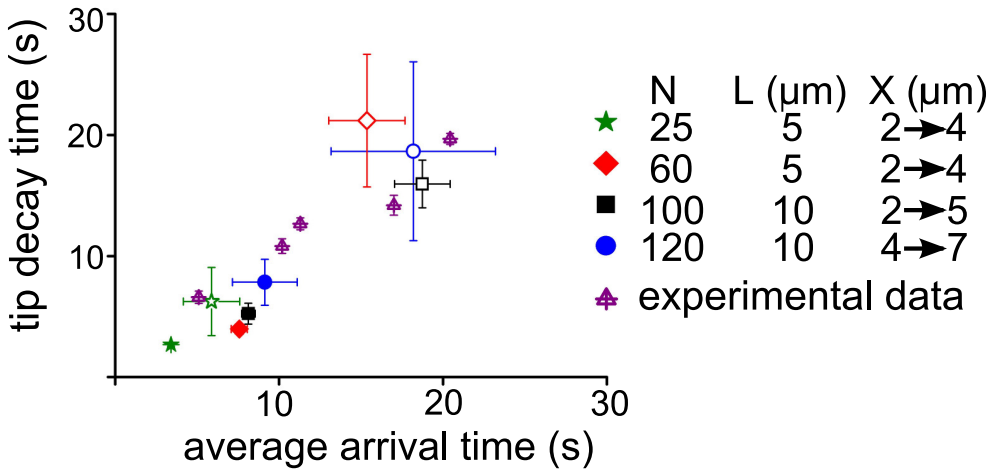
Figure 6.9: **Average arrival time vs. decay time at the tip from
simulations** Scatterplot of simulated data for different motor number (N),
length (L) and X. The different symbols represent different N. For each N,
moving X to a position farther away from the tip (open symbols represent a
larger X) results in a linear increase in timescales. The experimental data,
indicated by the purple triangles, falls into the simulation regime.

The experimental data, indicated by purple triangles in fig. 6.9 fall
into the same regime as the simulations for different N. Because the
simulations that account for cooperative binding, cooperative unbinding
at the tip and a nucleation point reproduce the experimental results,
we suggest that motors in experiments are indeed recycled to make ad-
ditional walking attempts to the membrane tube tip. The simulations
provide an estimate for the cooperative binding probability of 0.24 and
for the number of motors necessary to drive the system: $25 < N < 120$.

6.4   Conclusion

We have shown that motors in stationary membrane tubes spontaneously create a recycling pattern of motor clusters that grow as they move towards the tip of the tube at typical timescales. Using Monte Carlo simulations, we show that cooperative binding can account for the formation of motor clusters. From the simulations we estimate a cooperative binding probability of 0.24 and a range for the concentration of motors necessary to drive the system to be between 25 and 120. We also find that, assuming a fixed point where the membrane tube meets the microtubule to be a nucleation point for motor clusters and cooperative unbinding at the tip of the membrane tube, a linear relationship between the average arrival time and tip decay time emerges.

Chapter 7

Bidirectional transport by competing kinesin and dynein, preliminary results

This chapter details preliminary work to investigate motor competition in small vesicle transport. The mechanism by which motors of opposite directionality coordinate to mediate bidirectional transport is still unclear. Here we present a minimal in vitro method to study the influence of force and motor number on bidirectional transport: a tug-of-war scenario. We find that small unilamellar vesicles (SUVs) transported by kinesins in vitro more unidirectionally, as do SUVs transported by dynein. SUVs coated with both kinesin and dynein move bidirectionally but do not have a large net displacement. We tip the ratio of motors on the SUV to favor kinesin and find that vesicles become more motile and move unidirectionally though there are large fluctuations in the SUV speeds. We support the preliminary experimental results with numerical simulations based on a tug-of-war model. The experiments and simulations were performed by Robert Ietswaart during his bachelor research project. We conclude with suggestions for continued research.

7.1   Models for bidirectional transport

Intracellular cargos, commonly in the form of vesicles, move bidirectionally along MTs.[101,102] The bidirectional movement is driven by motors of opposite polarity: kinesin and dynein. Unfortunately, the mechanism by which the motors coordinate to transport material is unclear and has long been debated. There are three popular models for how opposite polarity motors could work together.[101] The first and simplest model is that of a tug-of-war where the cargo is decorated with both fully functional kinesin and dynein that interact with the MT so that the direction of the cargo transport is determined by the set of motors that exerts the highest force (fig. 7.1a).[103] The second model suggests that only one set of motors is on a cargo at any given time and that for the cargo to change direction, the motors must be exchanged (fig. 7.1b). The third model illustrated in fig. 7.1c suggests that both types of motors are bound to the cargo the entire time but that there is a coordination in binding that allows only one type of motor to engage with the MT at any given time.[101]

Here, we explore the first, and simplest of these three models. In the tug-of-war, changes in direction arise from stochastic variation in the number of active motors in a given direction. The net direction of transport, then, is controlled by determining which set of motors has a higher probability of winning the tug-of-war. Until now, bidirectional transport has been examined *in vivo*[104] or *in vitro* with gliding[36] and bead assays.[40] However, *in vivo* there are many other proteins that can play a role in the dynamics of the motors. On beads or glass surfaces, motors are sterically hindered by their position on the bead so that they are not free to self-organize as they might *in vivo*.

Here, we consider a system where kinesin and dynein are attached to small vesicles made of synthetic lipids so that the motors are free to diffuse in the membrane and that there are no accessory proteins to influence the system. We perform computer simulations based on a tug-of-war model and compare the predictions from this model with *in vitro* experiments. We show that kinesins and dyneins can transport small
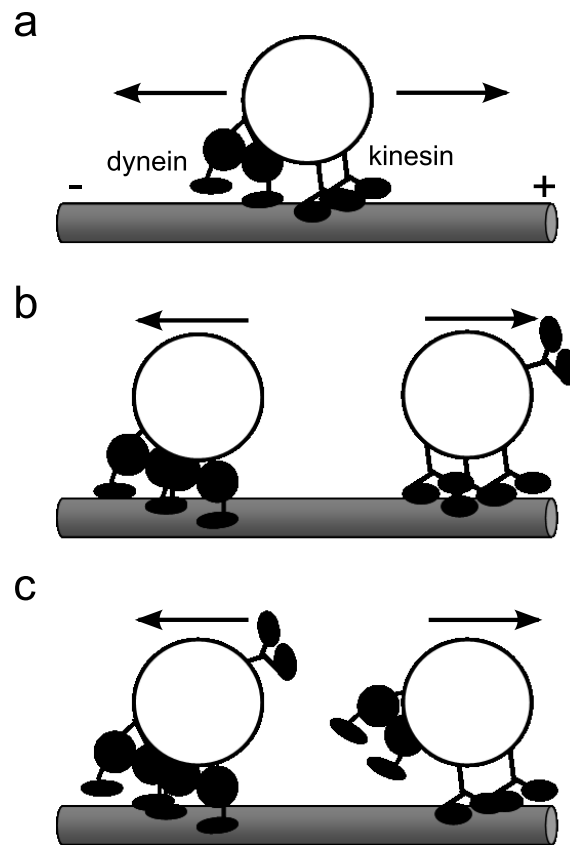
Figure 7.1: **Models for bidirectional transport**. a) Kinesin and dynein both interact with the MT and take steps in opposite directions so that motors compete to transport the SUV in a tug-of-war. b) Only one type of motor is on the cargo at any time. For the cargo to switch direction, the motors on the cargo must be exchanged. c) Both kinesin and dynein are on the cargo, but only one type of motor may interact with the MT at any given time. Here, the motors must coordinate binding on the MT in order to transport in the desired direction. Figure adapted from Gross.[101]

unilamellar vesicles (SUVs) made of synthetic lipids across MTs *in vitro*. We vary the ratio of the two different motor species and examine the resulting dynamics of the small vesicle as it is transported across MTs *in vitro*. We find that as the relative concentration of kinesin on a vesicle increases, the vesicle is biased towards one direction of movement and fluctuations in speed increase. Our initial conclusions from this work are that a force-mediated coordination of motors leads to bidirectional movement. For long range directional movement, the ratio of one motor over the other must increase. We suggest improvements to the model and experiments presented here.

7.2   Tug-of-war

The tug-of-war model can be most simply explained in a picture in which motors diffusing in the membrane of the SUV randomly bind to a MT. Once on the MT, motors walk in their respective preferred directions until the motors reach the edges of the SUV. At the edge, the motors provide counter forces to eachother so that the motors can no longer take steps forward. The motor species of greatest number at the edge of the vesicle has a higher probability to win the tug-of-war and the vesicle moves in the direction of those motors. Stochastic fluctuations in the number of opposing motors bound to the MT at any given time lead to bidirectional movement of the SUV.

We use Monte Carlo simulations, similar to those in chapter 6, to investigate whether or not this fundamentally simple tug-of-war model can lead to bidirectional movement. We consider a MT directly beneath a SUV covered with a number of kinesins, N_k, and dyneins, N_d, so that the total number of motors on the MT, $N = N_k + N_d$. We argue that, due to the high curvature of the small vesicles, motors may only interact with a few protofilaments on the MT.[51] In our simuluations, we consider the simplest case of motors only interacting with a single protofilament, a one-dimensional track. The cartoon schematic in fig. 7.2 shows the system described by motors moving on and exchanging between two lattices, the MT and the SUV.

Motors diffusing in the SUV may attach to any site on the MT, provided it is empty. Once bound to the MT, a motor walks forward in its preferred direction as long as the site in front of it is unoccupied. Motors diffusing in the SUV explore a length $l = \sqrt{4Dt}$ (mean displacement in 1-D), where D is the diffusion constant, and t is time. To account for the large area in which the motors may diffuse in the SUV, motors in the SUV may occupy the same lattice site. However, on the MT, lattice sites are exclusive and only one motor is allowed to occupy a site at any time. Motors freely diffusing in the membrane tube randomly bind to the MT
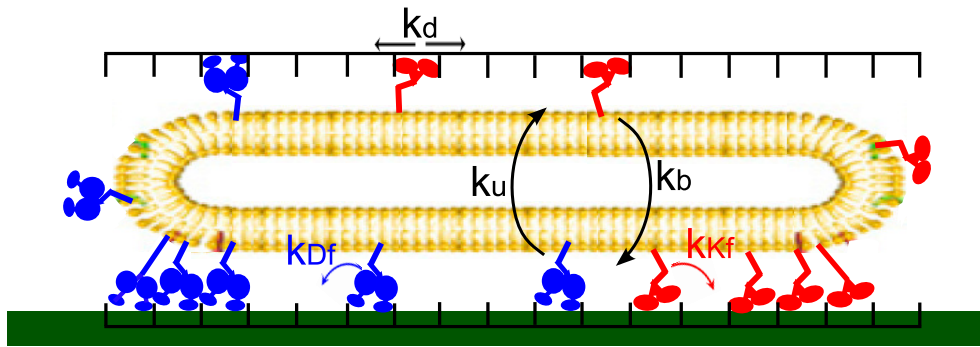
Figure 7.2: **Schematic cartoon of SUV transported by kinesin and dynein** Kinesin motors are shown walking to the plus end and dyneins to the minus end of the MT. The SUV is approximated by a 1-D system where motors can move on and between two lattices at the membrane and on the MT. Kinesins on the MT move towards the plus-end at a rate k_{Kf} and dyneins towards the minus-end at a rate k_{Df}. All motors randomly bind to the MT with a rate k_b and randomly unbind from the lattice at a rate k_u. When one side of the vesicle has more motors, the motors at the opposite end unbind at a rate that is proportional to the ratio of the total numbers at either end.

lattice at a rate k_b. Once motors are bound to the MT, they walk in their respective directions towards the edge of the SUV at constant velocities with a rate k_{Kf} for kinesin and k_{Df} for dynein. Motors detach from the lattice at a rate k_u. Motors at the edge of the SUV may only walk forward if they outnumber the motors walking in the opposite direction at the opposite edge of the SUV and if a motor on the opposite side unbinds

from the MT. The rate at which motors unbind at the edge of the vesicle, in the presence of an opposing force (from motors on the opposite edge) scales with the ratio of opposing motors (e.g. $N_{\mathrm{K(edge)}}/N_{\mathrm{D(edge)}}$) at either end of the SUV. This increased probability of detachment is based on the observations that applied load decreases processivity[13,14] as well as motor velocity.

The values D, k_u, k_{Df} and k_{Kf} used in the simulations are taken directly from experimentally measured values. $D = 1.2 \pm 0.2 \mu m^2/s$ for a lipid-motor complex in a lipid bilayer as measured by Fluorescence Recovery After Photobleaching.[50,53] The kinesin motor in our experiments walks at $450 \pm 50 nm/s$ which gives $k_{Df} = 50 \pm 5s^{-1}$ (Vk). Motors walk on MTs for an average of 100 steps[13,14] $(k_u = 0.1)$. The dynein motor in our experiments walks at $30 \pm 7 nm/s$ which gives $k_{Df} = 5 \pm 2s^{-1}$ (Vd). k_b is assumed to be $0.47s^{-1}$ based on work by others.[86]

Because the ratio of kinesins to dyneins on a SUV are different in each experiment, we also vary the values of N_k and N_d in the simulations to see how the system responds. Based on experiments in the next section we estimate the total number of motors, N, on a SUV to be ≈ 600. Figure 7.3 shows example simulated traces of SUV position in time for SUVs with different ratios of kinesin to dynein. Fig. 7.3a is from a SUV covered with 50% kinesin and 50% dynein and the inset zooms in on the small fluctuations while the motors are involved in a tug-of-war. When the ratio tips towards favoring kinesin (fig. 7.3b, 90% kinesin and 10% dynein) the vesicle is transported at higher speeds in predominantly one direction.

7.3   Comparison of simulations to experimental data

In order to determine if our interpretation of the tug-of-war model presents a reasonable picture of bidirectional transport, we compare the simulations to *in vitro* experiments. We specifically attach kinesin and dynein molecules to fluorescently labeled SUVs ranging from $100nm$ to $2\mu m$ in diameter. SUVs encounter MTs and, in the presence of ATP, the motors
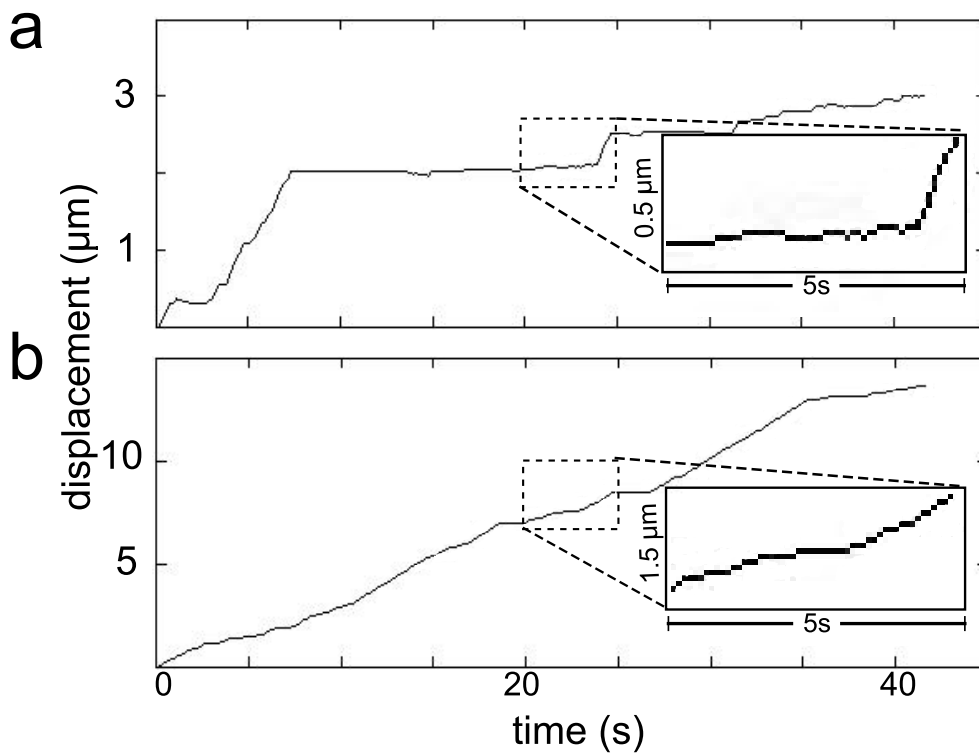
Figure 7.3: **Simulated SUV trajectories** a) Simulated position trace of a SUV covered with 50% kinesin and 50% dynein. Inset zooms in on the region in the dashed box to show the smaller fluctuations of the vesicle where bidirectional transport can be seen. b) Simulated position trace of a SUV covered with 90% kinesin and 10% dynein. There is a stronger bias towards one direction than in (a) and the SUV travels at higher average speeds indicating that kinesin begins to dominate the vesicle transport.

bind to the MT and transport the SUV in the motors' according preferred direction. Fig. 7.4a shows a fluorescence time series of SUV transported by kinesin motors. We trace the trajectory of the SUV and make a kymograph along this trajectory path, shown in fig. 7.4b. The SUV moves steadily and quickly along the MT as compared to the SUV transported by dynein motors in fig. 7.4c. The dynein used in these experiments has a velocity approximately $10x$ slower than kinesin, but there is also a large fraction of the dynein on the vesicles that can bind to MTs but cannot walk. This fraction of dead motors likely contributes to more stationary periods of vesicles transported by dynein such as in the first $10s$ of the kymograph in fig. 7.4c.

However, regardless of the immobile dynein fraction, SUVs coated with only kinesin or only dynein move unidirectionally across MTs. When both kinesin and dynein motors are on the same vesicle, bidirectional transport appears (fig. 7.4d). The example in fig. 7.4d shows a vesicle coated with 90% kinesin and 10% dynein that moves bidirectionally. We do not examine ratios where the amount of dynein on a vesicle outnumbers kinesin. Because vesicles with 100% dynein move so little (again likely due to the large fraction of dead dynein motors that bind to the MT) we do not expect to see an increase in motility by increasing the amount of dynein relative to kinesin. We perform the experiments on the following ratios: 50% kinesin and 50% dynein, 75% kinesin and 25% dynein, 90% kinesin and 10% dynein, 95% kinesin and 5% dynein and finally 99% kinesin and 1% dynein. For all the experiments, we trace the positions of the SUVs in time. From each of these position traces we determine the instantaneous speeds of the SUV using a moving window size of 2s.

Fig. 7.5 shows the distribution of the speeds for the SUVs in fig. 7.4. Kinesin (fig. 7.5a) has an average speed of $354nm/s$ with a standard deviation of $123nm/s$. In contrast, the vesicle moved by dynein motors does not move very quickly and has a mean speed of $8nm/s$ with a smaller spread in the speeds of $13nm/s$. For the mixture of 90% kinesin and 10% dynein the mean is $14nm/s$ and has a spread of $111nm/s$. The non-zero mean speed indicates that one motor dominates this system,
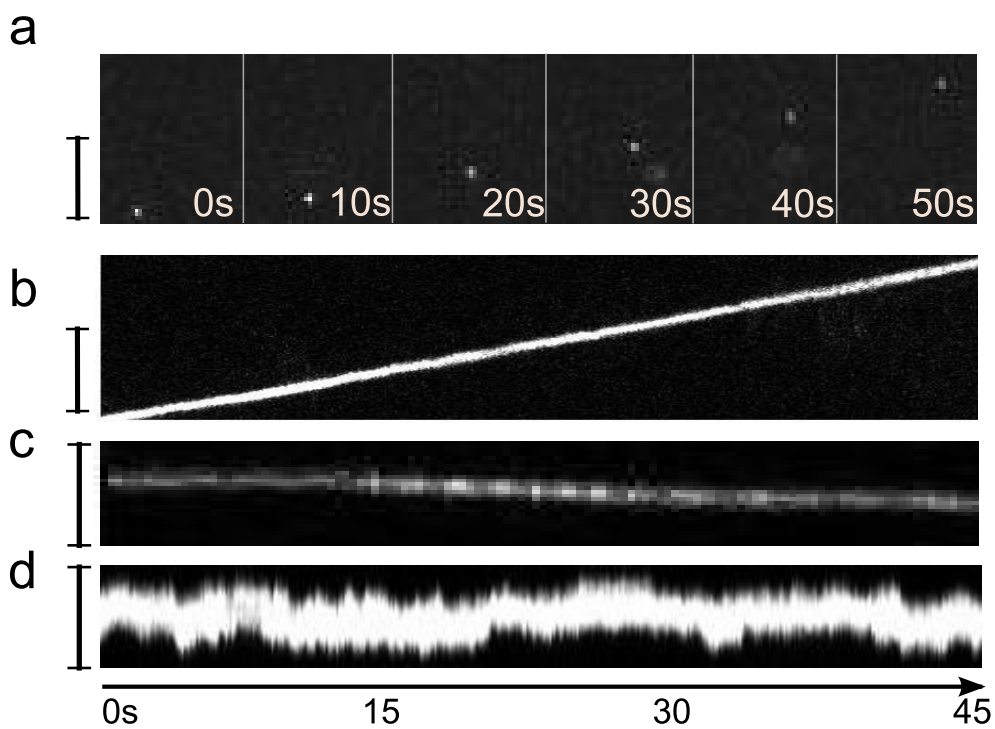
Figure 7.4: **Small vesicle transport** *in vitro* a) Time series of a fluorescently labeled vesicle transported over a MT by kinesin motors. bar= $8\mu m$. b) Kymograph of the vesicle, from (a), displacement over the underlying MT. bar= $8\mu m$. c) SUV transported by dynein on a MT. bar= $2\mu m$. d) SUV coated with 90% kinesin and 10% dynein. bar= $2\mu m$.
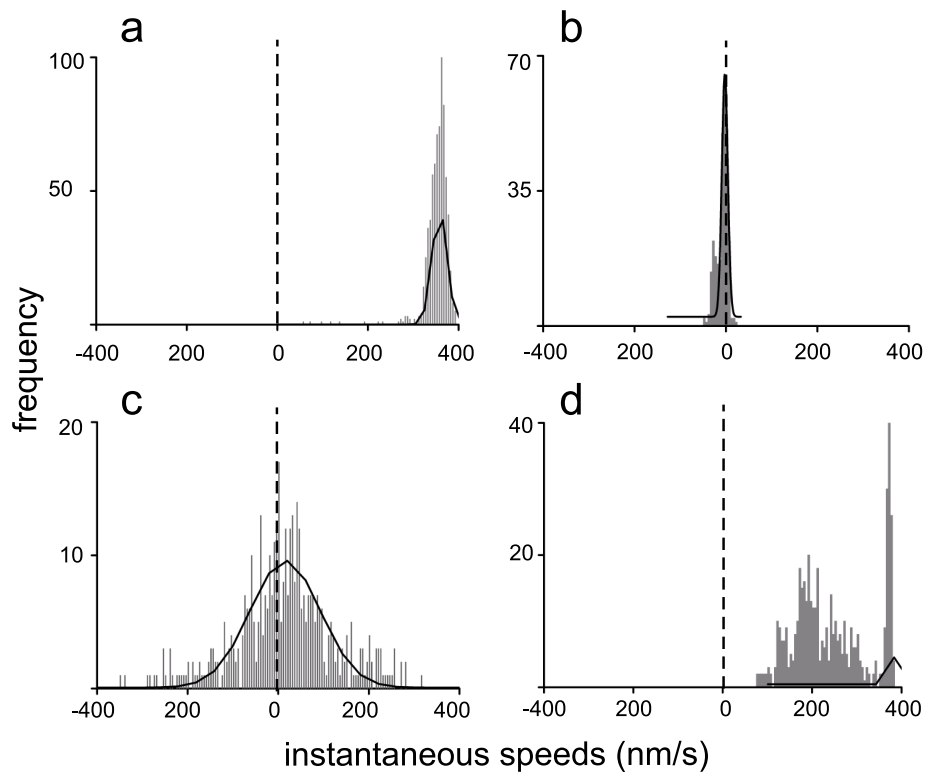
Figure 7.5: **SUV instantaneous speeds** a) Speed distribution from fig. 7.4a with 100% kinesin. b) Speed distribution from fig. 7.4a with 100% dynein. c) Speed distribution from fig. 7.4c with 90% kinesin and 10% dynein. d) Speed distribution from a simulated trace with 90% kinesin and 10% dynein. The distributions are all fit with single peak gaussians. In general these fits are all poor and do not account for additional "speed populations" in the data, most clearly seen in (d).

likely kinesin because there are many more kinesin than dynein motors. The speed distribution for a simulated trace with 90% kinesin and 10% dynein (from fig. 7.3) is shown in fig. 7.5d where the mean is $421nm/s$ and spread $156nm/s$. All of the distributions in fig. 7.5 are also fit with a gaussian. We perform the fitting to determine if the speed distribution can be described by a single gaussian. However, figures 7.5a, b and d all have a distinct second population to the left of the peak fit by the gaussian indicating that the speeds cannot be described by a single distribution.

To compare all data, we determine the mean, and standard deviation for the instantaneous speeds from all experiments and simulations and plot these in figs. 7.6a and c. Solid symbols represent experimental data while open symbols are from simulated data. The symbols correspond for experiments and simulations using the same ratios. All of the average speeds are listed as positive speeds. Because we do not directly determine the direction a SUV is transported along a MT, we plot the absolute values of the average vesicle speeds.

The experimental data shows a general trend towards increasing speed and increasing spread in the speeds as the kinesin to dynein ratio increases. As the ratio favors kinesin, the SUV becomes more motile. The increase in spread in the speed is an indicator of active motor competition where opposing motors interfere with each other's stepping and hence, speed. The simulated data also increases in mean speed as the amount of kinesin on the SUV increases but the standard deviation does not. We expect this difference because we do not account for membrane fluctuations and measurement noise in our simulations. In order to determine the noise level of the system, we measured the fluctuations of vesicles covered with motors, but in the absence of ATP. These vesicles have a mean between $0nm/s$ and $10nm/s$ and a standard deviation between $0nm/s$ and $60nm/s$. Thus, in the lower left hand corner of the scatterplot any signal from active SUV transport is below the noise.

Figs. 7.6b and d shows the means and standard deviations of the speed distributions as determined from a gaussian fit. The mean speed and standard deviation both increase as kinesin concentration on the
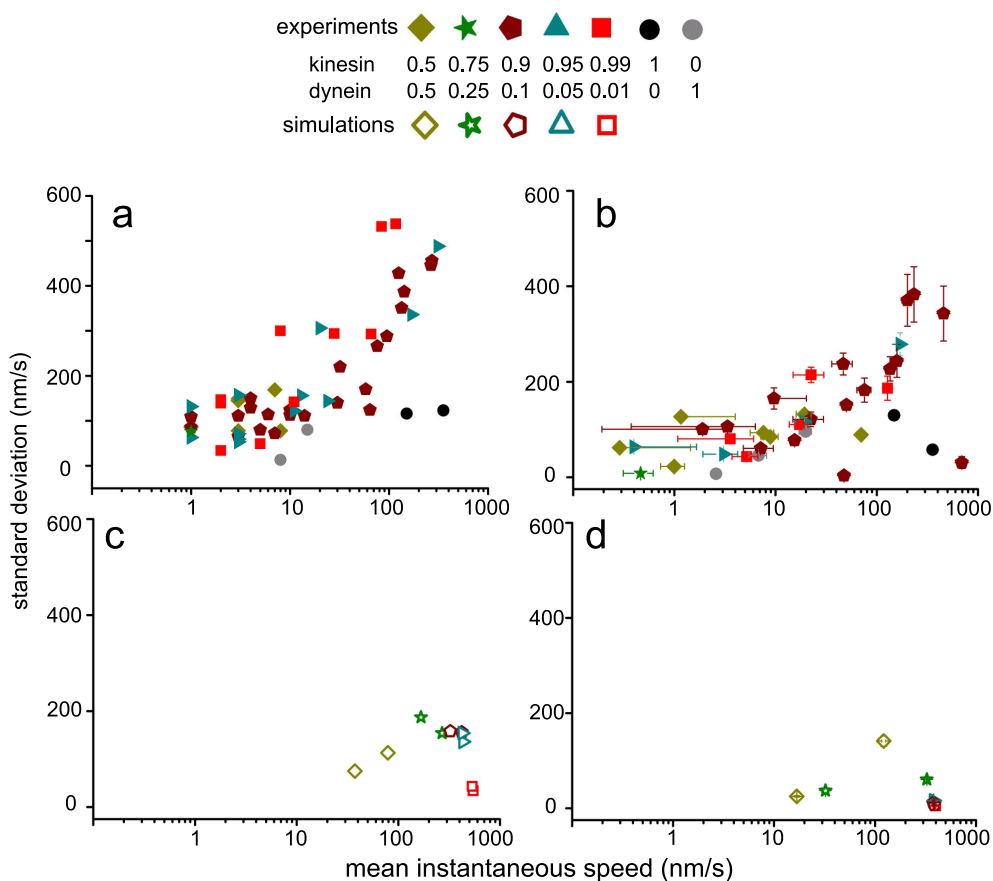
Figure 7.6: **Mean vs. spread in speed for all simulated and experimental data** Solid symbols represent experimental data and open symbols represent simulated data. a) Scatterplot of the mean of the instantaneous speeds versus the standard deviation of the speeds. The scatterplot shows a general trend towards increasing speed and increasing spread in speed as the ratio of kinesin to dynein increases. The legend above shows the ratio of kinesin to dynein. b) Scatterplot of the mean and spread as calculated from a single gaussian fit to the distribution of instantaneous speeds (see gaussian fits to speed distributions in fig. 7.5). The trend in the data of an increase in mean speed and standard deviation with increase in kinesin concentration is also apparent here. The spread in the speeds, indicated by the standard deviation is lower than in (a). c) Scatterplot of mean of the instantaneous speeds versus the standard deviation of the SUV speeds from simulations. d) Scatterplot of the mean and spread as calculated from a single gaussian fit to the distribution of instantaneous speeds from simulations.

SUVs increases. In this case, though, the spread in the speeds is much lower. We expect this because of the poor fitting of the distributions by a gaussian seen in fig. 7.5. The data points that fall into a region of high speed and low standard deviation occur because of the bias in the gaussian fit to the higher, narrower peak. The plot in fig. 7.6a is more representative of the actual SUV transport speeds.

One might expect that SUVs that are more heavily decorated with kinesin should move at high speeds and low spread similar to the case of SUVs covered completely with kinesin (black circles in fig. 7.6a). This trend does not appear in our experimental data. We conclude that dynein, even in small amounts, can still actively interfere with kinesin transport of a SUV.

7.4 Outlook

We have shown that a tug-of-war model for transport with kinesin and dynein does result in bidirectionality. Our model, simulations and experiments confirm that a single motor species will transport an SUV over a MT unidirectionally. When we mix the two types of motors on the SUVs, the SUVs move bidirectionally. We find that as the ratio of kinesin to dynein begins to favor kinesin, the vesicles become more motile, they move at much higher average speeds but there is also a much larger range of speeds. We attribute the spread in speed to opposing dyneins on the SUV interfering with kinesin transport. When motor concentrations are equal, there is very little net movement, comparable to *in vivo* results.[105]

The experiments with SUVs should be repeated using dynein motors that are 100% functional (see chapter/section 2.1.3). These normally functioning dynein motors show MT gliding speeds of $\approx 130 nm/s$ and we would expect them to compete more with kinesin in both the *in vitro* experiments and in the simulations. With a population of fully active dynein available, the motor ratio in the experiments could be tipped to favor dynein and the net transport observed. The experiments could also be improved by using polarity-marked MTs. An indication of polar-

ity would allow us to clearly distinguish which set of motors is winning the tug-of-war at any given point in time. Finally, we suggest that a force-dependent velocity should be incorporated into our model and simulations.

Future experiments: Membrane tubes with dyneins

We have just discussed the dynamics of small vesicles driven by both dynein and kinesin. *In vivo*, however, many other membranous structures are transported bidirectionally by motors, such as membrane tubes. It would be interesting to first characterize membrane tubes formed and transported by dynein motors. Because dynein is processive, one might expect the results to look similar to those of kinesin. However, dynein can take irregular step sizes, side step and take back steps,[16] so that its behavior in membrane tubes under tension is not entirely predictable.

A natural question would be to ask how kinesin and dynein coordinate to mediate membrane tube formation and transport in the absence of any accessory proteins. The dynamics of these membrane tubes may be similar to the dynamics of membrane tubes pulled by nonprocessive motors,[32] though the process driving the dynamics are entirely different. It would be very interesting to compare these two systems and hypothesize why nature chose to use the two motor-species system. Moreover, it would be interesting to see if the dynamics of membrane tubes mediated by both kinesin and dynein show at all similar behavior to small vesicles that are transported by the two competing motors.

7.5   Data Analysis

We determined the position of the SUVs by finding the position of one of the edges of the vesicle in the kymograph. We developed a Matlab® algorithm that examines the signal along each line of the kymograph. Approaching the SUV from the same side for each time point, the algorithm determines where the signal is greater than twice the background signal and defines this point as the edge position. Fig. 7.7a shows the position trace of the vesicle from fig. 7.4d. Similar to the analytical methods used for determining instantaneous speeds of membrane tubes in chapter 4,
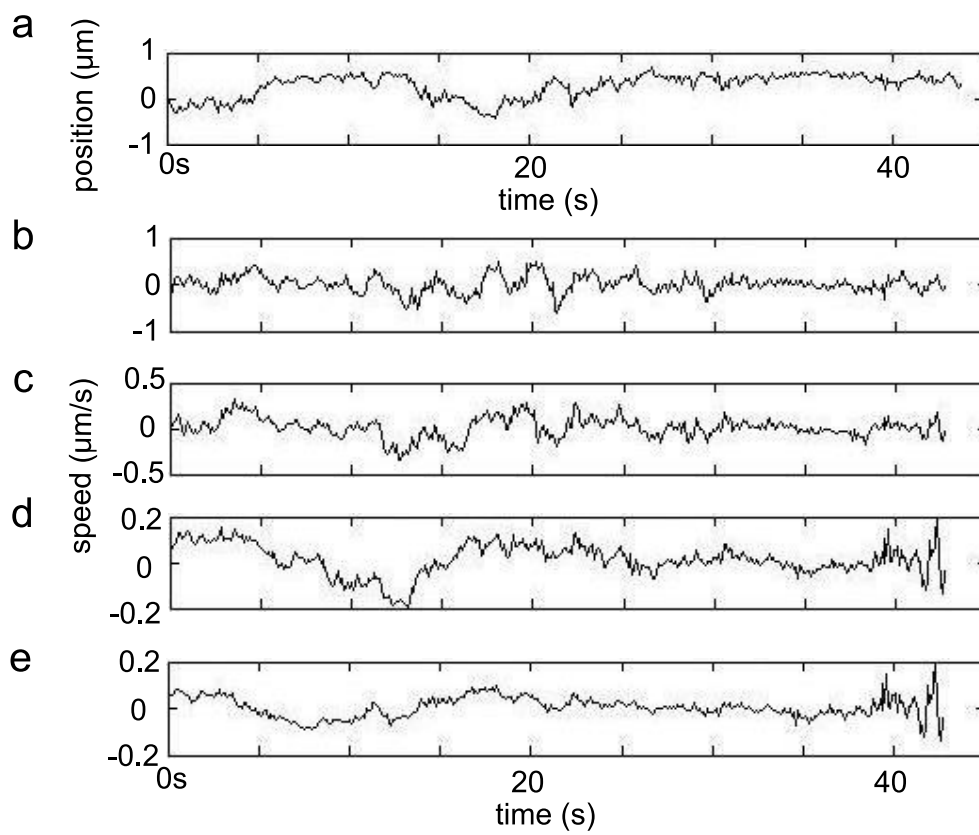
Figure 7.7: **Speed Analysis** a) Trace of the edge of the vesicle from fig. 7.4d. b) Instantaneous speed trace using a window size of $1s$. c) Window size $2s$. d) Window size $5s$. e) Window size $10s$.

we determined instantaneous speeds of the SUV using a moving window. The resulting instantaneous speeds for each point in time for a window size of $1, 2, 5$ and $10s$ are shown in fig. 7.7b-e. A window size of $1s$ is too
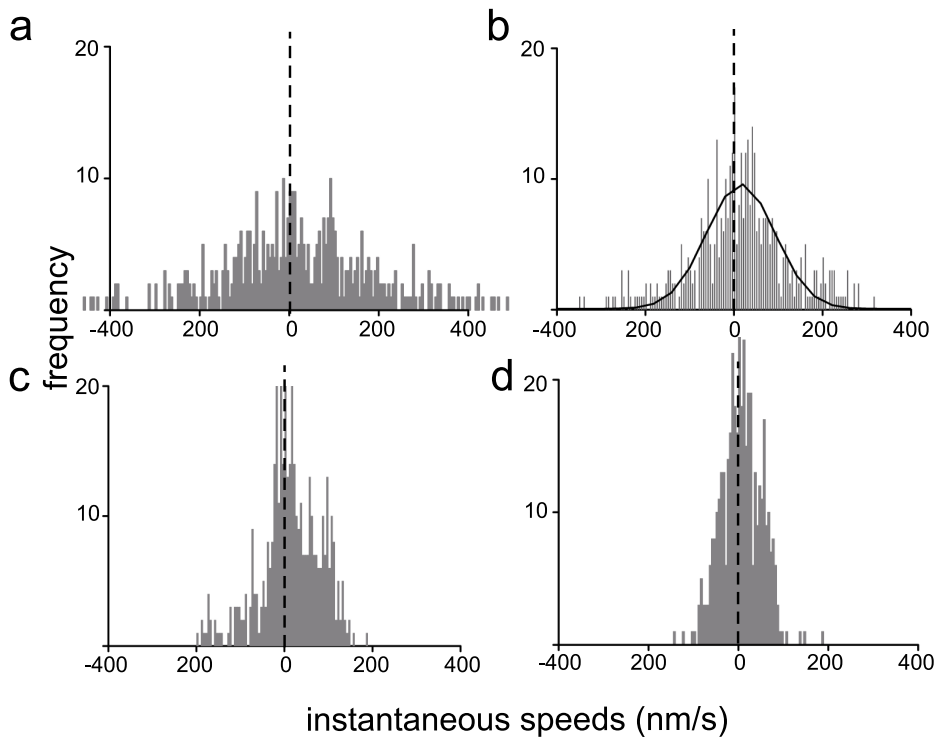
Figure 7.8: **Speed Distributions** a) Distribution of speeds for a window size of $1s$ from the trace in fig. 7.7b. The distribution contains values of speeds that are above the single motor speed. b) Speed distribution for $2s$. The distribution is fit with a single peak gaussian. The mean and spread from this gaussian fit were used to describe the dynamics of each SUV. c) A window size of $5s$ narrows the distribution but, in this example, the peak from (c) is enhanced with the $5s$ window. d) A $10s$ window size overaverages the data and biases in the speeds towards one direction or the other are lost.

small given the noise in the system (data acquisition is 10Hz). The speed values from the distribution exceed the maximum speeds for a single motor (both for dynein and kinesin) as can be seen in fig. 7.8a. Fig. 7.8b shows the speed distribution for a window size of $2s$. Here, the noise

is reduced and a bias towards a positive speed becomes more apparent. A window size of $5s$ narrows the distribution more, but shows the same general features as the $2s$ window. A $10s$ window overaverages the data and the biases in speed towards one direction or the other are lost so that the mean almost always appears to be $0nm/s$. Hence, throughout the analysis, we used a $2s$ window because it was the minimum window size above the noise level and did not average out interesting features in the speed profile. We determine the mean and standard deviation for all the speed data from experiments and simulations. The speed distribution in fig. 7.8b is fit with a gaussian. A single gaussian fit requires that only a single population of speeds exists, which in the case of the SUVs we trace, very infrequently the case.

Bibliography

[1] Amos, L. & Klug, A. (1974) Arrangement of subunits in flagellar microtubules. *J. Cell Sci.* 14:523-549.

[2] Brady, S.T., Pfister, K.K. & Bloom, G.S. (1990) A monoclonal antibody against kinesin inhibits both anterograde and retrograde fast axonal transport in squid axoplasm. *Proc. Natl. Acad. Sci.* USA. 87:1061-1065.

[3] Howard, J. (2001) in *Mechanics of Motor Proteins and the Cytoskeleton* (Sinauer Assoc USA), pp 197-262.

[4] Kull, F.J., Sablin, E.P., Lau, R., Fletterick, R.J. & Vale, R.D. (1996) Crystal structure of the kinesin motor domain reveals a structural similarity to myosin. *Nature* 380:550-555.

[5] Samso, M., Radermacher, M., Frank, J. & Koonce, M.P. (1998) Structural characterization of a dynein motor domain. *J. Mol. Biol.* 276:927-937.

[6] Image timeseries taken from a movie of conventional kinesin walking from the Vale lab: http://valelab.ucsf.edu/Homepage.html.

[7] Chandra, R, & Endow, S.A. (1993) Expression of microtubule motor proteins in bacteria for characterization in in vitro motility assays. *Methods Cell Biol.* 39:115-127.

[8] Reck-Peterson, S.L. & Vale, R.D. (2004) Molecular dissection of the roles of nucleotide binding and hydrolysis in dynein's AAA domains

in Saccharomyces cerevisiae. *Proc. Natl. Acad. Sci.* USA. 101:1491-1495.

[9] Svoboda, K., Schmidt, C.F., Schnapp, B.J. & Block, S.M. (1993) Direct observation of kinesin stepping by optical trapping interferometry. *Nature* 365:721-7.

[10] Kojima, J., Muto, E., Higuchi, H. & Yanagida, T. (1997) Mechanics of single kinesin molecules measured by optical trapping nanometry. *Biophys. J.* 73:2012-2022.

[11] Visscher, K., Schnitzer, M.J. & Block, S.M. (1999) Single kinesin molecules studied with a molecular force clamp. *Nature* 400:184-189.

[12] Kawaguchi, K. & Ishiwata, S. (2000) Temperature dependence of force, velocity, and processivity of single kinesin molecules. *Biochem. Biophys. Res. Commun.* 272:895-899

[13] Thorn, K.S., Ubsersax, J.A. & Vale, R.D. (2000) Engineering the processive run length of the kinesin motor. *J. Cell Biol.* 151:1093-1100.

[14] Schnitzer, M.J., Visscher, K. & Block, S.M. (2000) Force production by single kinesin motors. *Nat. Cell Biol.* 2:718-723.

[15] Coy, D.K., Wagenbach, M. & Howard, J. (1999) Kinesin takes one 8-nm step for each ATP that it hydrolizes. *J. Biol. Chem.* 274:3667-3671.

[16] Reck-Peterson, S.L., Yildiz, A., Carter, A.P., Gennerich, A., Zhang, N. & Vale, R.D. (2006) Single-molecule analysis of dynein processivity and stepping behavior. *Cell* 126:335-348.

[17] McDonald, H.B., Stewart, R.J. & Goldstein, S.B. (1990) The kinesin-like ncd protein of drosophila is a minus end-directed microtubule motor. *Cell* 63:1159-1165.

[18] Walker, R.A., Salmon, E.D. & Endow, S.A. (1990) The *Drosophila claret* segregation protein is a minus-end directed motor molecule. *Lett. Nat.* 347:780-782.

[19] deCastro, M.J., Ho, C-H. & Stewart, R.J. (1999) Motility of dimeric ncd on a metal-chelating surfactant: evidence that ncd is not processive. *Biochemistry* 38:5076-5081.

[20] Foster, K.A. & Gilbert, S.P. (2000) Kinetic studies of dimeric Ncd: evidence that Ncd is not processive. Biochemistry 39:1784-91.

[21] King, S.J. & Schroer, T.A. (2000) Dynactin increases the processivity of the cytoplasmic dynein motor. *Nat Cell Biol.* 2:20-24.

[22] Gennerich, A., Carter, A.P., Reck-Peterson, S.L. & Vale, R.D. (2007) Force-induced bidirectional stepping of cytoplasmic dynein. *Cell* 131:952-965.

[23] deCastro, M.J., Fondecave, R.M., Clarke, L.A., Schmidt, C.F. & Stewart, R.J. (2000) Working strokes by single molecules of the Kinesin-related microtubule motor Ncd. *Nat. Cell Biol.* 2:724-729.

[24] Pechatnikova, E. & Taylor, E.W. (1999) Kinetics processivity and the direction of motion of Ncd. *Biophys. J.* 77:1003-1016.

[25] Gross, SP, Vershinin, M & Shubeita, GT (2007) Cargo transport: two motors are sometimes better than one. *Curr. Biol.* 17:R478-R486.

[26] Leopold, P.L., McDowall, A.W., Pfister, K.K., Bloom, G.S. & Brady, S.T. (1992). Association of kinesin with characterized membrane-bounded organelles. *Cell Motil. Cytoskeleton* 23:19-33.

[27] Vancoillie, G., Lamberg, J., Mulder, A., Koerten, J.K., Mommaas, A.M. Van Oostveld, P. & Naeyaert, J.M. (2000). Cytoplasmic dynein colocalizes with melanosomes in normal human melanocytes. *Br. J. Dermatol.* 1413:298-306.

[28] Vancoillie, G., Lamberg, J., Mulder, A., Koerten, J.K., Mommaas, A.M. Van Oostveld, P. & Naeyaert, J.M. (2000) Kinesin and kinectin can associate with the melanosomal surface and form a link with microtubules in normal human melanocytes. *J. Invest. Dermatol.* 114:421-429.

[29] Habermann, A., Schroer, T.A., Griffiths, G. & Burkhardt, J.K. (2001) Immunolocalization of cytoplasmic dynein and dynactin subunits in cultured macrophages: enrichment on early endocytic organelles. *J. Cell Sci.* 114:229-240.

[30] Klumpp, S. & Lipowsky, R. (2005) Cooperative cargo transport by several molecular motors. *Proc. Natl. Acad. Sci.* USA. 102:1728417289.

[31] Hunt, AJ & Howard J (1993) Kinesin swivels to permit microtubule movement in any direction. *Proc. Natl. Acad. Sci.* USA. 90:11653-11657.

[32] Shaklee, P.M., Idema, T., Storm, C., Schmidt, T & Dogterom, M. (2008) Bidirectional motility of membrane tubes driven by nonprocessive motors. it Proc. Natl. Acad. Sci. USA. 105:7993-7997.

[33] Reck-Peterson, S.L., Tyska, M.J., Novick, P.J. & Mooseker, M.S. (2001) The yeast class V myosins, Myo2p and Myo4p, are nonprocessive actin-based motors. *J. Cell Biol.* 153:1121-6.

[34] Dunn, B.D., Sakamoto, T., Hong, M.S., Sellers, J.R. & Takizawa P.A. (2007) Myo4p is a monomeric myosin with motility uniquely adapted to transport mRNA. *J. Cell Biol.* 178:1193-1206.

[35] Endow, S.E. & Higuchi, H. (2000) A mutant of the motor protein kinesin that moves in both directions on microtubules. *Lett. Nature* 406:913-916.

[36] Vale, R.D., Malik, F. & Brown, D. (1992) Directional instability of microtubule transport in the presence of kinesin and dynein, two opposite polarity motor proteins. *J. Cell Biol.* 119:1589-1596.

[37] Tao, L., Mogilner, A., Civelekoglu-Scholey, G., Wollman, R., Evans, J., Stahlberg, H. & Scholey, J.M. (2006) A homotetrameric kinesin-5, KLP61F, bundles microtubules and antagonizes ncd in motility assay. *Curr. Biol.* 16:2293-2302.

[38] Bieling, P., Telley, I.A., Piehler, J. & Surrey, T. (2008) Processive kinesins require loose mechanical coupling for efficient collective motility. *EMBO Reports* 9:1121-1127.

[39] Beeg, J., Klumpp, S., Dimova, R., Gracià, R.S., Unger, E. & Lipowsky, R. (2008) Transport of beads by several kinesin motors. *Biophys. J.* 94:532-541.

[40] Ross, J.L., Shuman, H., Holzbaur, E.L.F. & Goldman, Y. (2008) Kinesin and dynein-dynactin at intersecting microtubules: motor density affects dynein function. *Biophys. J.* 94:3115-3125.

[41] Ross, J.L., Wallace, K., Shuman, H., Goldman, Y.E. & Holzbaur, E.L.F. (2006) Processive bidirectional motion of dyneindynactin complexes. *in vitro. Nat. Cell Biol.* 8:562-70.

[42] Diehl, M.R., Zhang, K., Lee, H.J. & Tirrell, D.A. (2006) Engineering Cooperativity in Biomotor-Protein Assemblies *Science* 311: 1468-1471.

[43] Rogers, A.R., Driver, J.W., Constantinou, P.E., Jamison, D.K. & Diehl, M.R. (2009) Negative interference dominates collective transport of kinesin motors in the absence of load. *Phys. Chem. Chem. Phys.* Epub April 2009.

[44] Bottier, C., Fattaccioli J., Tarhan, M.C., Yokokawa, R., Morin, F.O., Kim, B., Collard, D. & Fujita, H. (2009) Active transport of oil droplets along oriented microtubules by kinesin molecular motors. *Lab on a Chip* DOI: 10.1039/b822519b.

[45] Roux, A., Cappello, G., Cartaud, J., Prost, J., Goud, B. & Bassereau, P. (2002) A minimal system allowing tubulation with

molecular motors pulling on giant liposomes. *Proc. Natl. Acad. Sci.* USA. 99:5394-5399.

[46] Lane, J.D., Allan, V.J. (1999) Microtubule-based endoplasmic reticulum motility in Xenopus laevis: activation of membrane-associated kinesin during development. *Mol. Biol. Cell* 10:1909-22.

[47] Evans, E. & Yeung, A. (1994) Hidden dynamics in rapid changes of bilayer shape. *Chem. Phys. Lipids* 73:39-56.

[48] Evans, E., Bowman, H., Leung, A., Needham, D. & Tirrel, D. (1996) Biomembrane templates for nanoscale conduits and networks. *Science* 273:933-935.

[49] Koster, G., Van Duijn, M., Hofs, B. & Dogterom, M. (2003) Membrane tube formation from giant vesicles by dynamic association of motor proteins. *Proc. Natl. Acad. Sci.* USA. 100:15583-15588.

[50] Leduc, C., Campàs, O., Zeldovich, K.B., Roux, A., Jolimaitre, P., Bourel-Bonnet, L., Goud, B., Joanny, J-F., Bassereau, P. and Prost, J. (2004) Cooperative extraction of membrane nanotubes by molecular motors. *Proc. Natl. Acad. Sci.* USA. 101:17096-17101.

[51] Campàs O, Kafri Y, Zeldovich KB, Casademunt J, Joanny J-F (2006) Collective dynamics of interacting molecular motors. *Phys. Rev. Lett.* 97:038101.

[52] Brugués, J. & Casademunt, J. (2009) Self-organization and cooperativity of weakly coupled molecular motors under unequal loading. *Phys. Rev. Lett.* 102:118104.

[53] Shaklee, P.M., Bourel-Bonnet, L., Dogterom, M. & Schmidt, T. Nonprocessive motor dynamics at the microtubule membrane tube interface. *accepted Biophys J.*

[54] Roos, W.H., Campàs, O., Montel, F., Woehlke, G., Spatz, J.P., Bassereau, P. & Cappello, G. 2008. Dynamic kinesin-1 clustering on

microtubules due to mutually attractive interactions. *Phys. Biol. 5* epub.

[55] Shaklee, P.M., Idema, T., Bourel-Bonnet, L., Dogterom, M. & Schmidt, T. Kinesin recycling in stationary membrane tubes. *submitted*

[56] Angelova M.I., Soléau S., Meléard P., Faucon J.F. & Bothorel P. (1992) Preparation of giant vesicles by external AC fields. Kinetics and application. *Prog. Colloid Polym. Sci.* 89:127-131.

[57] Pott T., Bouvrais H. & Meleard P. (2008) Giant unilamellar vesicle formation under physiologically relevant conditions. *Chem. Phys. Lipids* 93:115119.

[58] Montes L-R., Alonso, A., Goni, F.M. & Bagatolli L.A. (2007) Giant unilamellar vesicles electroformed from native membranes and organic lipid mixtures under physiological conditions. *Biophys. J.* 93:3548-3554.

[59] Fygenson, D.K., Marcko, J.F. & Libchaber, A. (1997) Mechanics of Microtubule-Based Membrane Extension. *Phys. Rev. Lett.* 79:4497-4500.

[60] Fygenson, D.K., Braun, E. & Libchaber, A. (1994) Phase diagram of microtubules. *Phys. Rev. E* 50:1579-1588.

[61] Harms, G.S., Cognet, L, Lommerse, P.H.M., Blab, G.A. Schmidt, T. (2001) Autofluorescent proteins in single-molecule research: applications to live cell imaging microscopy.*Biophys. J.* 80:2396-2408.

[62] Saunders, L., Perrin, J. & Gammack, D. (1962) Ultrasonic irradiation of some phospholipid solutions. *J. Pharm. Pharmacol.* 14:567-572.

[63] Jolimaitre, P., Roux, A., Blanpain, A., Leduc, C., Bassereau, P., & Bourel-Bonet, L. (2004) Synthesis and preliminary physical ap-

plications of a rhodamin-biotin phosphatidylethanolamine, an easy attainable lipid double probe. *Chem. Phys. Lipids* 133:215-223.

[64] Sköld, H. N., Komma, D. J. & Endow, S. A. (2005). Assembly pathway of the anastral Drosophila meiosis I oocyte spindle. *J. Cell Sci.* 118:1745-1755.

[65] Young E.C., Berliner E., Mahtani H.K., Perez-Ramirez B. & Gelles J. (1995) Subunit interactions in dimeric Kinesin heavy chain derivatives that lack the Kinesin rod. *J. Biol. Chem.* 270:3926-3931.

[66] Kuznetsov, S.A. & Gelfand, V.I. (2001) Kinesin Protocols: Purification of Kinesin from the Brain. *Meth. Mol. Biol.* 164:1-7.

[67] Huang, T.G. & Hackney, D.D. (1994) Drosophila kinesin minimal motor domain expressed in Escherichia coli. Purification and kinetic characterization. *J. Biol. Chem.* 269:16493-16501.

[68] Verbrugge, S., Kapitein, L.C & Peterman, E.J.G. (2007) Kinesin moving through the spotlight: single-motor fluorescence microscopy with submillisecond time resolution. *Biophys. J.* 92:2536-2545.

[69] Petersen, N.O., Höddelius, P.L., Wiseman, P.W., Seger, O. & Magnusson, K.E. (1993) Quantitation of membrane receptor distributions by image correlation spectroscopy: concept and application. *Biophys. J.* 65:1135-1146.

[70] Elson, E. (1985) Fluorescence Correlation Spectroscopy and Photobleaching Recovery. *Ann. Rev. Phys. Chem.* 36:379-406

[71] Axelrod, D., Koppel, D.E., Schlessinger, J., Elson, E. & Webb, W.W. (1976) Mobility measurement by analysis of fluorescence photobleaching recovery kinetics. *Biophys. J.* 16:10551069.

[72] Soumpasis, D.M. (1983) Theoretical Analysis of fluorescence photobleaching recovery experiments. *Biophys. J.* 41:95-97.

[73] Terasaki, M., Chen, L.B. & Fujiwara, K. (1986) Microtubules and the endoplasmic reticulum are highly interdependent structures. *J. Cell Biol.* 103:1557-1568.

[74] Waterman-Storer, C.M. & Salmon, E.D. (1998) *Curr. Biol.* Endoplasmic reticulum membrane tubules are distributed by microtubules in living cells using three distinct mechanisms. **8**, 798-807.

[75] Dabora, S.L. & Sheetz M.F. (1988) The microtubule-dependent formation of a tubulovesicular network with characteristics of the ER from cultured cell extracts. *Cell* 54:27-35.

[76] Vale, R.D. & Hotani, H. (1988) Formation of membrane networks in vitro by Kinesin-driven microtubule movement. *J. Cell Biol.* 107:2233-2241.

[77] Allan, V. & Vale R. (1994) Movement of membrane tubules along microtubules in vitro: evidence for specialised sites of motor attachment. *J. Cell Sci.* 107:1885-1897.

[78] Lane, J.D. & Allan, V.J. (1999) Microtubule-based Endoplasmic Reticulum motility in *Xenopus laevis*: activation of membrane-associated Kinesin during development. *Mol. Biol. Cell* 10:1909-1922.

[79] Derényi, I., Jülicher, F. & Prost, J. (2002) Formation and interaction of membrane tubes. *Phys. Rev. Lett.* 88:238101.

[80] Block, S.M., Asbury, C.L., Shaevitz, J.W. & Lang, M.J. (2003) Probing the Kinesin reaction cycle with a 2D optical force clamp. *Proc. Natl. Acad. Sci.* USA. 100:2351-2356.

[81] Wendt, T.G. *et al.* (2002) Microscopic evidence for a minus-end-directed power stroke in the Kinesin motor Ncd. *EMBO J* 21:5969-5978.

[82] Badoual, M., Jülicher, F. & Prost, J. (2002) Bidirectional cooperative motion of molecular motors. *Proc. Natl. Acad. Sci.* USA. 99:6696-6701.

[83] Allersma, M.W., Gittes, F., deCastro, M.J., Stewart, R.J. & Schmidt, C.F. (1998) Two-dimensional tracking of Ncd motility by back focal plane interferometry. *Biophys. J.* 74:1074-1085.

[84] Meyhöfer, E. & Howard, J. (1995) The force generated by a single kinesin molecule against an elastic load. *Proc. Natl. Acad. Sci.* USA. 92:574-578.

[85] Rossier, O. *et al.* (2003) Giant vesicles under flows: extrusion and retraction of tubes. *Langmuir* 19:575-584.

[86] Campàs, O., Leduc, C., Bassereau, P., Casademunt, J., Joanny, J-F. and Prost, J. 2008. Coordination of Kinesin motors pulling on fluid membranes. *Biophys. J.* 94:5009-5017.

[87] Hackney, D.D. 1995 Highly processive microtubule-stimulated ATP hydrolysis by dimeric kinesin head domains. *Nature* 377:448-450.

[88] Sprague, B.L., Pego, R.L., Stavreva, D.A. and McNally, J.G. 2004. Analysis of Binding Reactions by Fluorescence Recovery after Photobleaching. *Biophys. J.* 86:3473-3495.

[89] Cross, R.A. (2004) The kinetic mechanism of kinesin. *TRENDS Biochem. Sci.* 29:301-309.

[90] Gross, S.P., Welte, M.A., Block, S.M. & Wieschaus, E.F. (2002) Coordination of opposite-polarity microtubule motors. *J. Cell Biol.* 156:715724.

[91] Hill, D. B., Plaza, M. J., Bonin, K. & Holzwarth, G. (2004) Fast vesicle transport in PC12 neurites: velocities and forces. *Eur. Biophys. J.* 33:623632.

[92] Kural, C., Kim, H., Syed, S., Goshima, G., Gelfand, V. I. & Selvin, P. R. (2005) Kinesin and dynein move a peroxisome in vivo: a tug-of-war or coordinated movement? *Science* 305:14691472.

[93] Koster, G., Cacciuto, A., Derényi, I., Frenkel, D., and Dogterom, M. (2005) Force barriers for membrane tube formation. *Phys. Rev. Lett.* 94:068101-4.

[94] Powers, T.R., Huber, G. & Goldstein, R.E. (2002) Fluid-membrane tethers: minimal surfaces and elastic boundary layers. *Phys. Rev. E* 65(4 Pt 1):041901.

[95] Vilfan, A., Frey, E., Schwabl, F., Thormahlen, M., Song Y.H. & Mandelkow, E. (2001) Dynamics and cooperativity of microtubule decoration by the motor protein kinesin. *J. Mol. Biol.* 312:1011-1026.

[96] Frey, E. & Vilfan, A. (2002) Anomalous relaxation kinetics of biological lattice-ligand binding models. *Chem. Phys.* 284:287-310.

[97] Xie, P. (2008) Stepping behavior of two-headed kinesin motors. *Biochim. Biophys. Acta.* 1777:1195-1202.

[98] Crevel, I. M.-T.C., Nyitrai, M., Alonso, M.C., Weiss, S., Geeves, M.A. & Cross, R.A. (2004) What kinesin does at roadblocks: the coordination mechanism for molecular walking. *EMBO J.* 23:2332.

[99] Seitz, A. & Surrey, T. (2006) Processive movement of single kinesins on crowded microtubules visualized using quantum dots. *EMBO J.* 25:267-277.

[100] Svoboda, K., Mitra, P.P. & Block, S.M. (1994) Fluctuation analysis of motor protein movement and single enzyme kinetics. *Proc. Natl. Acad. Sci.* USA. 91:1178211786.

[101] Gross, S.P. (2004) Hither and yon: a review of bi-directional microtubule-based transport. *Phys. Biol..* 1:R1-R11.

[102] Welte, M.A. (2004) Bidirectional Transport along Microtubules. *Curr. Biol.* 14:R525R537.

[103] Müller, M. J. I. , Klumpp, S. & Lipowsky R. Tug-of-war as a co-operative mechanism for bidirectional cargo transport by molecular motors. *Proc. Natl. Acad. Sci.* USA. 105:4609-4614.

[104] Shubeita, G.T., Tran, S.L., Xu, J., Vershinin, M., Cermelli, S., Cotton, S.L., Welte, M.A., & Gross, S.P. (2008) Consequences of Motor Copy Number on the Intracellular Transport of Kinesin-1-Driven Lipid Droplets *Cell*. 135:1098-1107.

[105] Sheetz, M.P. (1999) Motor and cargo interactions. *Eur. J. Biochem.* 262:19-25.

Summary: Membrane transport driven by motor collections

Just like any successful factory, the cell requires a functional and reliable transportation system. Inside the cell, nanometer-sized motor proteins act as the cargo transporters. Motors walk along intracellular highways by putting one foot in front of the other. They use their arms to hold the cargo upon their back. The intracellular highways that motors walk along are protein polymers called microtubules (MTs). These MT tracks radiate out from the center of the cell (where the nucleus sits) towards the edges, in a star shape as shown in fig. 7.9a. The cargo that motors carry can take the shape of spheres of membrane material called vesicles, ranging in size from 10s of nanometers to micrometers, or in long tubular shapes called membrane tubes.

In the same way that cars on a highway are restricted to driving in one direction, motors are too. Some motors are designed to walk towards the nucleus and some motors may only walk away from the nucleus, towards the cell periphery. From studies on individual motors we know how large a motor's steps are, how quickly motors burn fuel (ATP), how much load they can bear and how long they stay attached to and walk on MTs. When transporting cargo in the cell, motor proteins rarely work alone, raising the question of how motors work together in transport.

If you and I need to move a couch down the street into your new apartment, we have to coordinate. First, we have to agree on a direction in which to walk, then we have to walk at a speed that is easy for both of us. Moreover, we need to avoid any obstacles that might appear on the
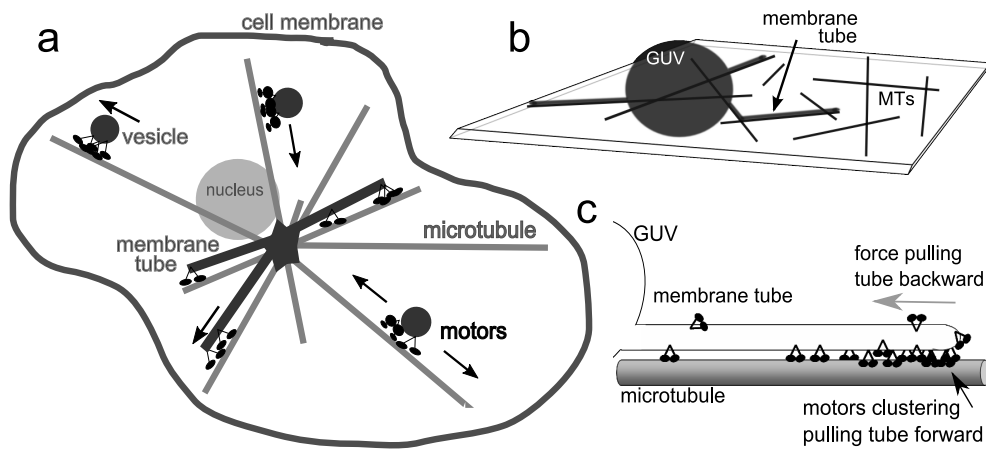
Figure 7.9: **Schematic cartoon of transport in the cell** a) Motor proteins transport cargo, in the form of small pieces of membrane (vesicle spheres and tubular shaped membrane compartments) around the cell by walking along intracellular highways: microtubules. b) Experimental design in this thesis: minimal transportation system from the cell. Motor proteins are bound to a micrometer-sized vesicles called GUVs. When they encounter MT tracks on a glass surface, they walk and exert enough force to deform the GUV and extract membrane tubes. c) Motors clustering at the tip of a membrane tube pull a membrane tube from a GUV while walking on a MT.

sidewalk and make detours when necessary. Then, of course, if your new neighbor decides to lend a hand, he will also have to coordinate with us and not suddenly try to carry the couch off in another direction. The same degree of coordination is necessary for motors to move their cargo across the cell, except that they don't have the luxury of being able to discuss the plan out loud. Multiple motors have to arrange themselves in such a way that they can successfully transport their cargo from point A to point B while avoiding obstacles and making split decisions about which route to take.

In this thesis, we examine how motors coordinate with each other to mediate membrane transport in the cell. Because the cell is highly complex and there are many processes occurring at the same time, we isolate the transportation system and look at it outside of the cell, *in vitro*. In the methods chapter 2, we explain our experimental design. We lay down MT tracks on a glass surface, attach motor proteins to spheres of membrane material that are 1000 times larger than a single motor (these cargos are called giant vesicles, GUVs), provide the ATP fuel for the motors and allow the motors to walk on the MT tracks to carry their cargo. A MT is like a 3-lane highway so that several motors can walk directly next to eachother. As several motors start to walk in parallel along the MT tracks pulling membrane from the massive GUV with them, they exert enough force to deform the spherical shape and extract a long tube of membrane material from the GUV. The experimental design is shown in the cartoon schematic of fig. 7.9b. In order to keep the membrane tube from relaxing back into the spherical GUV, there has to be a constant supply of motors pulling at the tip of the tube, fig. 7.9c.

There are different types of motors inside of the cell, processive and nonprocessive motors. Processive motors take many steps forward along a MT before stepping off the MT and resting while attached to the cargo as other motors carry on with transport. Nonprocessive motors, on the other hand, only take a single step before falling off the MT. Because nonprocessive motors only take a single step along a MT, they initially seem lazy and would not appear to be the best choice for the cell to use as a transporter. Yet, in chapter 4 we show that, paradoxically, though

nonprocessive motors are restricted to walking in one direction, they can actually regulate bidirectional movement of membrane tubes. We suggest a model to understand this paradox. We suggest that nonprocessive motors are social molecules and form small groups, called clusters, all along the length of the membrane tube where the cluster at the tip is responsible for pulling the tube forward. When all the motors in the tip cluster have taken a step and fall off the MT, there is nothing at the tip to keep the tube from relaxing back towards the GUV, so the tube retracts backwards until it encounters another cluster that can either hold the tube in place or pull it forward again. Thus, clusters of unidirectional, nonprocessive motors can regulate bidirectional transport of membrane tubes.

In chapter 4, we infer the motor dynamics simply by observing the dynamics of the membrane tube cargo that the motors transport. However, to truly understand how motors organize to coordinate transport, we must see the motors themselves. In chapter 5, we perform experiments where we directly examine a fluorescence signal from motors in membrane tubes formed from GUVs. We use two widely used biophysical techniques, image correlation spectroscopy and fluorescence recovery after photobleaching to determine the mobility of both processive and nonprocessive motors in membrane tubes. We find that nonprocessive motors show a diffusive behavior at the interface between the underlying MT track and the membrane tube cargo. The diffusion constant of the motors at this interface is at least 1000 times smaller than the diffusion constant for a motor that is freely diffusing in the membrane (not interacting with a MT). We interpret the small diffusion constant as an indicator that nonprocessive motors dynamically bind and unbind to the MT in order to maintain a continuous interaction between the membrane tube and the MT. A continuous, but constantly changing connection between the MT and membrane is probably necessary to drive the bidirectional tube movement we discuss in chapter 4.

Membrane tubes are not only moved bidirectionally by motor proteins but the tubes often pause and change course as the motors beneath decide which MT path to follow. In chapter 6 we find, in non-moving

membrane tubes, processive motor clusters form and reach the tip of a membrane tube at regular time intervals. The result is particularly surprising, because we would not expect motors to continue to be active in membrane tubes that are non-moving. The average times over which motor clusters form scales linearly with the time over which motors depart from the tip of the tube suggesting that motors are recycled towards the tip. We propose that cooperative binding, a strong preference for a motor freely diffusing in the membrane tube to bind directly next to a motor that is already bound to the MT, plays a critical role in recycling. We use computer simulations to show that the presence of cooperative binding between motors (to the MT) quantitatively accounts for the clustering we observe experimentally. The combination of a nucleation point where the cluster begins to grow at a distance behind the tip, a social preference to bind cooperatively along the length of the MT and finally cooperative unbinding at the tip defines the recycling period. We further estimate a probability that motors will bind cooperatively to the MT and also estimate the number of motors necessary for the recycling to occur.

Fig. 7.9a shows a small vesicle that is being pulled in opposite directions by two different motors. In chapter 4, we show that bidirectional transport of membrane tubes can be regulated by unidirectional nonprocessive motors. However, bidirectional transport in cells is thought to be regulated by two different motors that pull their cargo in opposite directions along MTs. How motors of opposite directionality coordinate to mediate bidirectional transport is still unclear. In chapter 7, we study the influence of force and motor number on bidirectional transport of small vesicles. We find that motors of opposite directionality can coordinate through a force-driven tug-of-war, where the side with the most motors wins, to mediate bidirectional transport.

Intracellular transportation in the cell relies on the successful coordination of motor proteins. In this thesis we have shown the transport dynamics that emerge as motors work collectively in transport. We find that motors coupled to eachother through a membrane cargo are sensitive to force and to their neighboring motors, and that both of these factors influence cargo transport. Understanding intracellular transport on such

a simplified level *in vitro* is an essential first step to understanding the underpinnings of a very complex cell from the "bottom up".

Samenvatting

Een cel heeft net zoals elke willekeurige fabriek een betrouwbaar transport systeem nodig. Binnen in de cel zorgen motoreiwitten, van enkele nanometer groot, voor het vervoer van lading. Deze motoren lopen over intracellulaire snelwegen, op een manier die vergelijkbaar is met die van onszelf: ze lopen voetje voor voetje. Hun handen gebruiken ze om lading op hun rug vast te houden. De intracellulaire snelwegen waarover motoren lopen zijn eiwit polymeren, zogenaamde microtubuli (MTs). Deze MT wegen lopen van het midden van de cel (waar de celkern is), naar de rand van de cel. Dit resulteert in een stervormige organisatie van MTs, zoals we in fig. 7.10a kunnen zien. De lading die motoren meedragen kan de vorm aannemen van membraan bolletjes, die we blaasjes noemen, of membraanbuizen. Deze zijn tientalen nanometer tot enkele micrometers groot.

Net zoals auto's op een snelweg maar een richting op mogen rijden, zo mogen motoren ook maar een kant op lopen over een MT. Sommige motoren zijn zo ontworpen dat ze naar de celkern toelopen, terwijl andere motoren juist van de kern weglopen in de richting van de rand van de cel. Van eerdere studies aan individuële motoren weten we hoe groot de stappen zijn die een motor neemt, hoe snel een motor brandstof (ATP) gebruikt, hoeveel lading een motor kan dragen en tenslotte hoe lang een motor over een MT loopt. Motoren, die lading vervoeren door de cel, zijn echter zelden alleen. Daarom rijst de vraag hoe motoren eigenlijk samenwerken.

Als jij en ik een bank vanaf de straat je nieuwe appartement in willen dragen zullen we onze bewegingen goed moeten coördineren. Eerst moeten we het eens worden in welke richting we lopen en vervolgens moeten we een snelheid kiezen die voor ons allebei gemakkelijk is. Boven-
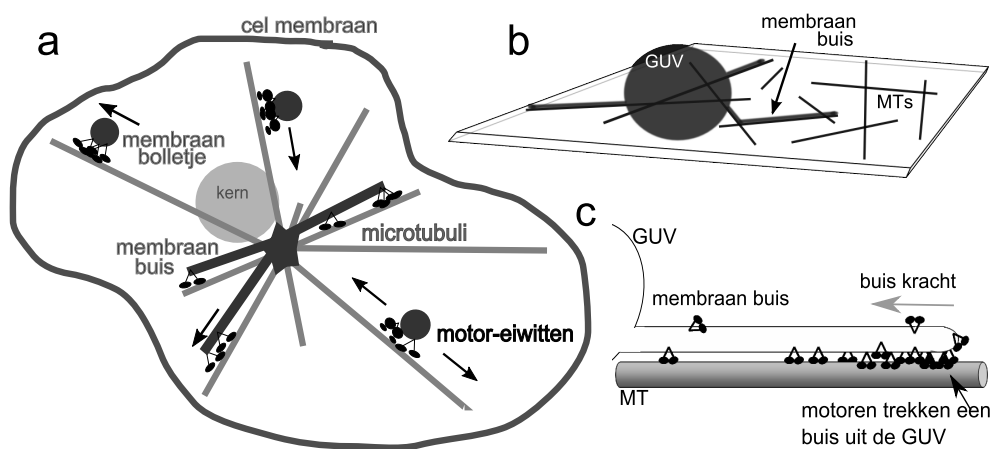
Figure 7.10: **Schematische tekening van transport in de cel** a) Motor-eiwitten transporteren lading, in de vorm van kleine stukjes membraan (zowel kleine bolletjes als buizen) door de cel, door langs intracelulaire snelwegen te lopen: microtubuli. b) De experimentele opstelling die beschreven staat in dit proefschrift. Deze opstelling is een minimaal transport systeem voor de cel. Motoreiwitten worden aan micrometer-grote blaasjes, zogenaamde GUVs, bevestigd. Zo gauw de motoren een MT weg op het glas vinden, lopen ze daarover heen en terwijl ze dit doen, oefenen ze krachten uit die groot genoeg zijn om de GUV te vervormen en buizen te trekken. c) Motoren, die aan het eind van de membraan buis clusteren, trekken een steeds langere buis uit een GUV, terwijl ze over een MT lopen.

dien moeten we obstakels vermijden, en misschien zelfs wat omwegen maken. En, als je buurman ook een handje komt helpen, moet hij natuurlijk ook met ons samenwerken en niet opeens gaan proberen de bank een andere kant op te dragen. Dezelfde mate van coördinatie is nodig als motoren hun lading door de cel willen vervoeren, behalve dan dat ze niet de luxe hebben om luidkeels te overleggen. Meerdere motoren moeten zich zo organiseren dat ze hun lading succesvol van A naar B kunnen vervoeren en ondertussen obstakels vermijden. Daarnaast moeten ze ook beslissen welke kant ze opgaan als ze voor een splitsing komen te staan.

In dit proefschrift onderzoeken we hoe motoren zich organiseren om membraan te transporteren door de cel. Omdat de cel erg complex is en er veel processen parallel plaatsvinden hebben we het transport systeem geisoleerd van de rest van de cel, om het zo *in vitro* te bestuderen. In hoofdstuk 2 beschrijven we de methodes en de experimentele opstellingen die we gebruikt hebben. We plaatsen MT wegen op een glas oppervlak, bevestigen motor-eiwitten aan membraan bolletjes die 1000 keer groter zijn dan de individuële motor-eiwitten (deze bolletjes worden giant vesicles genoemd, GUVs), verschaffen brandstof aan de motoren in de vorm van ATP en ten slotte laten we de motoren over de MT wegen lopen, terwijl ze hun lading meedragen. Een MT is een beetje als een vierbaansweg en dus kunnen meerdere motoren tegelijk naast elkaar over de MT lopen. Terwijl meerder motoren tegelijk in parallel over de MT lopen kunnen ze de reusachtige GUV vervormen en genoeg kracht genereren om lange membraan buizen uit de GUV te trekken. Deze experimentele opstelling is getekend in fig. 7.10b. Om ervoor te zorgen dat de membraan niet als een elastiek terugspringt in de GUV, moet er een constante kracht uitgeoefend worden aan het eind van de membraanbuis en hiervoor is een constante toevoer van motoreiwitten naar het eind van de buis nodig, fig. 7.10c.

In de cel zijn verschillende type motoren aanwezig, processieve en niet-processieve motoren. Processieve motoren zetten meedere stappen over een MT voordat ze van de MT afstappen en rusten terwijl ze aan de lading bevestigd blijven, terwijl die tegelijkertijd door andere motoren verder wordt vervoerd. Niet-processieve motoren aan de andere kant,

zetten echter maar één stap op de MT. Ze lijken dus lui en niet erg geschikt om door de cel als transporteur gebruikt te worden. Toch laten we in hoofdstuk 4 zien dat, ook al lopen niet-processieve motoren maar in een richting over de MT, ze, paradoxaal genoeg, bewegingen van de membraan buis in beide richtingen kunnen reguleren. We stellen een model voor om deze paradox te begrijpen. We stellen voor dat niet-processieve motoren sociale moleculen zijn die kleine groepjes, clusters genoemd, langs de hele lengte van de membraan buis vormen. Het cluster aan het einde van de membraan buis is verantwoordelijk voor het vooruit trekken van de buis. Op een gegeven moment hebben echter alle motoren aan het einde van de buis een stap genomen en de MT los gelaten. Nu weerhoudt niets de buis er meer van om zich terug te trekken richting de GUV. Terwijl de buis zich terugtrekt komt het eind van de buis echter motor clusters tegen, die de buis tegenhouden of zelfs weer vooruit trekken. We kunnen dus concluderen dat clusters van éénrichtings-motoren transport van membraan buizen in twee richtingen kunnen reguleren.

In hoofdstuk 4 deduceren we de dynamiek van de motoren door simpelweg de dynamiek van de membraanbuis, die door de motoren vervoerd wordt, te observeren. Om echter werkelijk te begrijpen hoe motoren zich organiseren om transport te coördineren, moeten we de motoren zelf bekijken. In hoofdstuk 5 voeren we experimenten uit, waar we een fluorescent signaal bestuderen. Dit signaal is direct afkomstig van de motoren aan de membraanbuizen, welke uit de GUVs zijn getrokken. We gebruiken twee veel-gebruikte biofysische technieken, *image correlation spectroscopy* en *fluorescence recovery after photobleaching*, om de mobiliteit van zowel processieve als niet-processieve motoren in membraanbuizen te bepalen. We vinden dat niet-processieve motoren diffunderen op het raakvlak tussen de membraanbuis en de onderligende MT weg. De diffusie constante op dit raakvlak is tenminste 10 keer langzamer dan in de rest van de mebraanbuis, waar de motor geen interactie heeft met de MT weg. Onze interpretatie is dat deze lage diffusie constante een indicatie is van het dynamisch binden en loslaten van de MT. Dit zorgt ervoor dat er continu interactie is tussen de MT en de membraanbuis. Deze continue maar voortdurend veranderende interactie tussen de MT

en de membraanbuis is waarschijnlijk nodig voor de beweging in twee
richtigen van de buis, zoals we die in hoofdstuk 4 hebben besproken.

Membraanbuizen worden niet alleen door motoren in twee richtingen
vervoerd, soms staan de buizen stil en veranderen ze van richting als de
motoren onder de buis besluiten welk MT pad ze gaan volgen. In hoofd-
stuk 6 vinden we, in niet bewegende membraan buizen, dat processieve
motoren ook clusters vormen, die met regelmatige tijdsintervallen bij het
eind van de membraan buis aankomen. Deze observatie is nogal ver-
rassend aangezien we niet hadden verwacht dat motoren actief blijven in
membraan buizen die niet meer bewegen. De gemiddelde tijd waarover
membraan clusters vormen schaalt linear met de tijd waarover motoren
het eind verlaten, wat suggereert dat de motoren aan het eind van de
buis gerecycled worden. Wij stellen voor dat coöperatieve binding een
kritieke rol speelt bij het recyclen. Met coöperatieve binding bedoelen we
dat een diffunderende motor een sterke voorkeur heeft om direct naast
een motor, die al aan de MT gebonden is, aan de MT te binden. We
gebruiken computer simulaties om te laten zien dat coöperatieve binding
van motoren aan MTs de experimenteel-gemeten clustering, kwantitatief
kan verklaren. De combinatie van een nucleatie punt, die de groei van
een cluster opstart en een zeker afstand verwijderd is van het eind van
de buis, coöporative binding langs de lengte van de MT en ten slotte
coöperative loslating aan het eind van de buis defineren de tijdsduur van
de recycle periode. Verder maken we een afschatting van de kans dat mo-
toren coöperatief aan de MT binden en schatten we het minimaal aantal
motoren af dat nodig is voor het recyclen.

Fig. 7.10a toont een klein membraan bollletje dat door twee verschil-
lende motoren in tegenovergestelde richtingen wordt getrokken. In hoofs-
tuk 4 hebben we laten zien dat het transport van mebraanbuizen in twee
richtingen gereguleerd kan worden door niet-processieve motoren. We
denken echter dat in cellen transport in twee richtingen wordt gereg-
uleerd door twee verschillende motoren, die de lading in twee tegen-
overgestelde richtingen trekken langs de MT. Hoe motoren, die in ver-
schillende richtingen lopen, zich coördineren is nog niet duidelijk. In
hoofsdtuk 7 bestuderen we de invloed van kracht en motor aantallen op

beweging van kleine membraan bolletjes in twee richtingen. We vinden dat motoren van tegenovergestelde richtig zich kunnen coördineren om transsport in twee richtingen mogelijk te maken. Ze doen dit door een door kracht gereguleerde tug-of-war, waar de kant met de meeste motoren wint.

Intracellulaire transport in de cel is afhankelijk van de succesvolle coördinatie van motor-eiwiten. In dit proefschrift hebben we laten zien welke transport dynamiek kan ontstaan als motoren samenwerken. We vinden dat motoren gevoelig zijn voor kracht en voor hun buur-motoren, en dat deze factoren beiden het transport beïnvloeden. Door intracellulair transport op een simpel *in vitro* niveau te begrijpen wordt een essentiële eerste stap gezet om de complexe cel bottom-up te gaan begrijpen.

Curriculum Vitae

Paige Marie Shaklee was born in Stamford, Connecticut, USA on October 12, 1981. She attended George Washington High School in Denver, Colorado and graduated with an International Baccalaureate Diploma in 1999. She then studied Physics Engineering at the Colorado School of Mines in Golden, Colorado where she received her B.S. In August, 2003, she joined the Master of Nanoscience program between the Delft University of Technology and Leiden University. Two major research projects contributed to her Master thesis. The first project was at National Jewish Medical and Research Center, in Denver, Colorado, in the Department of Immunology in the group of Larry Wysocki where she developed a knock-down mouse-model to study the influence of a specific receptor in lupus disease. The second research was performed at the FOM Institute AMOLF in Amsterdam in the group of Marileen Dogterom and focused on the development of an experiment with microfabricated chambers to study the influence of motor proteins on positioning processes of microtubule organizing centers. She started her PhD in November 2005 in the Physics of Life Processes group at Leiden University under the supervision of Thomas Schmidt and in the Bio-Assembly and Organization group at AMOLF under the supervision of Marileen Dogterom. The results of her research are presented in this thesis. Upon receipt of her PhD, Paige will investigate cardiomyopathies as a post-doctoral fellow in Jim Spudich's group at Stanford University in Palo Alto, California, USA.